AN INVESTIGATION INTO CONTROLLING THE GROWTH MODES OF FERROELECTRIC THIN FILMS USING PULSED LASER DEPOSITION AND RHEED

by

SEAN ROBERT CRAIG McMITCHELL

A thesis submitted to
The University of Birmingham
for the degree of
DOCTOR OF PHILOSOPHY

Department of Electronic, Electrical,
and Computer Engineering
School of Engineering
May 2008

ABSTRACT

Thin film ferroelectrics are widely considered for tunable microwave applications, the reduced dimensions leading to low tuning voltages. The incipient ferroelectric strontium titanate is suitable for tunable microwave devices, particularly in conjunction with high temperature superconductors. It has no spontaneous polarisation yet possesses a large permittivity at low temperatures that is sensitive to an electric field bias with relatively low loss. For such applications it is essential to use a low loss substrate such as magnesium oxide. In general, thin films have less favourable dielectric properties compared with their bulk counterparts due to differences in their microstructure. Strontium titanate films on magnesium oxide prove difficult to grow due to the high lattice mismatch and issues connected with chemical compatibility at the film/substrate interface. It has been shown that it is possible to engineer the growth mode of this system, altering the strain and the defect concentration. These are both known factors influencing the dielectric properties of thin films. Reflection high energy electron diffraction (RHEED) in combination with interval pulsed laser deposition (PLD) has been used to achieve a two dimensional, layer-by-layer growth mode. Crucial to this was the deposition of a unit-cell thick titanium dioxide buffer layer on the surface, the deposition of which was also controlled by RHEED. The growth mode and microstructure of films grown using standard PLD with and without the buffer layer, and films grown by interval PLD with and without the buffer

layer have been compared by analysis of the RHEED data and transmission electron microscopy. This is the first time layer-by-layer growth has been achieved in this highly mismatched epitaxial system. The results point the way towards control of defects in oxide thin films from which microstructure-property relationships may be more clearly determined.

AKNOWLEDGEMENTS

First and foremost I would like to thank Dr. Tim Jackson for seeing the project through as a truely great supervisor and reassuring me when things were going badly. I would also like to show my appreciation for my good friend, Houssny Bouyanfif, who worked closely with me in the beginning of the project, gave me much advice, provided many useful discussions and gave me a great drinking partner. Yau Yau Tse has significantly contributed to the project by providing all of the TEM analysis. Phe Suherman and Radka Chakalova showed me the PLD technique amongst others which were essential skills for a project such as this one. I am grateful, also, to Prof. Dave Blank, Dr. Guus Rijnders, Arjen Janssens, and the rest of the Twente group in Holland for allowing Houssny and I to visit and work with them for 6 weeks. Without that trip I would not have achieved what I have in this project and I thank THIOX and ESF for funding me. Donna Holdom has also been a great help in numerous ways from showing me how to use various apparatus, right through to helping with plumbing and compressed gas problems. Cliff Ansell and Gary Walsh also should be thanked for assistance with technical difficulties. My good friends in the EDT group helped in a whole variety of ways but must be thanked the most for putting up with me for so long. Thank you to Prof. Mike Lancaster for allowing me to be part of his research group and EPSRC for funding.

It would be a wrong of me not mention the great support, belief in me,

and calming influence provided by Claire Stephens, my friends and family throughout my PhD and the years leading up to it. I would also like to thank Amie Trick, for caring and being patient with me during the writing of this thesis. Her ability to cheer me up when everything feels like it's going wrong is very much appreciated. Last but not least I would like to show my gratitude to my parents for giving me the drive, ambition and belief in myself to get here as well as their support, both emotional and financial. I love you all.

Contents

List of Figures

List of Tables

Chapter 1

INTRODUCTION

Ferroelectrics [1, 2, 3] are dielectric materials which belong to any one of the 10 pyroelectric classes of crystals. All pyroelectric crystals are a subsection of the 20 piezoelectric crystal classes. Ferroelectric crystals exhibit a spontaneous polarisation below their Curie temperature, T_c, due to a unique polar axis. The spontaneous polarisation is associated with electric dipoles within the crystal structure. In ferroelectric materials the spontaneous polarisation is reversible under an external field and is many orders of magnitude larger than in a dielectric. The reversibility has important consequences since if an electric field can reverse the polarisation, the energy barrier between polarisation states must be small enough for other factors (i.e. temperature fluctuations) to overcome the barrier. So as temperature is increased the energy barrier may be mounted and the crystal will become non-polar.

Landau theory describes the ferroelectric transition from the non-polar "paraelectric" phase above T_c to the polar "ferroelectric" phase below T_c at temperatures close to T_c. There are two types of transition that the theory will allow, first and second order. A first order transition has a discontinuity at T_c for both the polarisation and the susceptibility as a function of temperature, whereas a second order transition is continuous. This thesis will concentrate only on second order transitions as the ferroelectric materials

studied here are of this type. Differentiation of the Gibbs free energy, G,

$$G = \frac{\alpha}{2}D'^2 + \frac{\beta}{4}D'^4 - E'D', \tag{1.1}$$

where $\alpha = \alpha_0(T - T_c)$, reveals that above T_c

$$\alpha_0(T - T_c) + 3\beta(\epsilon_0 E')^2 = \frac{1}{\epsilon_o \epsilon_r}, \tag{1.2}$$

and below T_c

$$\alpha_0(T - T_c) + 3\beta\left[\epsilon_r\epsilon_0 E' + \sqrt{\alpha_0\frac{(T_c - T)}{\beta}}\right]^2 = \frac{1}{\epsilon_o\epsilon_r}. \tag{1.3}$$

Here D' is the d.c. displacement field, E' is the d.c. applied electric field, α_0 and β are coefficients depending on the material, T is temperature, ϵ_0 is the permittivity of free space, and ϵ_r is the relative permittivity. From these equations, ϵ^{-1} versus temperature can be plotted if values of α_0 and β are known. A plot for the material $(Ba_xSr_{1-x})TiO_3$ (BSTO) with x=0.5 is shown in Fig. 1.1. With no applied external electric field, the permittivity goes to infinity at the transition, however, in the presence of an external field the permittivity becomes finite at the transition. The presence of an electric field also modifies the slope of the line and broadens the transition. Fig. 1.2 shows the effect of electric field on the permittivity as a function of temperature.

The dependence of the dielectric permittivity on the applied electric field is known as the tunability [5] and is defined as the ratio of the permittivity at zero field to its permittivity at some non-zero field,

$$n = \frac{\epsilon(0)}{\epsilon(E_0)}. \tag{1.4}$$

The high tunability of ferroelectric materials make them potentially very useful for tunable microwave devices, in which a d.c. field is applied to "bias" the permittivity. When considering time varying signals the amplitude of the

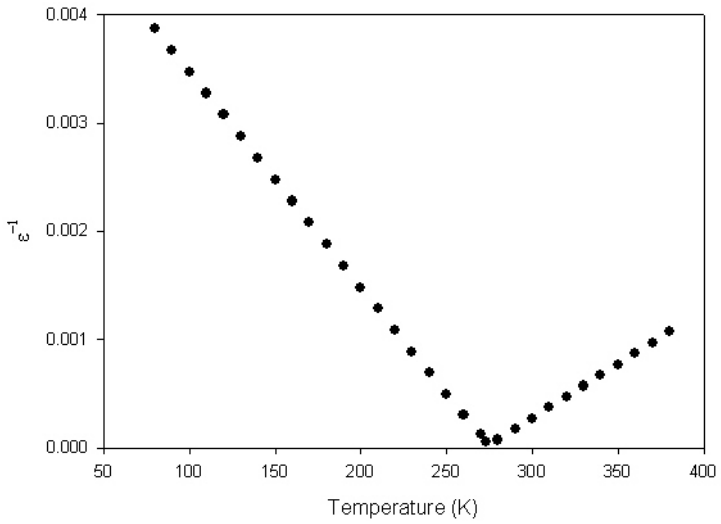

Figure 1.1: ϵ^{-1} vs. temperature in zero applied field for BSTO. The values used in equations 1.2 and 1.3 are $\alpha_0 = 1.13 \times 10^6$, $\beta = 9 \times 10^7$ which were calculated using data taken on films grown by Suherman [4].

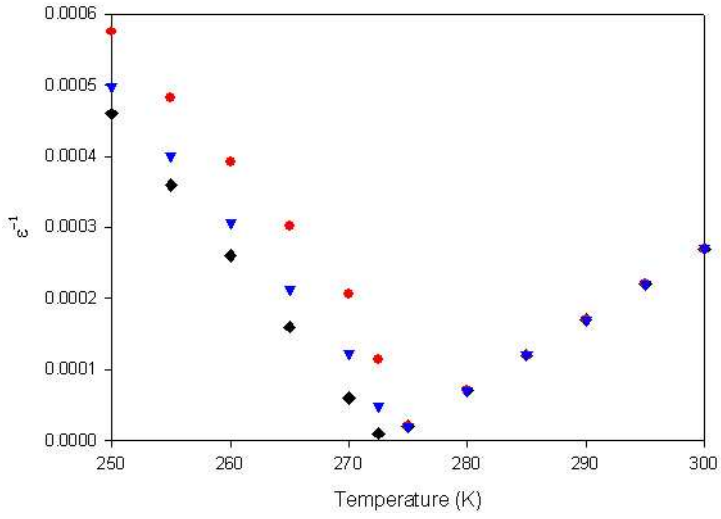

Figure 1.2: ϵ^{-1} vs. temperature for BSTO in various electric fields: black, zero applied field, blue, $8 \times 10^5 \mathrm{Vm}^{-1}$, and red, $2.8 \times 10^6 \mathrm{Vm}^{-1}$ applied fields.

a.c. field is considered to be much smaller than that of any d.c. bias field. The concept of complex permittivity is important.

If the electric field component of the a.c. microwave signal is given by

$$E = E_0 \exp(i\omega t), \tag{1.5}$$

where E_0 is the amplitude of the electric field, i is the square root of -1, ω is the angular frequency, and t is the time, then the electric displacement is given by

$$D = D_0 \exp i(\omega t - \delta), \tag{1.6}$$

where D_0 is the amplitude of the displacement field and δ is the phase difference between the displacement and the electric field. The phase angle δ is due to the system taking time to react to the change in electric field. It follows that

$$\begin{aligned} D &= D_0 \left[\cos\delta + i\sin\delta\right] \exp(i\omega t) \\ D &= \epsilon_0 \left[\epsilon_r' + i\epsilon_r''\right] E = \epsilon_0 E + P \end{aligned}, \tag{1.7}$$

where $\epsilon_r' + i\epsilon_r''$ is the permittivity with real and imaginary terms and P is the polarisation. The phase angle is associated with damping and hence with a loss in signal amplitude. A measure of the dielectric loss is the loss tangent, defined as

$$\tan\delta = \frac{\epsilon_r''}{\epsilon_r'}. \tag{1.8}$$

An ideal ferroelectric for use in tunable microwave devices would have a high tunability and low loss tangent. A quantitative method of comparing materials for use in microwave devices is the commutation quality factor [6], K,

$$K = \frac{(n-1)^2}{\left[n\tan\delta(0)\tan\delta(E_0)\right]}, \tag{1.9}$$

which is a function of the bias field, E_0. Materials with a high K are desired for microwave engineering.

Thin films are widely used in microwave tunable applications, their small dimensions leading to low tuning voltages and also relatively low cost production [5]. However, thin films have less favourable dielectric properties compared with their bulk counterparts and many factors can affect the quality of the films. The growth mode of the thin film [7], strain due to lattice mismatch [8], interfacial compatibility [9, 10], interfacial "dead layers" [11, 12], microstructural "dead layers" [13] due to features such as grain boundaries, and oxygen vacancies [14] are the major factors that affect the properties of thin film. They will all be discussed in detail in chapter 3. Monitoring and controlling the growth of the films is, therefore, essential in the production of high quality films for use in microwave devices.

Thin films of $SrTiO_3$ (STO) on substrates of MgO will be investigated in this thesis. The incipient ferroelectric STO is an ideal solution for tunable microwave devices. It has no spontaneous polarisation yet possesses a large permittivity at low temperatures that is sensitive to an electric field bias with relatively low loss. MgO is commonly used by microwave engineers as a substrate because of its low loss. Both STO and MgO are compatible with high temperature superconductors (HTS) such as $YBa_2Cu_3O_7$ which afford low conductor losses in a microwave device. Unfortunately, STO and MgO have a large lattice mismatch of $\sim 7\%$, STO having a lattice parameter of 3.905 Å and MgO having a lattice parameter of 4.213 Å at room temperature. This mismatch makes it difficult to control the growth mode of STO on MgO and introduces the possibility of strain into the system. The issue of interface compatibility is also relevant, with the SrO layer of STO being chemically incompatible with MgO [9, 10]. The films studied in this thesis will be grown by pulsed laser deposition (PLD) and growth will be monitored and controlled by in-situ reflection high energy electron diffraction (RHEED),

which will be discussed next in chapter 2.

Chapter 2

PULSED LASER DEPOSITION AND REFLECTION HIGH ENERGY ELECTRON DIFFRACTION

Pulsed laser deposition (PLD) [15, 16] is a common and very suitable method of depositing thin films of complex oxides such as $SrTiO_3$ (STO) amongst many others. In this method, photonic energy is coupled to a stochiometric target and ablates material in the form of a plasma plume which is then condensed on the surface of a heated substrate placed opposite the target. PLD offers several advantages over other deposition techniques such as stochiometric transfer from a single target no matter how chemically complex the material, easily controllable high deposition rates due to the pulsed nature of the deposition and the ability to deposit many heterostructures that are not always otherwise possible due to the process taking place away from thermal equillibrium. Disadvantages include difficulties in transfering research to mass production and macroscopic ejecta in the plume, however, some of these can be overcome by choosing carefully the deposition parameters.

In-situ reflection high energy electron diffraction (RHEED) is a powerful tool used to monitor and study the growth of thin films. This technique requires an electron beam at grazing incidence to the substrate in the PLD

system with a phosphor screen opposite and a camera to collect data. Early demonstrations of this technique used in combination with PLD [17, 18] yielded promising results on complex oxides, however, a low background pressure of oxygen was required to prevent oxidation of the electron gun filament and allow the electrons a sufficient mean free path for diffraction to take place. The problem of poorly oxygenated films was usually solved by pulsing oxygen onto the substrate surface in synchronisation with the pulsing of the laser but this complicated deposition systems with extra electronics. PLD systems with in-situ RHEED were later simplified by introducing differential pumping [19] so that the electrons travel the majority of the distance between the source and substrate in a low pressure tube. This allowed the deposition to take place at oxygen pressures that are needed to sufficiently oxygenate complex oxide films.

2.1 Pulsed laser deposition

Pulsed laser deposition (PLD) [15, 16, 20] is a physical deposition technique in which a high powered UV pulsed laser is used to ablate material from a target, forming a plasma plume which then condenses on a heated substrate placed opposite. This usually takes place in the presence of a background atmosphere of oxygen or some other gas. The photonic energy is coupled to the bulk material of the target and is converted into electronic excitations. A transfer of energy from the electrons to the lattice occurs within a few picoseconds and heating begins [15]. There are a number of parameters that require optimisation in PLD; laser pulse frequency, energy, spot size on the target, distance between the substrate and target, oxygen pressure and substrate temperature. These parameters are chosen to give the optimum film quality and growth. The laser pulse is absorbed in the target within the

optical absorption depth, $1/\alpha$, where α is the optical absorption coefficient. If $1/\alpha$ is smaller than the thermal diffusion length, $l_T = 2\sqrt{D\tau}$, such as is the case in metals, then all the photonic energy is deposited into the optical absorption depth and efficiently heats the target down to a depth of l_T during the laser pulse. This results in the ejection of thermal particles and can lead to non-stochiometric ablation. Here, D is the thermal diffusion constant and τ is the laser pulse duration. If, however, $1/\alpha$ is larger than l_T, as the case for most complex oxides and insulators, then the material is only heated within the optical absorption depth and the condition for stoichiometric transfer is met. In this regime, with nanosecond pulse durations, laser supported ablation takes place where only the first 100 or so picoseconds of the laser pulse ablates material from the target. The bulk is then screened from the remainder of the laser pulse by the plasma which absorbs the energy becoming increasingly hotter and more ionized. This can be understood by assuming that most materials used in PLD have an extinction coefficient, ξ, of approximately 1.5 [15, 21]. The absorption depth, given by

$$\frac{1}{\alpha} = \frac{\lambda}{4\pi\xi}, \tag{2.1}$$

for these materials is therefore around 13 nm. If there is a laser focus on the target of 2 mm^2 then the absorption volume contains approximately 3×10^{-9} moles. The enthalpy of vaporisation for most materials deposited in PLD is of the order of 500 kJ mol^{-1} [15, 22] and therefore, only 1.5 mJ is required for vaporisation of the optical absorption depth. If it is assumed that the total photonic energy of each 20 ns laser pulse is 30 mJ then only 5% of the pulse energy is used in vaporising, leaving 95% to ionise the plume.

Once the plasma has been formed in a layer next to the target it expands outwards due to the high local pressure. The recoil from this expansion of gas can cause particulates or "laser droplets" to be ejected into the plume

from the heated target caused by contact with the hot plasma. Another possible mechanism for the creation of these droplets is if the time required for the laser energy to be converted into heat in the bulk is shorter than the time that is required for the surface layer to be vaporised. In this situation the subsurface boiling ejects droplets from the surface layer [15, 23]. Solid particulates can be expelled from the target when surface roughening caused by the laser becomes significant [15, 24]. The outgrowths within the roughened area can fracture and be released into the plasma if the conditions are suitable. The effects of these mechanisms can be reduced or eliminated by carefully selecting the depostion parameters.

When the plasma expands out from the target it forms the so called "plume" [16, 25]. The size and shape of the plume is determined by the pressure of the background atmosphere and the angular distribution of kinetic energy of the ablated particles. The resultant plumes have a standard form [25] with a number of possible features as shown in Fig. 2.1. The brightest area of a plume is the core which is adjacent to the point on the target where the laser is impinging. From the core, a central stream is directed orthogonally away from the target surface due to the high kinetic energy of the ablated particles in this direction. Surrounding the core is a less luminous body and surrounding the central stream there is a finger of similar brightness. Depending on the ablated material and deposition parameters there can also be a halo-like feature where the light emission is even lower than in the body and finger. Background pressure can effect the size and shape of the plume and as pressure is decreased the shape goes from having a halo-like structure through having a more pronounced body and finger shape, with the plume getting longer, to at lower pressures the plume growing ever more spherical in shape, all the while the plume getting larger before ther-

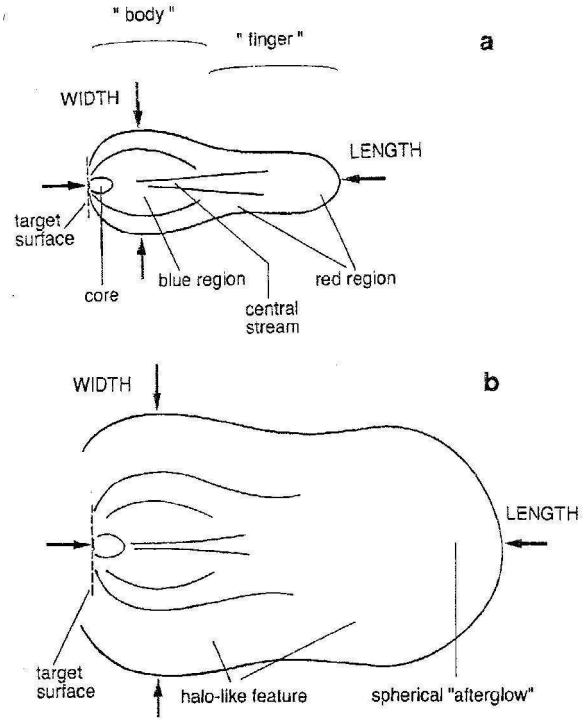

Figure 2.1: Schematic diagram of a plasma plume [25] without, (a), and with (b) the halo-like features occasionally seen. The colours refer to the plume from a YBCO target ablated in oxygen.

malising. Decreasing the laser spot size on the target also makes the plume more spherical, and with less material per pulse being ablated the size of the plume decreases. As with the effect of spot size on the plume, decreasing the fluence of the laser beam decreases the amount of ablated material in the plume and so makes it smaller.

The adatoms from the plume recondense on the substrate surface directly in front of the target. The substrate is held at elevated temperatures promoting surface diffusion of the adatoms to stable sites, however, this high temperature also increases the probability of a small percentage of the adatoms being re-evaporated. How the adatoms settle in stable site and the

manner in which the crystal structure of the film grows depends on a number of factors such as surface mobility and lattice mismatch between the substrate and the growing film. This will be discussed in more detail in chapter 3.

2.2 Reflection High Energy Electron Diffraction

Reflection high energy electron diffraction (RHEED) is a surface characterisation technique that utilises electron diffraction in such a geometry as to provide a very detailed insight into surface structures on an atomic scale. It is compatible with vacuum conditions and so has been used extensively to investigate thin film growth with a number of physical deposition techniques. A typical RHEED system consists of an high energy focused electron source placed at grazing incidence to the substrate with a phosphorescent screen and CCD camera opposite to collect data. RHEED is a relatively cheap but powerful tool in the study of thin films and heterostructures. However, relatively high background pressures of oxygen are required in the deposition of complex oxides such as $SrTiO_3$ to prevent excess oxygen vacancies which can adversely affect physical properties. These high pressures can prevent the use of RHEED due to reductions in the electron path length and other problems such as electron gun filament oxidation. This problem was overcome in the early 1990's by having a pulsed atomic oxygen source directed onto the substrate allowing the overall pressure of the chamber to be kept low but providing a high density of oxygen near the substrate during each pulse [17, 18]. Electronics that controlled the timing of the oxygen pulsing complicated the system design, could be problematic and the pressure pulsing could interfere with RHEED intensity measurements. A more simple design was demonstrated in the late 1990's that differentially pumped the chamber

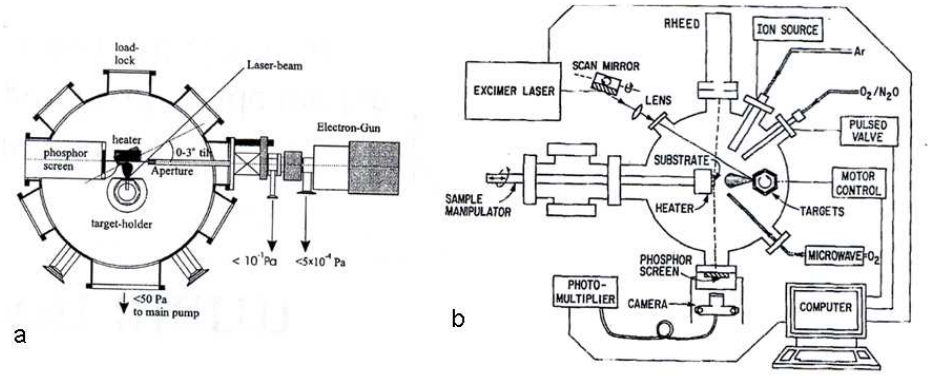

Figure 2.2: Two different RHEED system configurations with the differentially pumped system [19], (a), and the system with a pulsed oxygen supply [17], (b).

and electron gun separately [19]. To prevent the electron beam from being scattered by the deposition pressure of the chamber a tube surrounded the majority of the electron path. The tube was pumped by the pumps for the electron gun and was partially sealed at the far end with an aperture that the beam could be directed through but was small enough to prevent excess gas from being removed from the main chamber. The two systems are shown schematically in Fig. 2.2.

2.2.1 RHEED Patterns

Due to the grazing incidence, RHEED is a two dimensional diffraction with electrons only penetrating the top most atomic layers of the sample and thus it is very surface sensitive. The Ewald construction [1, 16, 26] is a useful model that makes it easy to visualise the diffraction conditions and pattern produced. A sphere of radius $k_0 = |\mathbf{k}| = 2\pi/\lambda$ is drawn, the incident wavevector of the electrons, $\mathbf{k}$, is drawn terminating on a reciprocal lattice point. The origin of the sphere is chosen to be consistent with the direction

of **k**. In this thesis the electron energy used in all experiments was 35 keV which created a Ewald sphere radius of 9.56×10^{11} m^{-1}. The two dimensional reciprocal lattice of the surface is represented, for a perfect crystal, by infinitely thin rods protruding from the reciprocal lattice points of the surface. The reason that rods are seen can be explained by considering a three dimensional lattice in real space being expanded along one of its axes without limit, so in reciprocal space the lattice points move closer together before forming a rod in the limit. The intersection of the lattice rods with the Ewald sphere, seen in Fig. 2.3, shows where diffraction spots occur. They lie on rings known as Laue circles in the case of a two dimensional surface. If there is crystallographic disorder, an uncertainty in the lattice parameters of the surface being investigated is introduced and this gives the lattice rods a finite thickness. The combination of the thick rods and the curved surface of the Ewald sphere gives the effects of streaks lying on the Laue circles instead of diffraction spots. Another phenomenon that causes this same effect is uncertainty in the electron energy which leads to a smearing of the Ewald sphere thickness. If the surface roughens to the point of there being penetration of the incident electron beam through islands then the diffraction will become three dimensional and the rods will become an array of spots leading to diffraction spots positioned in a grid-like pattern. Using the Ewald construction, inspection of the RHEED pattern can provide information about the surface roughness and crystallographic order, which gives insight into the growth mode of the film. Fig. 2.4 shows RHEED patterns for the three types of surface mentioned here.

The Ewald model provides a visual representation of the Laue diffraction conditions [1, 3, 26] which will be discussed in greater detail now. A plane wave is considered with wavelength λ incident at grazing angle θ_i on a one

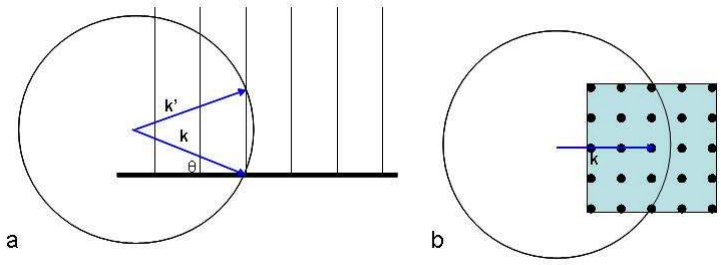

Figure 2.3: Lattice rods intersecting Ewald sphere, side view, (a), and plan view, (b). Here θ is the angle of incidence.

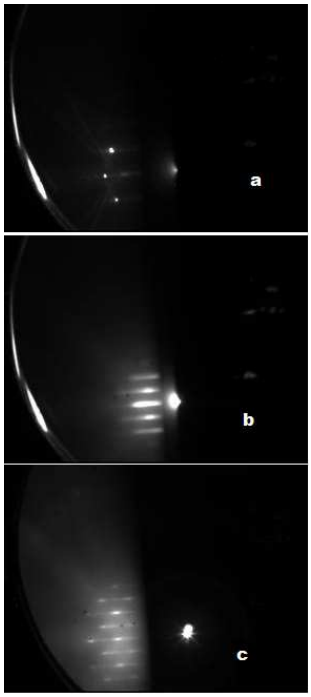

Figure 2.4: RHEED patterns from a two dimensional $SrTiO_3$ surface, (a), a two dimensional surface with crystallographic disorder, (b), and a three dimensional surface, (c).

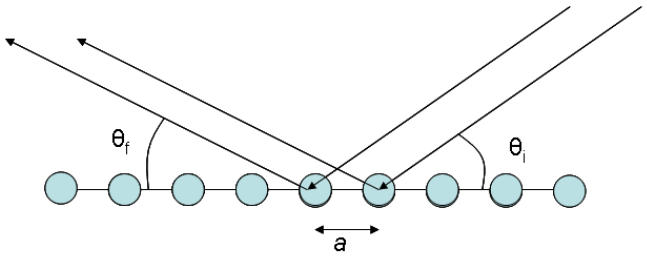

Figure 2.5: A plane wave incident at angle θ_i on a one dimensional array of atoms that extend in the direction $\hat{\mathbf{a}}$ with lattice spacing a.

dimensional array of atoms that extend in the direction $\hat{\mathbf{a}}$ and are separated by a distance a. The wave is then scattered at the grazing angle θ_f. This is shown in Fig. 2.5. Constructive intereference occurs when the path difference between the scattered waves from two adjacent atoms is equal to an integer number of wavelengths:

$$a\cos\theta_i - a\cos\theta_f = n\lambda. \tag{2.2}$$

This can be rewritten using the identities $k = 2\pi/\lambda$ and $G = 2\pi n/a$ to show that the difference in parallel components of the incident and scattered wave vectors is equal to a multiple of the reciprocal lattice spacing,

$$k\cos\theta_i - k\cos\theta_f = G. \tag{2.3}$$

Conservation of energy ensures the magnitudes of the initial and scattered wavevectors are equal and so constrains the scattered wavevectors to circles at the base of cones of angle $2\theta_f$ around $\hat{\mathbf{a}}$ as seen in Fig. 2.6. This is only the case when considering a one dimensional array of atoms. When a second dimension is also considered there are rows of atoms running parallel to the one dimensional array and this leads to interference maxima around the circles. The required condition for where these spots on circles lie can be seen if the sample surface is decribed by a two dimension reciprocal lattice

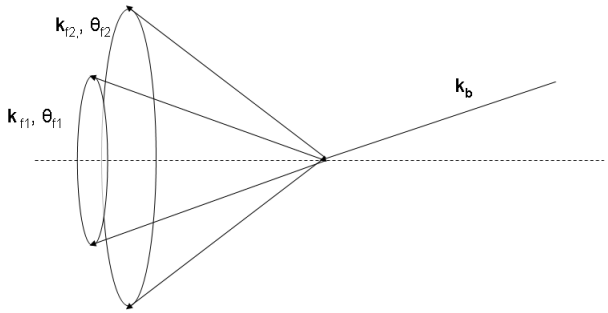

Figure 2.6: Laue cones formed by two allowed final wave vectors of diffraction off a one dimensional array of atoms.

which consists of points described by a series of lattice vectors,

$$\mathbf{G} = m\mathbf{a}^* + n\mathbf{b}^*, \tag{2.4}$$

where m and n are integers and $\mathbf{a}^*$and $\mathbf{b}^*$are reciprocal lattice unit vectors decribed by

$$\begin{aligned} \mathbf{a}^* &= 2\pi \frac{\mathbf{b}\times\hat{\mathbf{z}}}{\mathbf{a}\cdot(\mathbf{b}\times\hat{\mathbf{z}})} \\ \mathbf{b}^* &= 2\pi \frac{\mathbf{a}\times\hat{\mathbf{z}}}{\mathbf{b}\cdot(\mathbf{a}\times\hat{\mathbf{z}})} \end{aligned} . \tag{2.5}$$

Here $\mathbf{a}$ and $\mathbf{b}$ are the real-space lattice unit vectors, and $\hat{\mathbf{z}}$ is the unit vector normal to the surface being studied. By comparison to equation (2.3) it is clear to see that the condition for diffraction is that

$$\mathbf{S}_{||} = \mathbf{G}. \tag{2.6}$$

where $\mathbf{S}_{||}$ is the component of $\mathbf{k_f} - \mathbf{k_i}$ parallel to the surface being examined. This Laue condition coincides with the spots lying on rings which are given by the Ewald construction. The Laue model described here provides an excellent

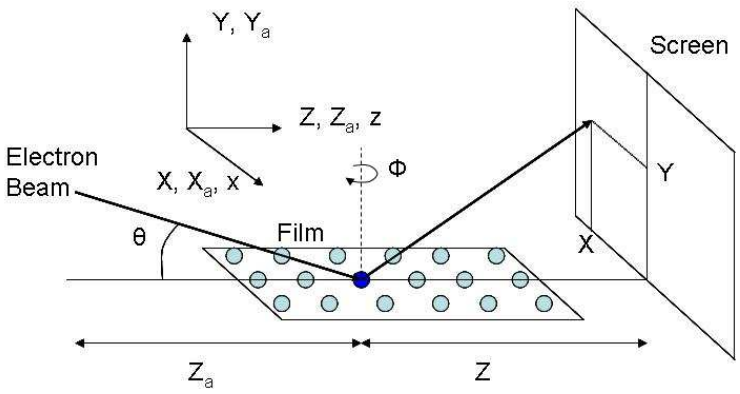

Figure 2.7: A schematic view of the RHEED electron path. The electrons travel at grazing incidence from the source which is positioned at coordinates X_a, Y_a, Z_a to a lattice point on the surface given by coordinates x, z and are scattered to a point on the RHEED screen X, Y, Z. The origin of all coordinate systems is the origin of the lattice shown here as the dark blue lattice point. In this model θ is the angle of incidence and ϕ the azimuthal angle.

understanding of the underlying physics of diffraction in ideal conditions but proves very complex when used to predict RHEED diffraction patterns from thin film surfaces in actual real-life conditions. Complications such as surface disorder and variations in electron energy produce streaked spots lying on the Laue circles of a two dimensional surface which are difficult to simulate using the Laue or Ewald constructions directly.

A model that proves more simple with which to construct a simulation and which takes into account surface disorder was divised by Bozovic et al. [27, 28] and is expanded upon in this thesis. A schematic view of the model can be seen in Fig. 2.7. It works by considering just one electron traveling from the source to the sample surface and then on to the screen. Considering the wave function of the electron, the probability of it arriving

at any point on the screen is given by the square modulus of the sum of waves that take all possible paths. The most probable path is the shortest path. The pathlength is approximated by assuming that all atoms on the surface scatter a spherical wave from the incident beam and each wave is expressed in the form $\cos(kR_{ij}) + i\sin(kR_{ij})$ where R_{ij} is the total path of the electron from the common emmission point to the point on the screen. So the intensity is given as a function of screen position:

$$I(X,Y) \propto \left\{ \left[\sum_i \sum_j \cos(kR_{ij}) \right]^2 + \left[\sum_i \sum_j \sin(kR_{ij}) \right]^2 \right\}, \tag{2.7}$$

where

$$k = \frac{\sqrt{2mE}}{\hbar}, \tag{2.8}$$

and

$$R_{ij} = \sqrt{(X_a + x)^2 + Y_a^2 + (Z_a + z)^2} + \sqrt{(X - x)^2 + Y^2 + (Z - z)^2}. \tag{2.9}$$

Here m is the electron rest mass, E is the electron energy, $\hbar$ is Planck's constant divided by 2π, X_a, Y_a, and Z_a are the coordinates of the electron source, X, Y, Z the coordinates of the pixel on the RHEED screen, and x and z are the coordinates of the ith, jth atom. All coordinates are with respect to the origin of the surface. Note that in Fig. 2.7 the crystal is shown aligned so that <100> coincides with the $\hat{\mathbf{z}}$ axis. The azimuthal angle of incidence, ϕ, is defined with respect to <100> and is zero in the figure. The values of x and z are calculated using the polar coordinates of the ith, jth atom from the origin. This is neccessary in order to simulate the pattern for the beam directed along any azimuthal angle. The distance of each lattice point from the origin is the magnitude of the lattice vector and is calculated using

$$r_{ij} = \sqrt{(ia)^2 + (jb)^2}, \tag{2.10}$$

where a and b are the in plane lattice parameters. The angle, α, between $\mathbf{r}_{ij}$ and <100> is given by

$$\alpha = \tan^{-1}\left(\frac{jb}{ia}\right). \tag{2.11}$$

Hence the x, z coordinates of the i, jth atom can be easily be calculated for any azimuthal angle using

$$\begin{aligned} x &= r_{ij}\cos(\alpha+\phi) \\ z &= r_{ij}\sin(\alpha+\phi) \end{aligned}, \tag{2.12}$$

where ϕ is the azimuthal angle at which the beam strikes the sample with respect to the <100> direction. By selecting the limits on the values of i and j an indication of the effect of various degrees of crystallographic coherence can be observed. In Fig. 2.8 simulated RHEED patterns from 10×10, 50×50, and 100×100 surface arrays are shown. In (a)-(c) the incident beam is along the <100> direction. For a 10×10 array paterns when the beam is directed along <110>, (d), and in the direction 7° away from the <100> direction, (e), are shown. The full code for this simulation can be see in appendix 1.

The model described above predicts the expected RHEED spot positions by calculating the lattice positions of a system very well at any azimuthal angle and qualitatively simulates how RHEED streaks alter with increasing surface coherence. Unfortunately, quantitative analysis of peak intensities is not possible with this model as it assumes only kinematic phenomena occur. This is not the case with RHEED; dynamical scattering [16, 26] also occurs resulting from such effects as mutliple and inelastic scattering. These phenomena cause anomalies in intensity and extra features in the diffraction pattern. The most common features seen due to dynamical effects in RHEED patterns are Kikuchi lines as seen in Fig. 2.9. These are seen as curved lines which move with azimuthal rotation as if they were rigidly fixed to the

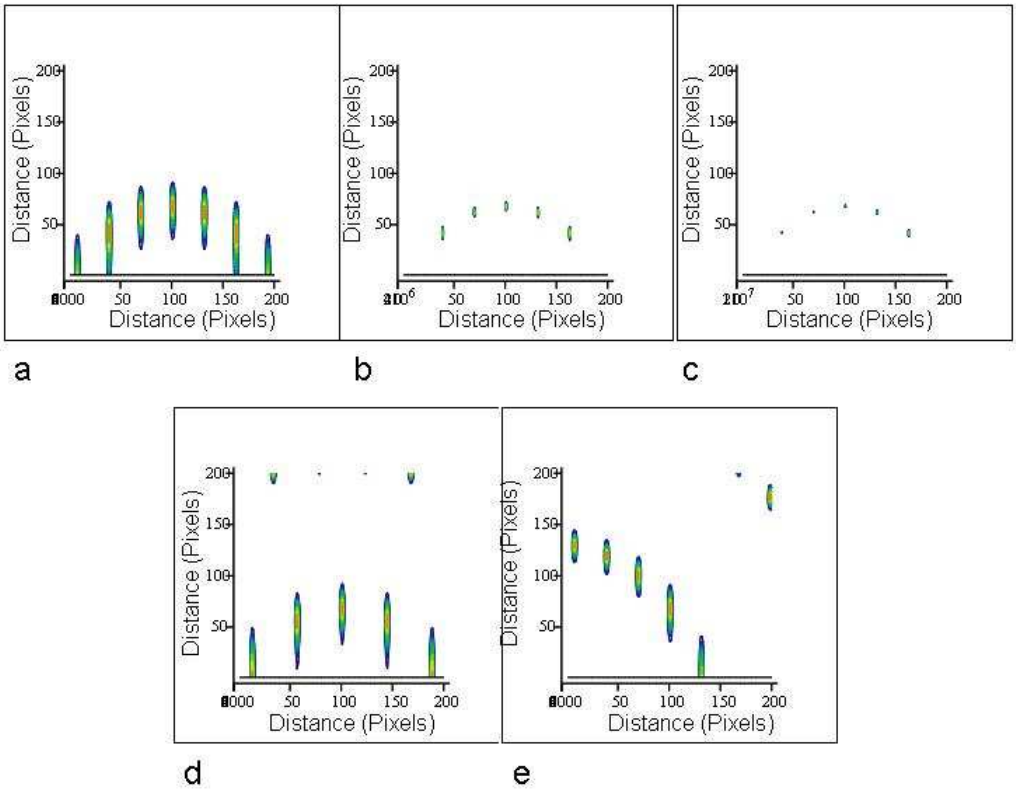

Figure 2.8: Simulated RHEED patterns [27] with the incident beam along the <100> direction for 10×10 (a), 50×50 (b), and 100×100 (c) surface arrays. Also, patterns with the incident beam along the <110> (d), and 7°away from the <100> direction (e) for a 10×10 array.

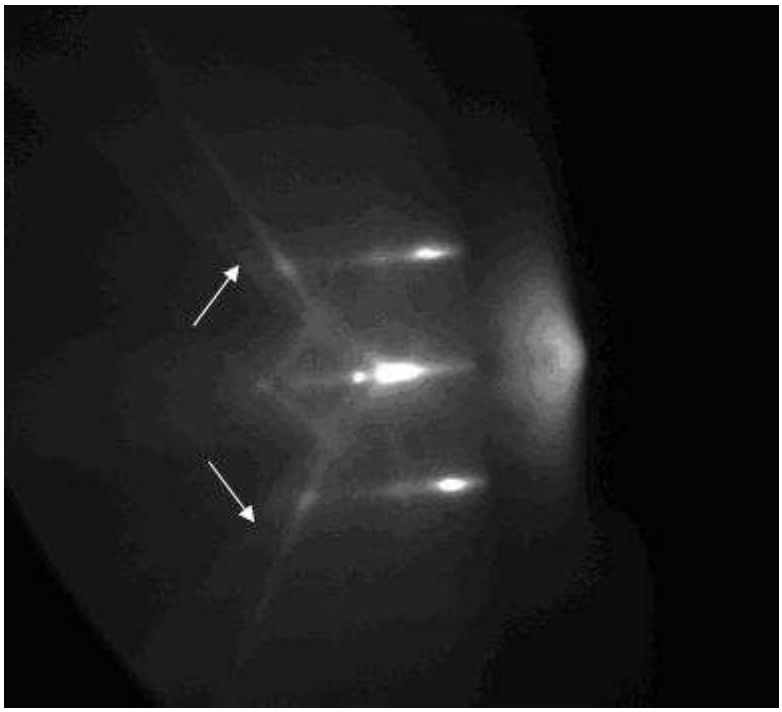

Figure 2.9: Kikuchi lines, indicated by white arrows, on a RHEED pattern from a MgO surface with the incident beam along the direction <100>.

lattice, converging at the (00) lattice rod when the incident beam is along a direction of high symmetry. Kikuchi lines are a good indication of a smooth, crystallographically coherent surface, as will be seen in chapters 4 and 5.

2.2.2 RHEED Intensity Measurements

Static diffraction patterns in RHEED provide useful information on the surface of a film including the lattice parameters of the sample in question, in-plane strain, crystallographic coherence, and surface roughness. However, in addition to these data, monitoring the real-time intensity of the RHEED spots can determine the growth mode of the film [16, 19, 26]. As unit cell high steps are much larger than the wavelength of the electrons at typical RHEED energies, and because of the grazing incidence of the RHEED geom-

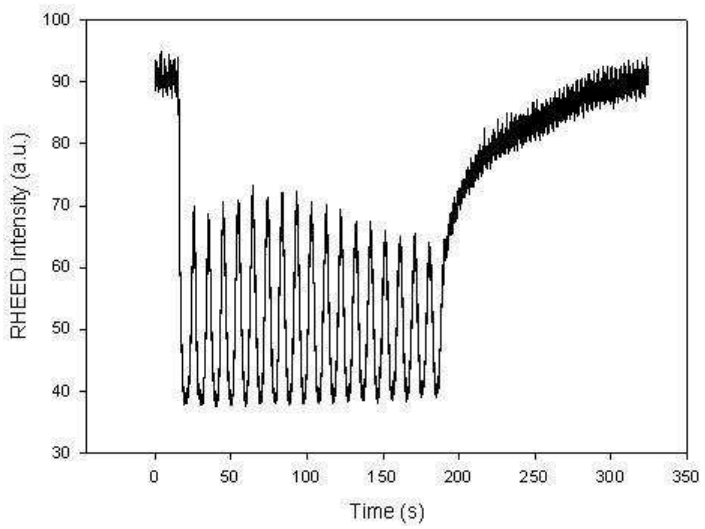

Figure 2.10: Typical RHEED intensity oscillations for two dimensional layer-by-layer growth of STO on an STO substrate.

etry, the electrons are readily scattered from two dimensional islands of the surface of a growing film. If a film is growing in a layer-by-layer fashion then as a unit cell layer begins to grow the film surface becomes gradually more rough on an atomic scale as two dimensional islands nucleate. The increase in step density leads to a decreased intensity of the diffracted RHEED spot being observed. When the layer reaches a coverage such that the step density begins to decrease as more material is added the RHEED intensity begins to increase again. This leads to an oscillatory behaviour of the RHEED intensity; a typical RHEED intensity measurement for a two dimensional layer-by-layer growth can be seen in Fig. 2.10. The deposition rate can be calculated from the period of the oscillations. Damping of the oscillations can occur due to surface roughening caused by the pulsed arrival of material inherent to PLD but a number of other factors can effect the growth. The intensity measurements in this thesis were all taken with a grazing in-

cident angle such that the electrons scattered from all levels of the surface are an integer number of wavelengths apart in order to give the maximum scattered intensity; this is known as the "in-phase" condition. Here, the intensity oscillations are caused by the roughness of the surface on an atomic scale, whereas in the "out-of-phase" condition it is an interference effect that dominates the oscillations [26]. There are various models that describe the nature of the RHEED intensity oscillations but most are based on the incident angle being in the out-of-phase condition. A model that works at the in-phase condition is the step density model which relies on the step edges of the growing islands scattering the electrons diffusely. This model will be be discussed now.

The step density model [16, 29, 30] describes the intensity oscillations seen in RHEED by assuming a one level growth, i.e. a growth with no second layer nucleation, and considering the change in density of surface steps after each deposition pulse. This also assumes instantaneous nucleation at the begining of each monolayer, which is reasonable with PLD due to the high supersaturation within the deposition pulse, and subsequent growth of two dimensional circular islands by step propagation. A surface is considered with a number of equally spaced islands of density equal to the nucleation density N_s, as seen in Fig. 2.11. After each pulse there is a certain density of adatoms which then diffuse to the step edges and are incorporated causing the islands to grow, thus increasing the coverage and in turn the step density. Therefore, the change in step density is dependent on the surface diffusivity and average travel distance of the adatoms which is determined by N_s and the average island size. The average island size is dependent on coverage [16]:

$$\pi r_2^2(t) = \frac{\theta(t)}{N_s}, \tag{2.13}$$

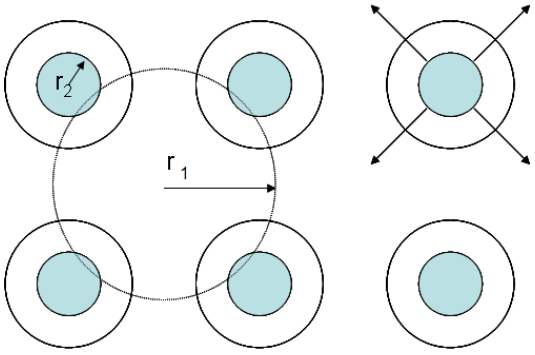

Figure 2.11: A schematic plan view of the growing islands on the two level film surface used in the step density model. r_2 is the radius of the islands, hich have a density N_s given at coverage θ and $r_1$represents the radius of the area between the islands. The white region around the islands represents the increase in coverage after one further pulse.

where πr_2^2 is the area of the islands. The characteristic time for the diffusing particles on the second level (on top of the islands) to travel to a step can be given as a function of coverage also,

$$\tau_2 = \frac{\theta}{D_s(\mu_1^{(0)})^2 \pi N_s}, \tag{2.14}$$

here D_s is the surface diffusion coefficient and $\mu_1^{(0)}$ is a root of the Bessel function and is equal to 2.40.

The same procedure can be used to describe what happens on the first level (between the islands). The coverage dependent area between islands can be approximated using [16]

$$\pi r_1^2(t) = \frac{1-\theta(t)}{N_s}, \tag{2.15}$$

where $1-\theta(t)$ is the proportion of the surface that is not covered by the growing monolayer. The characteristic decay time of the particles diffusion

from between the islands is

$$\tau_1 = \frac{1-\theta}{D_s(\mu_1^{(0)})^2 \pi N_s}. \tag{2.16}$$

If n_p is the number of pulses to complete a monolayer ($\theta = 1$) then $\frac{1}{n_p}$ represents the density of deposited adatoms in one pulse. Also, if θ_{n-1} is the coverage before applying a pulse then multiplication of the sum of θ_{n-1} and $(1-\theta_{n-1})$ by $\frac{1}{n_p}$ gives the total number of particles, expressed in terms of θ, deposited on top and in between the islands, respectively. So the change in coverage after one deposition pulse is given by

$$\Delta\theta_n(t) = \frac{\theta_{n-1}}{n_p}\left(1 - \exp\left(-\frac{t}{\tau_2}\right)\right) + \frac{(1-\theta_{n-1})}{n_p}\left(1 - \exp\left(-\frac{t}{\tau_1}\right)\right). \tag{2.17}$$

From the coverage the step density [29, 30] can be calculated using

$$S(t) = 2\sqrt{\pi N_s}(1-\theta)\sqrt{-\ln(1-\theta)}, \tag{2.18}$$

and using this the RHEED intensity can be predicted as

$$I(t) \propto 1 - \frac{S(t)}{S_{max}}, \tag{2.19}$$

where S_{max} is the maximum step density reached in the growth of one monolayer with no second layer nucleation. The intensity oscillation of one monolayer predicted using this model with parameters similar to those used in depositions for this project are seen below in Fig. 2.12. The intensity oscillation is clearly modulated by the laser pulsing due to the process of the addition of an instantaneous density of adatoms on the surface and the subsequent diffusion to the step edges. These modulations are similar to that of typical RHEED intensity relaxations but are not seen in RHEED data in this project due to the experimental setup (chapters 4 and 5).

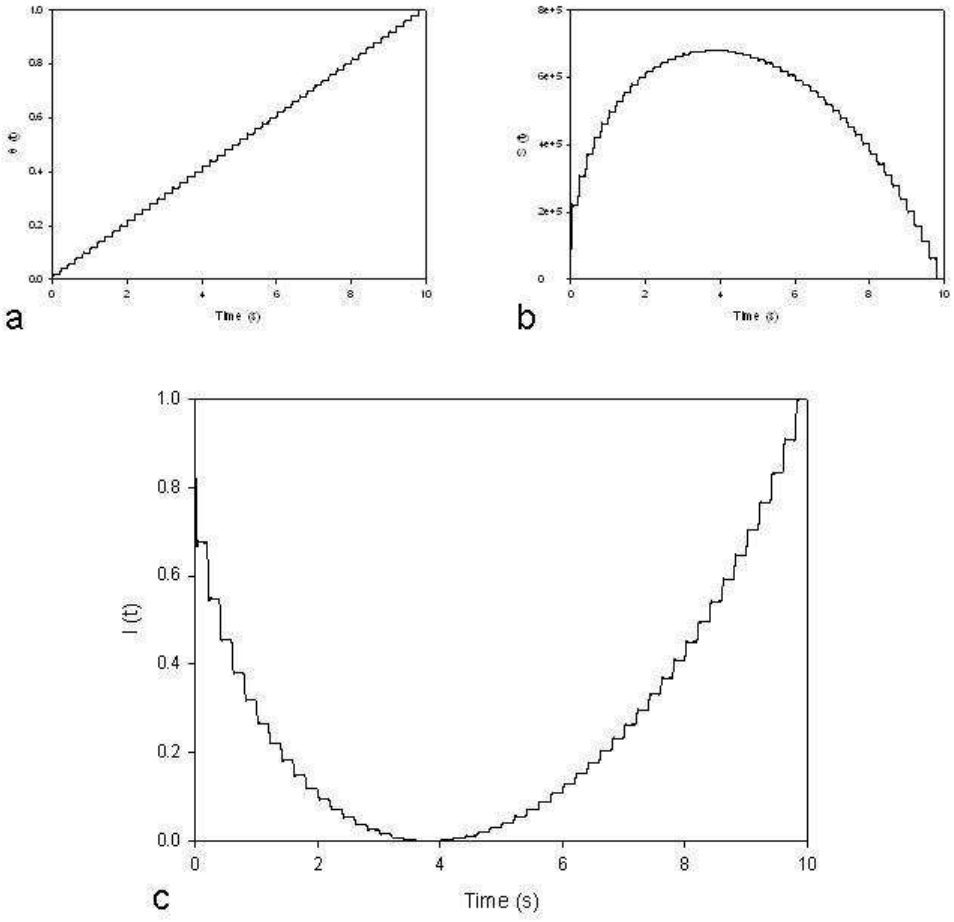

Figure 2.12: RHEED intensity oscillation simulated using the step density model. The change in coverage, (a), leads to a change in step density, (b), which in turn leads to an intensity oscillation, (c).

2.3 Experimental Methods

A detailed study of the growth of a complex oxide perovskite ferroelectric ($SrTiO_3$) on a substrate with a NaCl-like structure (MgO) using PLD and RHEED was the main focus of this thesis. PLD is a complex process with several essential stages that need to be considered to achieve a growth mode that produces a stoichiometric film of the highest crystallographic quality. Substrate preparation, preablation and deposition conditions, and the order in which these conditions are applied are all important factors that need to be reproduced accurately in order to achieve reliable results. RHEED is a useful tool to be used in conjunction with PLD to study the growth but it is a method that is littered with features that can alter intensity measurements considerably if they are not avoided. In the following sections, all of these considerations will be discussed in detail along with a description of the experimental setup and experimental methods.

2.3.1 Experimental Setup

The PLD-RHEED system used in this thesis was comercially bought from Twente Solid State Technologies (TSST); a schematic diagram of the system can be seen in Fig. 2.13 and photographs of the actual system can be seen from two different angles in Fig. 2.14 and Fig. 2.15. It is a high vacuum chamber with a base pressure of $\sim 5 \times 10^{-8}$ mbar and load lock for removal and insertion of heater and targets without the need to break vacuum. It has in-situ RHEED for monitoring of the growth and an additional ion-beam milling chamber. The system is fully automated with a computer controlling valves, gas flows, heater, shutter and target movements. The RHEED uses differential pumping for high pressure measurements via a secondary turbo pump seen below the RHEED gun in Fig. 2.15. A valve (the "RHEED valve"

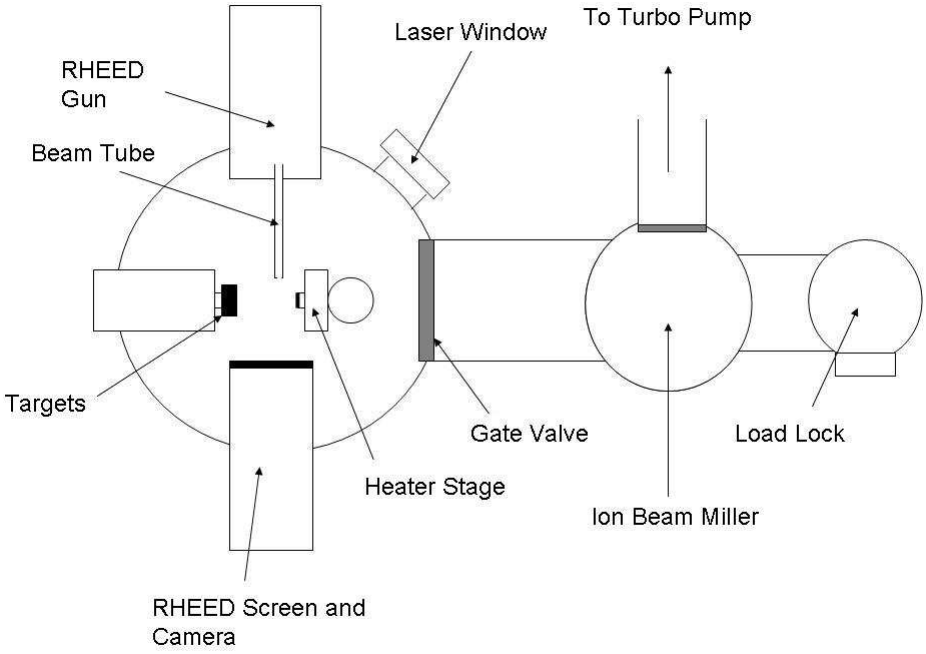

Figure 2.13: A schematic diagram of the PLD-RHEED system.

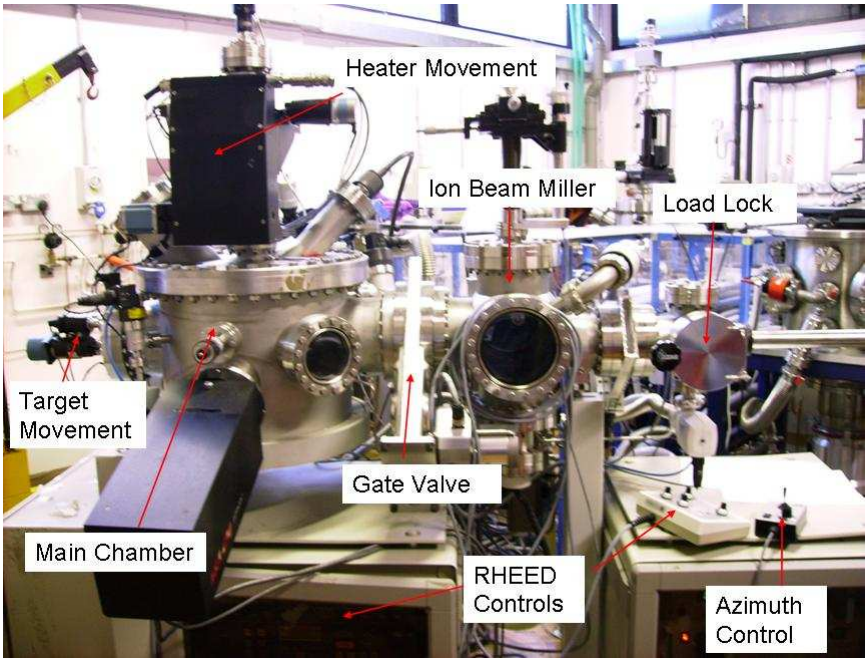

Figure 2.14: The RHEED-PLD chamber with all the main components labelled.

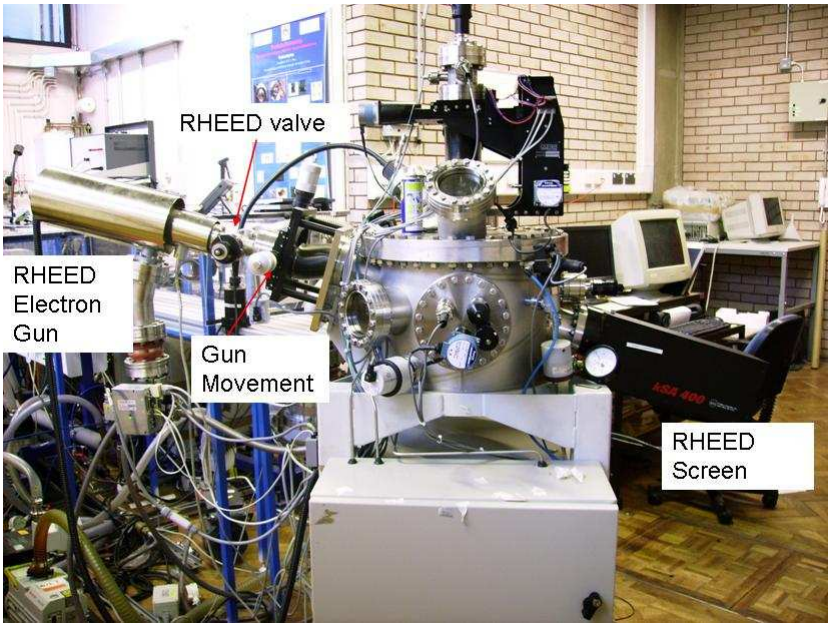

Figure 2.15: The RHEED configuration on the main chamber.

in Fig. 2.15) isolates the gun from the main chamber when closed. When the RHEED beam is required, this valve is opened to pump the beam tube in Fig. 2.13. In this way the pressure in the gun and tube is maintained below 5×10^{-4} mbar even when the pressure in the chamber is at a pressure as high as 1 mbar. Care has to be taken to ensure this valve is closed when the main chamber is raised above 1 mbar to protect the gun filament. The gun has a maximum voltage of 35 kV and a maximum current of 1.6 A. The kSA 400 software is used to take images from the RHEED, intensity measurements and undertake analysis.

A Lambda Physik/Coherent LPX 200 laser was used in the ablation process for this thesis. The voltage range of the laser was 18-24 kV and the maximum laser pulse frequency was 100 Hz. For pulse frequencies higher than 10 Hz a maximum voltage of only 22 kV could be used. The laser was always used in "constant voltage" mode because at high frequencies the internal energy measurements used for "constant energy" mode decreased in accuracy causing a large drift in laser energy. Energy was measured with an in-line meter which measured 10 % of the laser beam via a beam splitter on the optical track. The laser beam was reflected down the optical track with a mirror at 45° to the laser. The beam was cut with a 0.8×0.9 cm aperture in the centre of the beam which then passed through an attenuator. This was used so that the laser could be operated at the highest possible voltage as the pulse-to-pulse energy was more stable in this regime. From the attenuator, the beam passed through the beam splitter and the part that was not deflected out of the beam was focused on the target using a lens with a focal length of 35 cm to a spot of 1.55×0.85 mm on the target. The lens was positioned such that the focus of the beam was in front of the target.

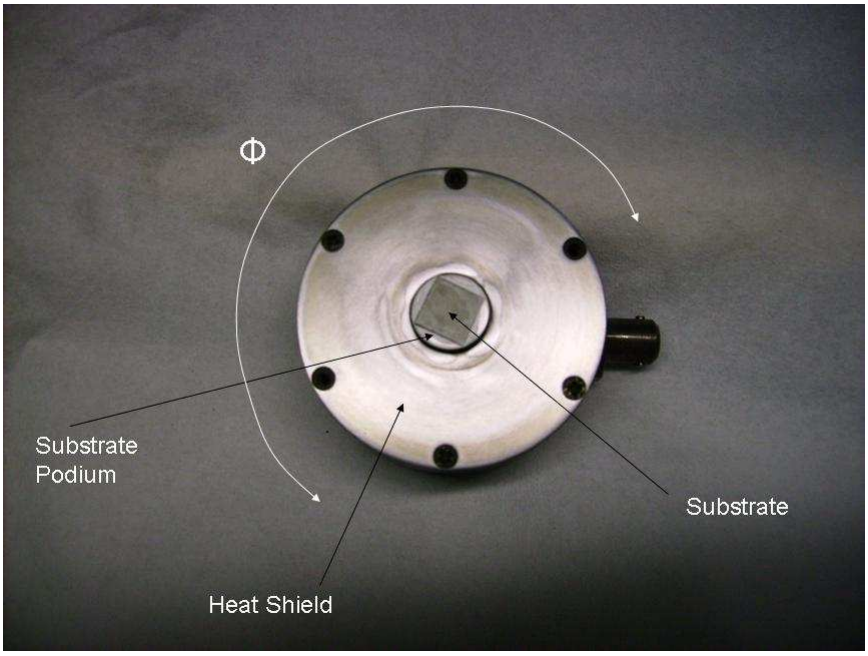

Figure 2.16: A substrate glued to the heater. The azimuthal angle, ϕ, is also shown here to indicate the heater manipulation inside the chamber.

2.3.2 Preparation

The heater used in conjunction with the PLD-RHEED system was also designed by TSST. It consists of a heater block with a substrate podium in the centre and heat shielding around the heater block and surrounding the podium, covering the main heater surface but allowing the podium to protrude. The layout of the heater can be seen in Fig. 2.16. Before a substrate could be attached to the heater, the heater needed to be cleaned. The top heat shield was removed and the podium surface was first cleaned with ferric nitrate solution, $Fe(NO_3)_3.9H_2O$, to remove any silver dag that was left over from previous depositions. The whole heater block was polished lightly with grinding paper to remove any surface damage or contamination from the ferric nitrate. Also, the heat shield was polished lightly to remove any

material deposited on to the shield during in previous depositions. After polishing both items were rinsed with acetone and blown dry with nitrogen.

It is important that substrates are clean, dust free, and have no scratches or chips on the surface to ensure the best possible surface for growth, mobility, and a consumate interface. The as-recieved substrates had been polished on one side. Each one was removed from its packaging and checked under an optical microscope for scratches and chips prior to deposition. Substrates were discarded unless they were totally scratch and chip free. A perfect substrate was cleaned in an ultrasonic bath for 10 minutes in acetone and then a further 20 minutes in ethanol. The substrate was rinsed with ethanol after each bath. Then the substrate was blown dry with nitrogen whilst being held on an optical lens tissue placed on a bed of standard tissue. The optical tissue ensured that the substrate stays dust free. The drying process was started as quickly after the washing process as possible to prevent ethanol from evaporating naturally and leaving a residue on the surface. Once the substrate was cleaned it was glued to the PLD heater using silver dag. At this stage the dag was painted onto the centre of the heater surface in excess and the substrate was placed onto the dag. The substrate was then gently pushed down into the dag using a cotton bud to produce a good thermal contact with the dag while ensuring that the dag did not rise above the surface of the substrate. The heater was then left to dry for at least 20 minutes before being inserted into the PLD chamber. A photo of a substrate glued to the heater can be seen in Fig. 2.16.

Laser irradiation severely alters the morphology of the PLD targets [31] surface causing outgrowths and in turn roughening, therefore, it is essential to clean and polish the target surface before every deposition to ensure there are no macroscopic particles in the plume and reproducible films are grown

[15, 23, 24]. All targets were polished using a rotary grinding disc with ethanol to lubricate the surface and prevent dust from spreading. The targets were held face down flat on the grinding disc, whilst rotating the target on the disc in the opposite direction to the motion of the disc. A coarse grinding paper was used first to abolish all trace of the laser track on the target and then a finer grinding paper to create a smooth polished surface on the target. One exception to this process is MgO which is transpaerent to UV radiation and so it is extremely difficult to grind away the laser track. In fact, as MgO is transparent to UV radiation only high laser fluences are enough to break the bonds and cause ablation; observation has shown that the presence of the laser track helps this process.

2.3.3 Laser Ablation

Before a deposition could be performed, a pre-ablation was carried out on each of the targets that were going to be used in the deposition. This was used to clean the target surface of any absorbed organic material left over from the polishing process. Pre-ablation was done in flowing oxygen at a pressure equal to that at which the actual ablation was to proceed. The heater was kept at room temperature and a shutter covered the substrate to prevent deposition. Every target was pre-ablated for 600 pulses at 5 Hz and the substrate was centred in the plume and moved to the correct distance away from the targets during this time. This was neccessary at this stage because the heater could not be moved during the deposition without destroying the alignment of the RHEED beam on the surface. Once pre-ablation was completed the chamber was pumped down to a base pressure of around 5×10^{-6} mbar.

In preparation for the deposition the shutter protecting the substrate was

opened, the heater temperature was set and the heater turned on. Oxygen was input at the deposition pressure once the heater had obtained 400°C to prevent loss of oxygen from the substrate at higher temperatures. If it was input before this temperature it was found to roughen the substrate surface in the early stages of the heating process. The RHEED was set up during the remainder of the heating and whilst temperature was stablising at the deposition temperature. The valve to the RHEED gun (Fig. 2.15) was opened and the beam current was raised to 35 kV in 5 kV increments, stopping for a few seconds between each increment. The beam current was increased to around 1.5 A, stopping at 0.3 A and 1.0 A for at least a minute each. The beam was aligned so that it passed directly through the pin-hole of the differential pumping tube and the spot size on the screen was maximized using the X and Y deflection, and the grid and focus circuits. The gun was then moved using the gun movement stage (Fig. 2.15) so that the beam began to graze the substrate surface and the specular intensity of the beam was maximised. The substrate was rotated azimuthally (ϕ) so that the beam was directed along $<100>$ and images were taken at various angles of incidence (θ) to check the quality of the substrate surface; these angles are shown in Fig. 2.16. The images from a high quality surface would show spots or streaks lying on Laue rings with Kikuchi lines intersecting the (00) peak. Once the heater temperature had stablised at the deposition temperature, the heater current was fixed at the average current required to keep that temperature. This was neccessary to prevent changing currents producing magnetic fields that deflect electrons from the RHEED. The gate valve (Fig. 2.14) position was also fixed to set the oxygen flow and prevent minute changes in flow effecting the intensity measurements. The azimuthal angle was altered so that the beam was along a direction of low symmetry. In

that condition, there were no peaks apart from the specular reflection and dynamical features such as Kikuchi lines were not seen. The evolution of the dynamical features during growth was found to cause anomalies in the RHEED intensity measurements. The peak intensity and a cross sectional image of the (00) reflection were measured as a function of time in all depositions. The former was used for deposition rate and growth mode analysis, whilst the latter was used to monitor movement in the specular reflection. Before deposition, the angle of incidence was set to give the greatest intensity, i.e. applying the in-phase condition, and the beam current was altered so that the peak intensity did not saturate the intensity measurement in the kSA 400 software package. The target for ablation was chosen, the laser was started at the correct pulse frequency and for the set number of pulses required. The intensity of the RHEED specular reflection was measured as a function of time for the duration of the deposition unless the intensity reached a steady state. In this case, the intensity measurement was stopped as no further useful data would be obtained.

This thesis is concerned with the growth of $SrTiO_3$ (STO) on MgO substrates, however to optimise deposition parameters and calibrate the number of pulses required for one monolayer, homoepitaxial growth was studied; two dimensional layer-by-layer growth is readily achieved in this case. The optimised parameters for all materials grown in this thesis are shown in Table 2.1. A homoepitaxial growth was performed to calibrate the deposition rate before each heteroepitaxial growth because uncertainties in energy measurements and deterioration of laser gases caused the number of pulses required for one monolayer to fluctuate over time. In an attempt to improve the crystalographic surface structure of MgO substrates 1000 pulses of MgO were deposited onto the surface of each MgO substrate at 5 Hz. The RHEED

Material	$SrTiO_3$	TiO_2	MgO
Fluence (J cm^{-2})	4	3	4
Temperature (°C)	850	850	850
Pressure (mbar)	1×10^{-1}	5×10^{-3}	1×10^{-1}
Pulse Frequency (Hz)	5 (100)	5	5
Target-Substrate Distance (mm)	45	45	45

Table 2.1: The growth parameters used for all films described in this thesis. Pulse frequencies in brackets were the frequencies used for PLID (see text).

intensity generally increased during this process suggesting a smoother surface with a higher crystalographic quality. The layer-by-layer growth mode is not favoured in the heteroepitaxial growth of STO on MgO for a number of reasons that will be dicussed in the next chapter. The technique used in this thesis to attempt to force a two dimensional growth mode is known as pulsed laser *interval* deposition (PLID) [16, 32]. PLID works on the principle of depositing exactly the correct number of pulses for a single unit cell layer onto the substrate at high pulse frequency so that the whole layer is deposited in a time less than the crystallisation time. The deposition of a single monolayer is followed by a pause in deposition allowing the adatoms to settle into a consumate layer before the next monolayer is deposited. This is done under the guidance of RHEED intensity data. As the adatoms are deposited, in this case at a pulse rate of 100 Hz, the specular intensity drops dramatically, then during the pause in deposition the intensity recovers exponentially as the layer crystalises to a steady state at which point the next layer can be deposited. A typical RHEED intensity measurement for this technique can be seen in Fig. 2.17. Another technique to improve the growth of STO on MgO is to control the starting layer of the STO structure. This

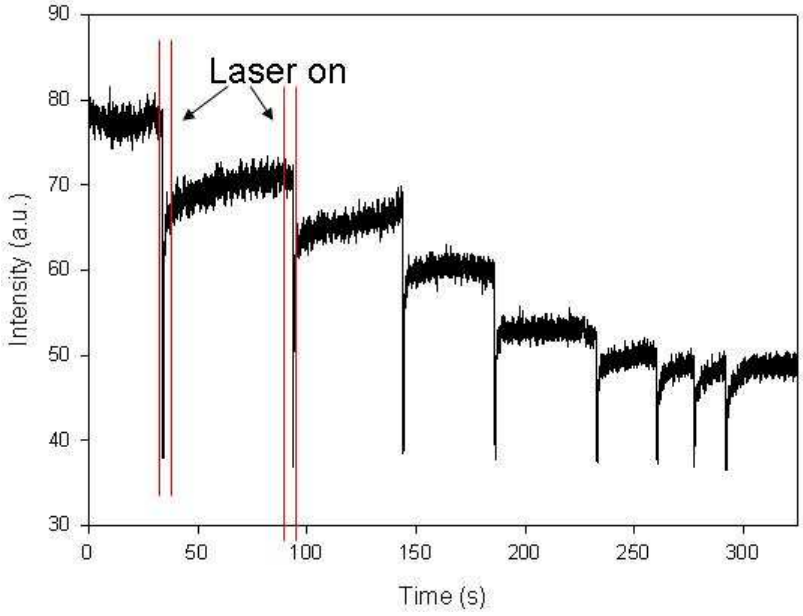

Figure 2.17: Typical RHEED intensity measurement during pulsed laser interval deposition of STO on MgO. The red lines indicate at which points material was deposited.

Growth Technique	Thickness (nm)	TiO_2 Buffer Layer
PLD	40	no
PLID	40	no
PLD	40	yes
PLID	40	yes

Table 2.2: Summary of films grown for comparison.

was done by depositing a single atomic layer of TiO_2 onto the MgO surface before STO, forcing TiO_2 to be the first layer. Films were grown with and without the TiO_2 buffer layer, in standard and interval deposition modes and then compared using a number of analysis techniques to determine the method of growth to produce the highest crystallographic quality possible. The heteroepitaxial films grown for comparison are summarised in Table 2.2.

Chapter 3

THIN FILM GROWTH

The growth processes of a film must be considered in order to understand the properties a film possesses and engineer a film for a specific task. The growth mode strongly influences whether the film has grains or is a single crystal, whether or not there is strain in the structure, how many defects there are and the type of defect, and the quality of interface between any layers there might be. A number of parameters can effect and determine the growth mode including lattice mismatch between the substrate and film materials, interface compatibility, time between laser pulses, the amount of material deposited in one pulse, and the surface mobility on substrate. These will be considered in this chapter along with the effects they have on the growth mode, microstructure and dielectric properties. Chapters 4 and 5 will refer to the theory described here, showing the influence of these parameters in the growth of STO on MgO.

3.1 Growth Modes

In general, there are three types of growth mode; two dimensional layer-by-layer (or Frank-van der Merwe), three dimensional island (or Volmer-Weber), and layer-by-layer superseded by three dimensional growth, Stranski-Krastanov

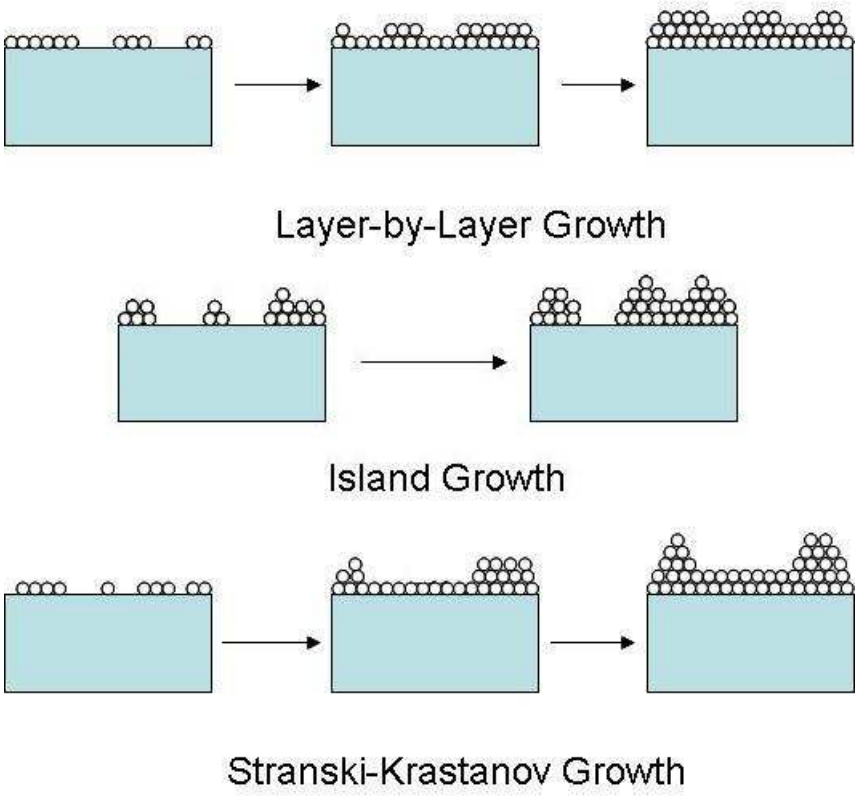

Figure 3.1: The three basic growth modes

[20]. An illustration of each of these modes can be seen in Fig. 3.1. The two dimensional layer-by-layer growth mode leads to the best crystallographic structure of the growing film. Here, stable nuclei grow two dimensionally outwards with the addition of adatoms, eventually coalescing and forming a unit cell thick layer. Once the previous layer is complete then nucleation and growth of the subsequent layer begins. The three dimensional island growth mode generally leads to more crystallographic disorder in the film with an increased number of defects and grain boundaries, and less consumate interfaces between film layers. Here, the stable nuclei absorb adatoms and grow out in three dimensions. This results in more than one monolayer being completed at the same time and the film continuing to grow in all directions.

The Stranski-Krastanov growth mode is an intermediate of the layer-by-layer and island growth modes. Here, the film starts with the initial layers growing in a two dimensional mode and at some point after the first monolayer energy considerations lead to the two dimensional mode being unfavourable and three dimensional islands begin to form. The growth mode of a film can be altered dramatically by adjusting the deposition parameters. However, there are also factors intrinsic to the combination of materials being used which influence, to perhaps a greater extent, the type of growth.

The deposition parameters affect the balance between the amount of material deposited in one laser pulse, surface mobility, and the time that the adatoms have to find stable sites in the new layer in between pulses [15, 16, 33]. This balance contributes somewhat to the growth mode of a film. The amount of material deposited in one pulse is controlled by a combination of laser spot size on the target, fluence, and background pressure; these determine the size of the plume and hence the amount of material reaching the substrate. The target-substrate distance is also a contributing factor to the amount of material deposited. Layer-by-layer growth is more likely when there is a small amount of material deposited in one pulse, and island growth becomes more probable with greater amounts of material deposited. This is due to there being a greater time required for all the adatoms to find stable sites at higher deposition rates. Surface mobility is effected by the substrate temperature, background pressure, fluence, and target substrate distance. At high temperatures there is a lower probability for adatoms to nucleate growth on top of existing islands and less time is required for all adatoms to find stable sites. However, at extremely high substrate temperatures re-evapouration of the adatoms from the surface can occur [20]. The laser pulse frequency determines the time that the adatoms

from one pulse have to find stable sites before the next pulse of adatoms arrives. Low pulse frequencies give adatoms more time to find stable sites at the edge of large two dimensional islands and allow for higher instantaneous deposition rates. High pulse frequencies promote high supersaturation and the formation of a high number of small islands reducing the probability of second layer island formation. However, if the deposition rate is too high at higher frequencies island growth is promoted because the adatoms from one pulse do not have time to settle into a single layer before the next pulse arrives. If the surface mobility is poor at lower pulse frequencies then island growth is promoted, also, because adatoms have a higher probability of nucleating second layer growth. Deposition parameters must be selected carefully to strike the correct balance between all of these factors to promote two dimensional layer-by-layer growth.

There are number of intrinsic properties that must be considered when studying the initial growth of heteroepitaxial films which can be placed into one of two main categories; lattice mismatch and interface compatibility. Lattice mismatch concerns the difference in in-plane lattice parameters between substrate and film layers which causes strain fields which can effect the growth mode of the growing film. The compatiblity of the interface between substrate and film, or even different layers of a heterostructure, depends on the crystallographic and chemical structure of the two materials and how well they fit together. In complex oxides the main factor in the compatibility problem is ion charge and the proximity of ions of the same charge [9, 10]. All these factors contribute to the change in free energy that arises from the growing film and it is this that ultimately decides the growth mode.

By considering, semi-quantitatively, this energy balance it is possible to understand the trade-off between energy terms that leads to the different

growth modes. Consider the case of a relaxed hemispherical island of radius r on top of a strained epitaxial layer. The condition for stability of this island gives the condition for the breakdown of layer-by-layer growth into Stranski-Krastinov growth. The net free energy for the nucleation of the hemispherical island on top of the growing strained epitaxial layer [20, 34] is given by

$$\Delta G = \frac{2\pi r^3}{3}\Delta G_v + \pi r^2 \gamma + \Delta G_s. \tag{3.1}$$

In equation (3.1) the first term represents the volume free energy of the relaxed island with respect to the flat, strained surface. The second term is the interfacial energy between the strained layer and the island. The final term is an energy that results from the difference in strain energy in the film layer after the island nucleates relative to that in the layer before island nucleation. Here, $\Delta G_s = \frac{1}{2}(\epsilon^2 - \mathrm{m}^2)YhA$ where ϵ is the mean misfit strain in the film after the island nucleates and m is the misfit, given by $[a_0(s) - a_0(f)]/a_0(f)$ where $a_0(s)$ and $a_0(f)$ are the lattice parameters of the unstrained substrate and film respectively. Y is the Young's modulus of the layer, h is the thickness of the epitaxial layer, and A ($= \pi r^2$) is the area affected by the strain. The condition for a stable island nucleus which will not dissociate is $d\Delta G/dr = 0$. This critcal radius is given by

$$r^* = -\frac{\left[\gamma + \frac{1}{2}(\epsilon^2 - \mathrm{m}^2)Yh\right]}{\Delta G_v}, \tag{3.2}$$

and from this, the critical thickness for the onset of Stranski-Krastanov growth can be calculated. In the limit $r^* = 0$,

$$h^* = \frac{2\gamma}{(\epsilon^2 - \mathrm{m}^2)Y}. \tag{3.3}$$

When the surface energy of the substrate material is less than that of the film island growth clearly dominates but with the introduction of misfit strain the range of this regime expands. Layer-by-layer growth can only

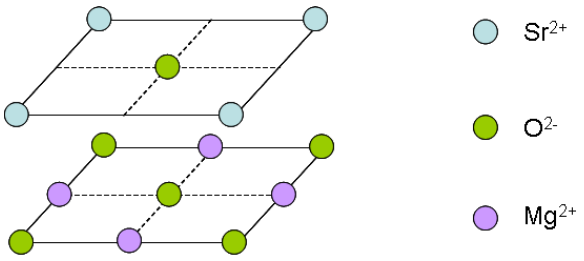

Figure 3.2: The atomic arrangement at the STO/MgO interface if SrO was the intial plane of cube-on-cube epitaxy. Strontium ions are blue, oxygen ions are green and magnesium ions are purple.

occur when the surface energy of the film is lower than that of the substrate. In this case, a small amount of strain can be accomodated by the layer. The Stranski-Krastanov mode lies between layer-by-layer and island growth; the thickness at which islands start to form depends both on misfit strain and the interface energy between the substrate and film as shown in equation (3.3).

The growth of STO on MgO requires an additional term in equation (3.1); the energy cost associated with interface chemistry [9, 35]. If the film begins with the SrO layer then the interface energy is large and the layer is unstable, resulting in a three dimensional island growth in the first layer. The closest, matched orientation of SrO on MgO is stacked in a cube-on-cube fashion on the MgO (100) surface, however, in this case there are large numbers of like-charged ions in nearest neighbour positions, as seen in Fig. 3.2. The repulsion caused by this greatly increases the interface energy and leads to an inherent instability. If the SrO was stacked on an MgO surface oriented 45° to cube-on-cube, i.e. so that the octahedra of oxygen surrounding the Mg^{2+} in the MgO align with the octahedra of the STO structure, the issue of near-neighbour like-charged ions is removed. However, within the MgO structure the O-O distances are near close packed

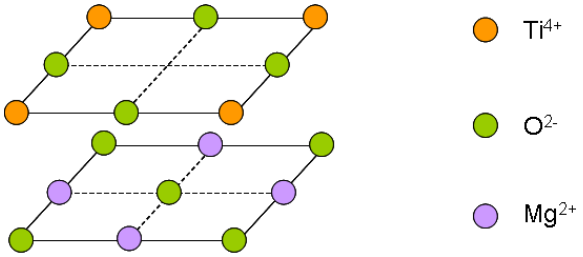

Figure 3.3: The atomic arrangement at the STO/MgO interface if TiO_2 was the initial plane of cube-on-cube epitaxy. Titanium ions are orange, oxygen are green, and magnesium are purple.

separation for O^{2-} with the small Mg^{2+} ions fitting into the interstices. Sr^{2+} ions are much larger causing the O-O distances in the SrO plane to be greater than that in MgO by around 34%; the large lattice energy increase as a result of simple strontium-ion substitution of the magnesium ions would also make this an unstable configuration. In contrast, the TiO_2 plane of STO can form a comensurate layer on MgO with alternate Ti^{4+} rows being vacant over the underlying Mg^{2+} sites, as can be seen in Fig. 3.3. The requirement of anion-cation near neighbour pairs is statisfied and with this intial plane, STO can sit epitaxially cube-on-cube with MgO in a low energy, stable configuration. The missing cation rows leave stable sites for the subsequent strontium-ion attachment and a comensurate interface and intial layers are more probable than with a starting SrO plane. The deposition of an atomically thin TiO_2 layer will force the stacking sequence of STO to be the more energetically favourable one.

3.2 Microstructure

The growth mode of a film determines the general microstructure of the film; whether it has grains, dislocations or other types of defects, and whether

there are strain fields within the structure of the film. Strain due to lattice mismatch is more likely to be introduced into a film with a growth mode that has a greater two dimensionality [36] (Appendix 2). Films grown in a three dimensional island growth mode have greater densities of defects which relax the strain. In the following sections, strain, defects, and their consequences on the physical properties of the film will be discussed in more detail.

3.2.1 Strain

Strain can be induced in thin films close to the film/substrate interface as a result of the lattice mismatch in epitaxial growth. The initial layers of a film stretch or compress to match the substrate's lattice parameters until the stored elastic energy in the thin film becomes too high. At this point dislocations form and/or island growth is initiated to relieve some or all of the stress. Strained layers in ferroelectric films can have a strong effect on the dielectric properties. STO has a lattice parameter of 3.905 Å and MgO of 4.213 Å. If the strain is not relieved by some mechanism, an MgO substrate puts an STO film in tension in-plane. The biaxial strain caused by the lattice mismatch leads to a tetragonality with a smaller c-parameter than a-parameter and it is easy to see that this would effect the polarisability of the material. A complex phase diagram is seen as a function of misfit and temperature [37]. In the simplest case, strain will shift T_c and strain gradients will smear and depress the divergence of the permittivity with temperature [38, 39]. It has also been shown that local strain can alter the dielectric loss by effecting the phase difference between the ionic motion and an applied electric field [12]. Strain is relaxed by lattice defects which cause local strain fields but the question of whether strain gradients are present in the bulk of the film depends on the defect structure.

Strain can be seen as part of a group of microstructural phenomenon known as "dead-layers" that are detrimental to the dielectric properties of thin films. There are several possible causes of the dead-layer effect and much debate over which are important. Depletion layers due to metal electrodes [40] are not relevant for this thesis as the films studied are intended for use in complex oxide high T_c superconductor devices. There has been doubt cast on the validity of the size effect leading to dead-layers in surface regions due to boundary conditions and depolarising fields [11, 12, 41]. Dielectric measurements of ferroelectric single crystals thinned down to thin film dimensions [39] have yielded a dielectric response very similar to that of bulk.

3.2.2 Defects

Strain energy caused by lattice mismatch is relieved by the formation of defects [20]. Initially, an epitaxial film will grow pseudomorphically, straining elastically to the lattice parameters of the substrate, creating a coherent film/substrate interface. As the film grows the strain energy increases until a critical thickness, d_c, at which the energy to have a strained film exceeds the energy of a relaxed film with an array of dislocations. When this happens dislocations are introduced into the film structure and some of the strain is relieved. As the film continues to grow thicker, more and more dislocations are introduced until the misfit strain is completely relieved. Expressions for the strain energy at thicknesses above and below d_c were given by Nix [20]. It is assumed in this treatment that the film and substrate have equal Young's moduli (Y) and and shear moduli (μ). In the regime where $d < d_c$ the elastic strain energy per unit area is given by

$$E_e = \frac{Y d \epsilon^2}{(1-\nu)}, \tag{3.4}$$

where ϵ is the biaxial elastic strain and ν is Poisson's ratio. It is clear to see that the strain energy increases linearly with film thickness in this regime and no dislocations are incorporated in the film. Now consider the case where $d > d_c$. Dislocations form at the film/substrate interface to relieve the strain energy that develops during further film growth. If the dislocations are arranged in a square grid of side S then the elastic strain energy is reduced from its initial value as the elastic strain is reduced by the dislocations to $\epsilon = \mathrm{m} - b/S$ where b is the magnitude or strength of the Burgers vector. The value of b/S is proportional to the number of dislocations at the interface and when it is equal to m the bulk strain in the film vanishes. The total strain energy per unit area in this regime is given by

$$E_T = \frac{Yd(\mathrm{m} - b/S)^2}{(1-\nu)} + \frac{\mu b^2 2\ln(\beta d/b)}{4\pi(1-\nu)S}, \tag{3.5}$$

where the first term represents the elastic strain in the bulk of the film and the second represents the dislocation energy. In equation (3.5), β is a constant relating the radius of the strain field surrounding the dislocation to the thickness of the film. This equation shows that strain energy increases linearly with film thickness whilst dislocation energy has a very weak logarithmic dependence of thickness making it almost constant. The critical film thickness can be calculated by minimising the total energy with respect to dislocation number and evaluating at $b/S = 0$:

$$d_c = \frac{b}{8\pi(1+\nu)\mathrm{m}} \ln\left(\frac{\beta d_c}{b}\right). \tag{3.6}$$

For a low mismatched system such as a $YBa_2Cu_3O_{7\text{-}x}$(YBCO) film on a STO substrate (m = 0.01) $d_c \approx 5$ nm. However, for a high mismatch system such as STO on MgO (m = 0.075) the strain energy is far too large and dislocations are expected to be introduced from the initial layers. This will be discussed further in chapter 5. These calculations were done using the

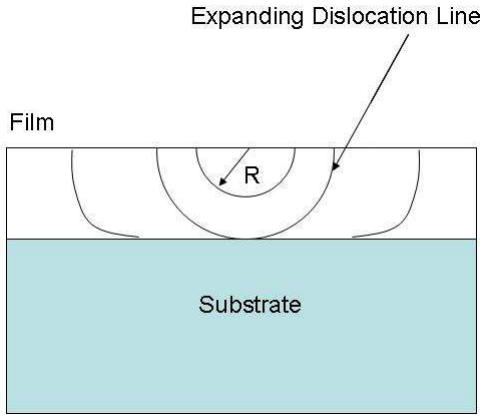

Figure 3.4: The glide of a threading dislocation half-loop gliding down to the interface and outwards with increasing film thickness, leaving behind a misfit dislocation.

bulk STO value of Poisson's ratio [42] and assuming the magnitude of the Burgers vector to be of the order of the bulk lattice parameter for STO.

Threading dislocations have a dislocation line that threads through the film and nucleate at the film surface as a half-loop [20, 43]. As the film grows the stress drives the dislocation line to glide and bend in a slip plane until, at d_c, it is able to glide infinitely leaving behind a misfit dislocation at the substrate/film interface. This is shown in Fig. 3.4. In reality, the thickness at which dislocations are introduced can be greater than the predicted values due to a number of reasons including an absence of a suitable glide system, interactions between dislocations and other defects, and the energy barrier associated with dislocation nucleation. The nucleation of a dislocation loop will now be examined along with the energy considerations involved. There is an energy increase in the system associated with creating the half-loop but also a decrease in the system energy due to the relief of some strain. Also, if the loop is imperfect with a stacking fault included causing a surface step, there will be an increase in system energy due to the stacking fault itself and

the additional surface energy involved in the creation of a step. The sum of these energies increase with half-loop radius until a critcal radius is reached, at which point the system energy begins to decrease and the dislocation becomes favourable. The energy associated with this critical radius is the activation energy of dislocation nucleation. If the film is not of a thickness where a half-loop of critical size can fit into the film, then nucleation will not occur and the film will remain strained even if a relaxed structure is more favourable. Matthews [43] showed, however, that the critical thickness for half-loop nucleation usually agrees fairly well with d_c. This is the case with an exceptionally clean film but vacancies, impurites, and other local phenomenon can push nucleation to occur before the film reaches critical thickness by increasing the strain energy locally. Threading dislocations in the film can also nucleate at the substrate interface or extend from a threading dislocation present in the substrate. However, in this case the dislocation slips in the opposite direction in the film due to the stresses acting on it being opposite. This scenario is shown in Fig. 3.5.

As the film thickness increases, more and more strain is relaxed through the formation of misfit dislocations and this therefore effects the dielectric properties. As discussed above in section 3.2.1, strain alters the Curie temperature; it follows that as the thickness of the film increases, the Curie temperature relaxes towards the bulk value due to the change in strain caused by the formation of dislocations [44]. The disruption to the crystal periodicity that dislocations cause obviously produce a strain field surrounding the dislocation line. An array of dislocations therefore produces local strain gradients throughout the film which in turn broaden the ferroelectric transition [38]. The extent to which these phenomenon will effect device performance much depends on the geometry of the device. Coplanar devices will be ef-

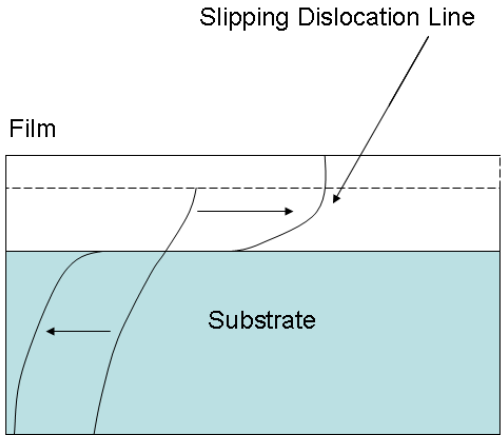

Figure 3.5: The elongation with increasing film thickness of a threading dislocation extended from the substrate to create a misfit dislocation at the interface.

fected more by the presence of threading dislocations than misfit dislocations at the film/substrate interface, for example.

3.2.3 Cracks

In-plane lattice mismatch not only results in misfit dislocations but can also lead to the formation of microcracks [45]. The exact process in which crack formation actually occurs is still unknown but differences in thermal expansion coefficients, temperature gradients, and substantial lattice mismatch are some of the commonly attributed causes. It is assumed that the elastic strain in the film drives the formation and growth of cracks. For the purpose of this discussion it is assumed that the elastic strain arises purely from lattice mismatch and local strain fields caused by film inhomogeneities will be ignored. As with the case concerned with dislocations, the strain energy in the film increases to a point where crack formation will become favourable.

The elastic strain in the mismatched film is given by

$$\epsilon = \frac{[a_0(s) - a_0(f)]}{a_0(f)} - \delta, \tag{3.7}$$

where δ is the strain relieved by the formation of other defects. The amount of strain energy that can be relieved per unit length of a two dimensional crack that penetrates the whole thickness of the film is

$$E_c = \pi Y \epsilon^2 (d/2)^2, \tag{3.8}$$

where d is the crack height, i.e. the thickness of the film. The formation of a crack is energetically favourable when E_c exceeds the energy for the formation of the new surfaces per unit crack length, E_s. The surface energy per unit crack area is defined as $E_s^* = E_s/d$ which, in turn, leads to a critcal thickness for crack formation becoming favourable:

$$d_c' = \frac{4E_s^*}{\pi Y \epsilon^2}. \tag{3.9}$$

An estimate value for the crack surface energy for a perovskite is $E_s^* = 340$ J m^{-2} [45] which leads to a critical thickness for crack formation in a STO film on an MgO substrate of 319 nm. The Young's Modulus was taken to be that of bulk STO [46] and assumes the very unlikely case of no strain relief by dislocations. Thus, in general it is expected that dislocations nucleate at smaller film thickness and cracking is not usually the mechanism of strain relief.

An array of cracks in a film clearly produces a series of air gaps which effect the permittivity. The film correspondingly has an effective permittivity lower than the bulk permittivity due to a volume fraction of the film having the permittivity of air which is unity [47]. These film components can be modelled in a series-capicitor geometry. Also, cracks relieve stress locally producing strain gradients which, as shown in the above section on strain, can also be detrimental to the dielectric repsonse.

3.3 Pulsed Laser Interval Depostion

Pulsed laser interval deposition (PLID) [16, 32, 48], introduced in chapter 2, uses the kinetics of the PLD setup to encourage layer-by-layer growth and improve the crystallographic structure. The technique exploits the high supersaturation and large number of small two dimensional islands that goes hand in hand with high pulse frequencies. Deposition parameters are selected so that a high number of pulses, typically around 50, are required to deposit sufficient material for one unit cell monolayer; this ensures a low error on the amount of material deposited from an integer number of pulses. One monolayer is deposited at a high pulse frequency, typically 60 Hz, which is then followed by a period of no deposition. The correct amount of material for one monolayer is deposited in under the relaxation time and nucleation mainly takes place after the depostion has occured. The high supersaturation of mobile adatoms on the surface after the deposition pulse favours a high nucleation density. Premature nucleation is avoided and the small size of the nuclei formed discourage second level nucleation by making the incorporation of adatoms at step edges most likely. Once the adatoms have reached stable sites and the RHEED intensity has recovered to a steady state, which is due to the descrease in the number of mobile adatoms, the next monolayer is deposited and this process begins again. It is clear to see how this technique increases the probability of layer-by-layer growth, even in material combinations where it is usually not favourable.

Chapter 4

HOMOEPITAXIAL GROWTH OF STRONTIUM TITANATE

Homoepitaxial growth of STO was mainly used for the measurement of deposition rate using the period of the RHEED oscillations. It was also used for optimisation of the interval deposition technique for the application to the heteroepitaxial system. However, as will be seen, it is far from easy to achieve a layer-by-layer growth and, hence, a growth rate measurement using RHEED, if the deposition parameters are not carefully chosen to give the correct deposition rate. One vital piece of information that is usually neglected in the literature is the laser spot size on the target. It will become obvious in this chapter that this is one of the most important parameters that decides the deposition rate. This chapter will describe the experiment results and the evolution of understanding that came from these to give the final optimised parameters used in heteroepitaxy. Also, RHEED and transmission electron microscopy (TEM) analysis will be shown and discussed from the homoepitaxial films grown using the final parameters in both standard and interval deposition regimes.

4.1 Spot Size and Deposition Rate

The PLD setup for the intial work of this thesis was somewhat different to that described in chapter 2 and used to deposit the films described in chapter 5. There were homogeniser elements in the beam path which fixed the laser spot size on the target at 2×4 mm^2. The reason for the use of these elements were to create a homogeneous beam profile, by taking in the whole beam, dividing it up into 24 smaller rectangular beams, each of even energy across their area, and orienting them onto the target so that they overlapped, leading to a spot of fixed size but homogeneous profile. This large spot size gave a bigger plume than the main setup decribed in chapter 2, which required the larger target substrate distance of 55 mm. The deposition rate was of the order of an angstrom per laser pulse. These were the standard conditions used in the laboratory since 1994 for the growth of high temperature superconductors, ferroelectric, and ferromagnetic oxides. In fact, similar conditions are used in most laboratories worldwide that do not have RHEED [15, 49, 50, 51].

With this setup RHEED oscillations were not observed under any deposition conditions examined and typical RHEED intensity measurements yielded a gentle decline of the specular intensity as a function of time. The RHEED intensity measurement and RHEED diffraction patterns of the final film surface for typical conditions for the best growth with this setup are shown in Fig. 4.1 and Fig. 4.2 respecitively. The deposition conditions used in the growth shown here are summarised in Table 4.2. These conditions put the substrate on the edge of the visible plume which is where stoichiometric deposition occurs. Although the RHEED intensity measurements show the film growth modes were in the island regime, the RHEED pattern exhibits spots lying on Laue circles and the presence of Kikuchi lines indicating an

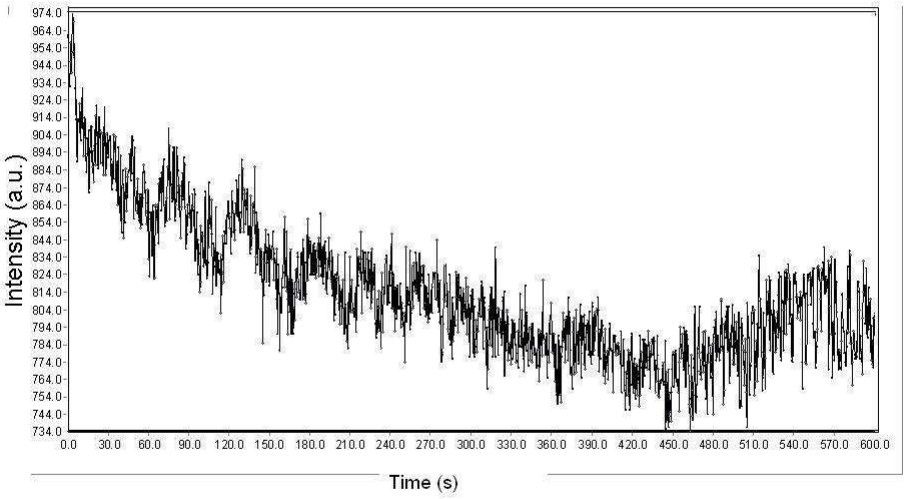

Figure 4.1: Typical RHEED intensity as a function of time for a homoepitaxial STO deposition with a large laser spot on the target.

Fluence (J cm^{-2})	1.5
Temperature (°C)	800
O_2Partial Pressure (mbar)	0.5
Laser Pulse Frequency (Hz)	1
Target - Substrate Distance (mm)	55
Number of Pulses	1000
O_2Cooling Pressure (mbar)	100
Cooling Ramp Rate (°C min^{-1})	30

Table 4.2: Typical deposition conditions for best growth with a large laser spot on the target.

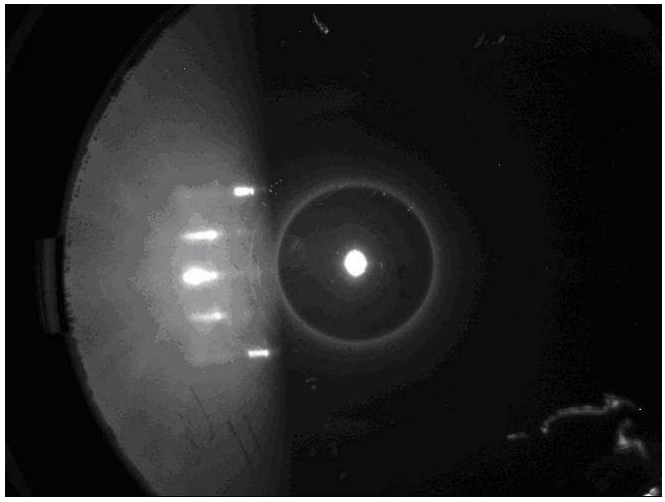

Figure 4.2: RHEED pattern along <110> of a surface of a homoepitaxial STO film grown under typical deposition parameters for the large laser spot on the target

atomically smooth and ordered surface.

In an attempt to understand the lack of RHEED intensity oscillations the thickness per pulse as a function of fluence was calculated. The deposition parameters were kept the same as those in Table 4.2 throughout and the fluence was altered. The film thickness was measured by patterning a step into the film by photolithography and ion beam milling down to the substrate. A profilometer was then used to measure the thickness at a number of points along the step and the thickness averaged. A plot of thickness per pulse versus fluence is shown in Fig. 4.3. Comparing the lowest deposition rate given by this setup, 0.113 ± 0.34 nm per pulse, to the literature [16, 32, 48, 52, 53] it is obvious that the growth rate given by such a large laser spot size is too high to give growth oscillations. The deposition rate observed requires only less than 4 pulses for the deposition of a complete monolayer of material whereas oscillations are observed in the literature for

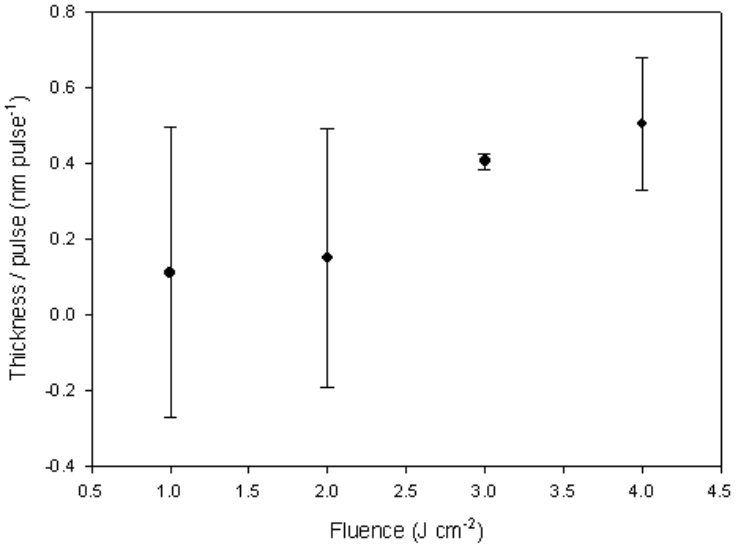

Figure 4.3: The thickness per pulse for growth with the larger laser spot size.

no less than around 20 pulses per monolayer. With the large spot size there was simply too much material every pulse to rearrange and crystalise into a two dimensional layer before the next pulse arrived. It is common in the literature [16, 32, 48, 52, 53] for a low pressure of oxygen to be used in deposition for high surface mobility. This, in combination with low deposition rates achieved by use of a small spot size and low fluence favours layer-by-layer growth. However, the films grown in this thesis are intended for use in microwave devices and so a higher oxygen pressure is required in deposition to better oxygenate the films.

To reduce the deposition rate the laser spot size on the target was reduced by altering the optical setup of the system. Removal of the homogenizer elements was essential as these fixed the spot size on the target and instead an aperture was used to take the most homogeneous central part of the laser beam. This part of the beam was then focused down onto the target to a much smaller size of 1.55×0.85 mm^2; this is the setup described in Chapter

Fluence (J cm^{-2})	2
Temperature (°C)	850
O_2 Partial Pressure (mbar)	0.1
Target - Substrate Distance (mm)	45
Laser Pulse Rate (Hz)	5

Table 4.3: Initial deposition parameters that caused layer-by-layer growth.

2. Re-optimisation of the other deposition parameters was then required to account for the change in plume size and find an optimal deposition rate. When the smaller spot size was used in conjunction with the parameters described in Table 4.2 a very small plume was produced. To counter this the substrate-target distance was decreased to the limit of the system to bring the substrate further into the plume. Also, the fluence was increased and the oxygen pressure was decreased to increase the size of the plume.

4.2 RHEED Oscillations and Optimisation of Interval Deposition

The new smaller laser spot setup quickly yielded RHEED oscillations corresponding to two dimensional layer-by-layer growth as shown in Fig. 4.4. The deposition conditions used to achieve this growth are summarised in Table 4.3. This gave a deposition rate of 86 pulses per monolayer deposited and was reproducible from deposition to deposition with an error in deposition rate of less than 10 pulses per monolayer. This was most likely due to error in system motor movement and a small plume that made the deposition rate extremely sensitive to variations in target - substrate distance. This was later improved by increasing the fluence further to provide a larger plume and thus making it less sensitive to variations in distances, however, there

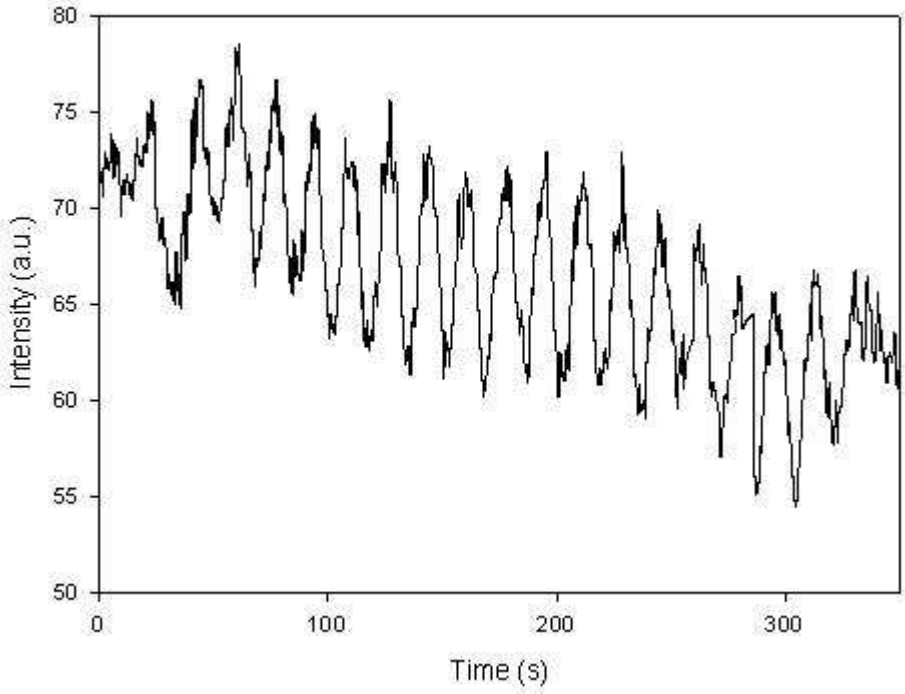

Figure 4.4: RHEED oscillations indicating layer-by-layer growth of homoepitaxial STO with a growth rate of 86 pulses per monolayer.

could still be errors in deposition rates of 1 or 2 pulses per monolayer over time. This is the reason for a deposition rate check using homoepitaxy before each interval deposition took place.

Optimisation of the PLID technique was required to ensure that there was the correct number of pulses in a monolayer interval at high and low laser pulse frequencies. The layer-by-layer standard homoepitaxial deposition was performed at a laser pulse rate of 5 Hz whereas the PLID was performed at 60 Hz. The drop in energy with increasing pulse rate is a characteristic of excimer lasers. The interval technique would not work if there were not the correct number of pulses to form a monolayer in each burst. Roughening would occur with each interval deposited. This optimisation required first depositing in standard mode and stopping deposition on a peak of a RHEED oscillation; this ensured that the top surface was a complete monolayer and was as smooth as possible. Then, moving to high frequency, one interval of the number of pulses corresponding to a monolayer at low frequency was deposited. Finally, deposition at low frequency in standard mode was started again. If this second round of standard deposition started on a peak of an oscillation then there was the correct number of pulses in the high frequency interval to deposit one monolayer. It was soon noted, during the initial optimisation depositions, that when depositing at the same laser voltage a higher number of pulses was indeed required to deposit one monolayer at high frequency. The extra pulses required were due to the output laser energy decreasing with increasing pulse frequency at constant voltage. For example, to have a fluence of 4 J cm^{-2} on the target at 5 Hz a voltage of 20.6 kV was required, however, to achieve the same fluence at 60 Hz a voltage of 22 kV was required. Once this was taken into account and the laser voltage adjusted at high pulse frequency to produce the same laser energy as at low

frequency the number of pulses required to deposit one monolayer at high and low pulse frequencies equalled each other. This is an experimental detail generally omitted in the literature.

4.3 Comparison of Films Grown by Standard and Interval Techniques

The deposition parameters were optimised and the homoepitaxial films grown by the standard and interval deposition methods were compared [36]. The parameters used are summarised in Table 4.3, however, the energy was adjusted so that there were a comparable number of pulses needed for the completion of one monolayer in both depositions.

4.3.1 RHEED Analysis

Standard PLD yielded oscillations of the RHEED intensity as a function of time, seen in Fig. 4.5, which are clear evidence of a two dimensional layer-by-layer growth mode. It should be noted that the oscillations presented here are much smoother and less noisy than those grown with the initial conditions shown in Fig. 4.4 due to the optimised growth conditions. Calculation using the period of the RHEED oscillations gave a deposition rate of 50 pulses per monolayer deposited. The relatively constant baseline of the oscillations and the lack of damping in the oscillations suggests that a true layer-by-layer growth was occuring where one layer completes before the next begins and these could continue for a very long time [26]. The oscillations do not show any evidence of modulation by the laser pulsing. Such modulations have been observed elsewhere [16, 48] and were explained by the high density of mobile adatoms on the surface after each pulse. Modulations such as these

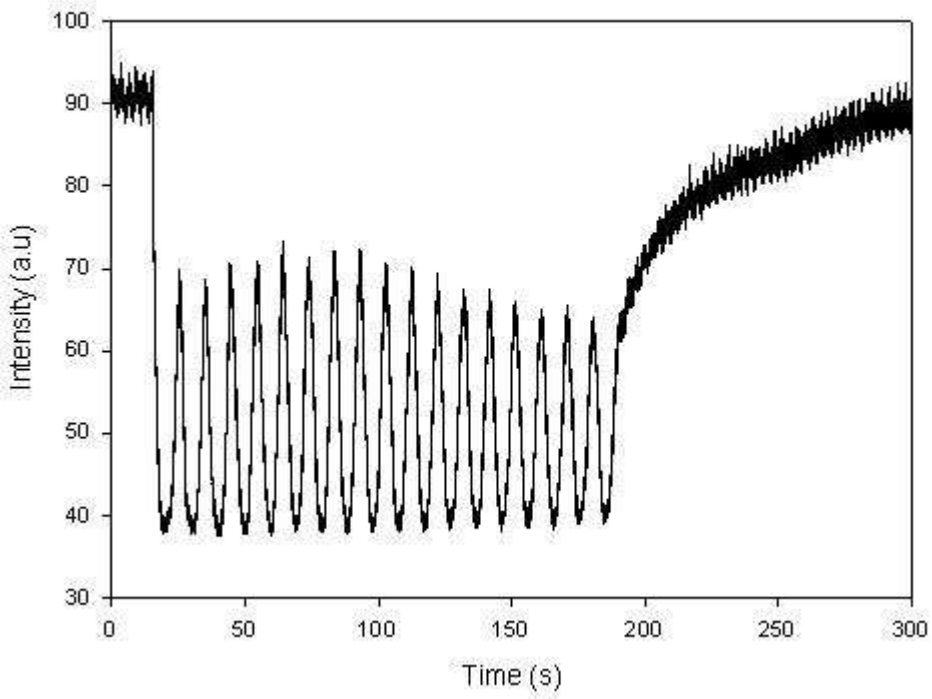

Figure 4.5: RHEED oscillations indicating layer-by-layer growth in homoepitaxy for optimised conditions.

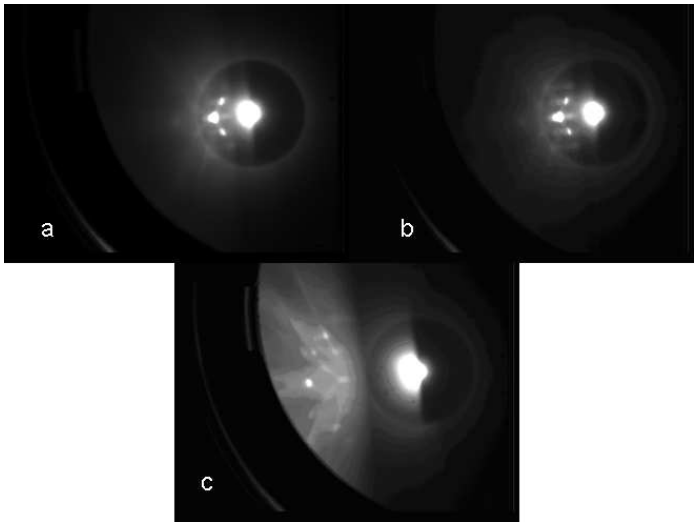

Figure 4.6: RHEED patterns taken along <100> before and after standard deposition of a homoepitaxial layer. Patterns from the substrate, (a), and from the film surface, with an angle of incidence of ~1°,(b), and ~3° (c).

are also predicted by the RHEED oscillation theory presented in chapter 2. In the present work it is suspected that the large number of pulses per monolayer and the limited temporal resolution of the RHEED camera probably explain the lack of any modulation. Fig. 4.6 shows the RHEED patterns of the substrate and film surfaces for the standard deposition. The diffraction pattern of the film (Fig. 4.6(b)) is very similar to that of the substrate (Fig. 4.6(a)) suggesting that it is of the same crystallographic quality. Kikuchi lines are present in both, with spots lying on Laue rings. These two features evidence a very well ordered smooth surface. In addition to this, the presence of diffraction spots and Kikuchi lines at high angles of incidence (Fig. 4.6(c)) suggest a highly crystaline, smooth surface.

The RHEED intensity as a function of time for the PLID is shown in Fig. 4.7. There were 20 monolayers deposited although only the first 5 can be distinguished by a definite drop in RHEED intensity followed by

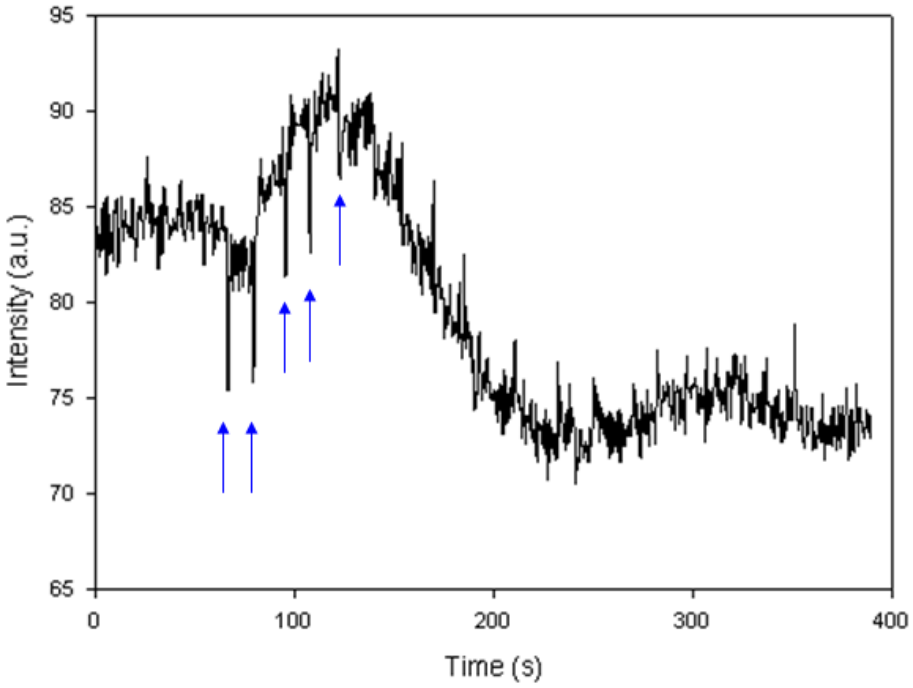

Figure 4.7: RHEED specular intensity as a function of time for homoepitaxial interval deposition. The blue arrows indicate the first 5 monolayers deposited.

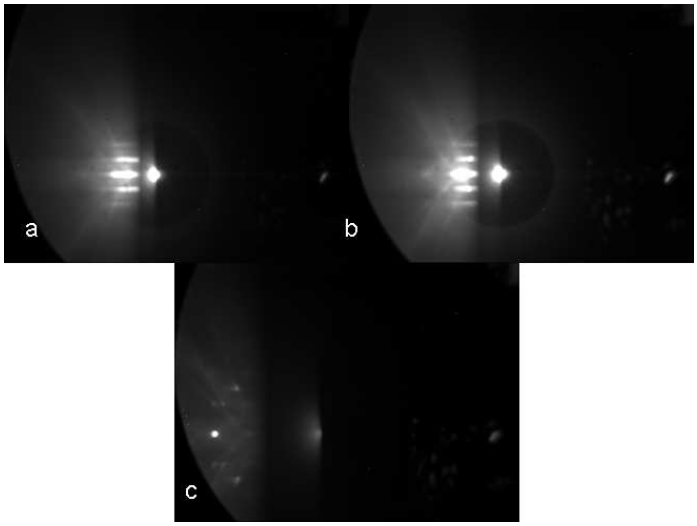

Figure 4.8: RHEED patterns along <100> before and after interval deposition of a homoepitaxial layer. Patterns of the substrate, (a), and the surface of the film at an angle of incidence of ~1°, (b), and at an angle of incidence of ~3.5°, (c).

a recovery. The lack of clear intervals in the RHEED intensity could be an indication of poor interval optimisation. The figure is made harder to interpret by the fact the intensity increased after deposition of each of the first 4 monolayers, suggesting that the surface quality was improving, but the decreasing intensity after the first 5 monolayers suggests that the surface quality was deteriorating. An examination of the RHEED patterns before and after growth, seen in Fig. 4.8, shows that, crystallographically, the film surface is similar if not more ordered than that of the substrate. The presence of streaky spots lying on a Laue ring with Kikuchi lines showed a well ordered, smooth surface for both the substrate (Fig. 4.8(a)) and the film surface (Fig. 4.8(b)). From the patterns presented here the substrate appeared to have a more streaky pattern, and hence, less well ordered surface than the film surface with Kikuchi lines appearing more prominent on the

film surface pattern. However, it must be pointed out that these differences could just be due to the angle of incidence and beam intensity differing slightly. The film surface was at least as high quality if not better than the substrate surface and this is backed up by the presence of diffraction spots and Kikuchi lines at high angles of incidence (Fig. 4.8(c)). The high quality film surface suggests that the interval optimisation was correct and the lack of features in the RHEED intensity measurement is most likely due to dynamical effects, described in chapter 2, interfering with the intensity of the specular reflection.

4.3.2 TEM Analysis and Comparison with Previous Work

All TEM analysis in this thesis was undertaken by Dr. Yau Yau Tse in the Department of Metallurgy and Materials. The TEM cross-sectional bright field images of the samples grown by PLD and PLID are shown in Fig. 4.9 with g=002. For these images the sample was tilted to the two-beam condition so that only the straight through and the (002) diffracted beams were visible. In both cases the interfaces were consumate and the microstructures were extremely similar. Fig. 4.10 shows a high-resolution TEM image taken along [010] of the film grown by standard deposition. The interface between film and substrate is perfectly coherent. There were no misfit or threading dislocations observed in either film. This TEM analysis combined with the RHEED results shows there was a two dimensional layer-by-layer growth using both deposition methods.

In comparison to previous work by this group [50, 54] which used the "large-spot" setup, the films grown here had a greater crystallinity and a more homogeneous microstructure. Tse et al. [50] reported columnar growth for all laser pulse frequencies investigated as shown in Fig. 4.11. The high

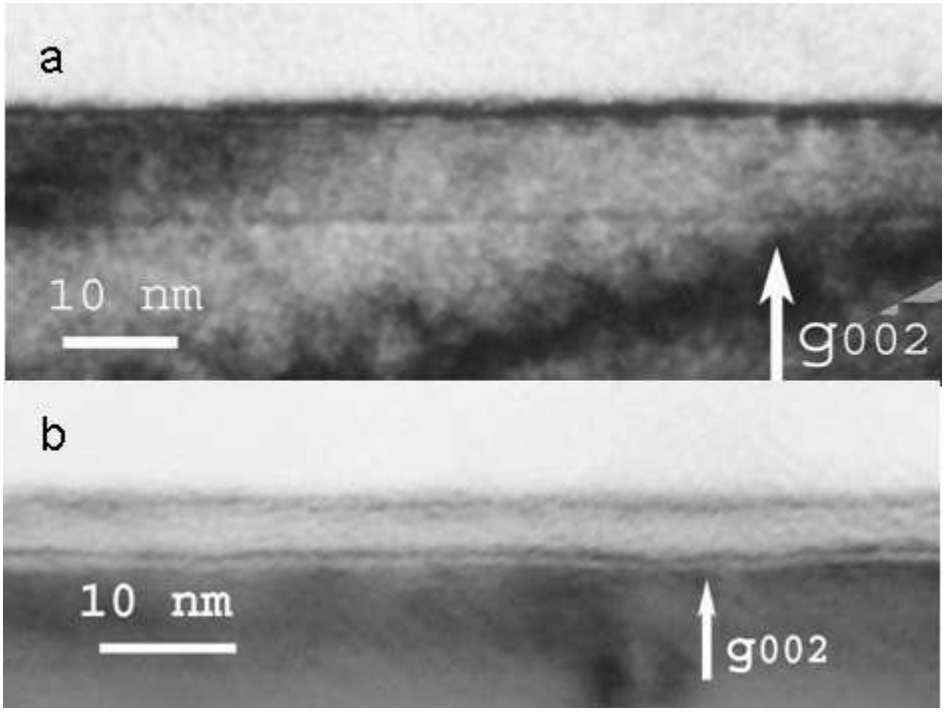

Figure 4.9: Cross-sectional bright field TEM images of homoepitaxial samples grown by PLD, (a), and PLID, (b), with g = 002.

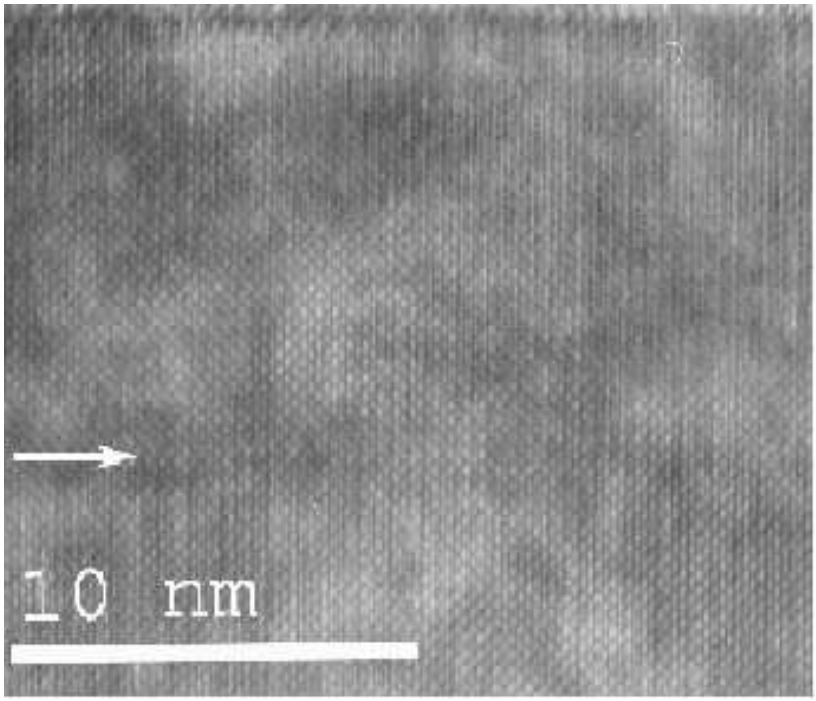

Figure 4.10: Cross-sectional high-resolution TEM of a homoepitaxial film grown by standard deposition.

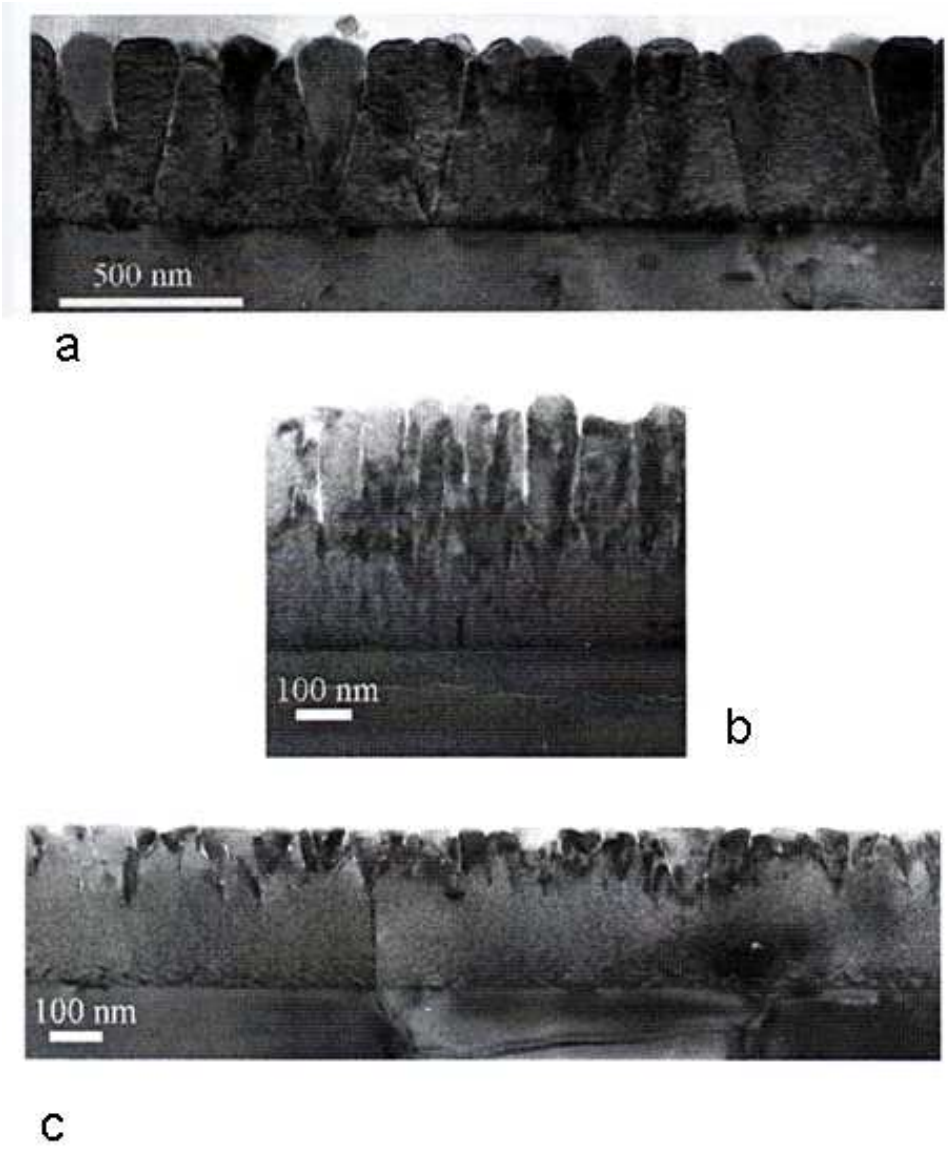

Figure 4.11: Cross-sectional bright field TEM images of homoepitaxial films grown by Tse et al. [50] at 0.15, (a), 1, (b), and 100 Hz, (c).

deposition rates reported do not allow sufficient time for single layer crystalisation to occur in between pulses. The highest deposition per pulse was observed in the sample grown at 0.15 Hz and was the most columnar. The lowest deposition per pulse was observed in the sample grown at 100 Hz and had the most homogeneous microstructure with columns appearing late in the growth. It is easy to see that lower instantaneous deposition rates provide growth with greater crystal quality. Films grown for this thesis with the smaller laser spot exhibited a true two dimensional growth whereas the films grown by Tse et al. clearly had a three dimensional growth mode with the presence of columns, dislocations, and off-stoichiometry inclusions in the structure. None of these features were observed in the films grown with a small spot size.

4.4 Summary

It has been shown that a two dimensional layer-by-layer growth can be easily achieved, in both standard and interval modes, only if the deposition parameters are carefully selected to provide a low deposition rate. A small spot size allows a low deposition rate whilst working at fluences which are high above the ablation threshold and pressures favourable for oxygenation of the film. The conditions allow single layer crystallisation to occur before the next pulse arrives. A high substrate temperature maximises surface mobility and favours two dimensional growth. RHEED data showed the high crystalline quality of films grown by both interval and standard deposition. TEM analysis shows a consumate interface between film and substrate with no threading or misfit dislocations observed. Films grown by both interval and standard deposition exhibit the same high quality structure.

Chapter 5

HETEROEPITAXIAL GROWTH OF STRONTIUM TITANATE ON MAGNESIUM OXIDE SUBSTRATES

Films of $SrTiO_3$ (STO) on MgO substrates have the potential to be very useful in applications such as microwave device circuitry. The high dielectric tunability of STO and low dielectric loss of MgO makes the architecture seem ideal. However, STO on MgO is not a well lattice matched system with both a high mismatch of lattice parameters and interfacial chemical incompatibility issues being present [9, 10, 35]. These two issues dramatically effect the growth mode and hence, the microstructure of an STO film grown on an MgO substrate. The microstructure, in turn, effects the dielectric properties of the film [7, 8, 9, 10, 11, 12, 13, 14]. In this chapter, the possibility of growth mode control is considered by examing the effect of using an interval deposition method [16, 32, 48] and also the effect of using an atomically thick TiO_2 buffer layer to decrease interfacial energy [9, 35].

5.1 Initial Growth Stages

The initial growth of STO on MgO substrates was studied by deposition of four monolayers, in both standard and interval deposition modes, directly

Fluence (J cm^{-2})	1.5
Temperature (°C)	850
Oxygen Partial Pressure (mbar)	0.1
Target-Substrate Distance (mm)	45
Laser Pulse Frequency (Hz)	5 (100 for interval deposition)

Table 5.1: Deposition parameters used in the study of heteroepitaxial initial growth stages.

onto annealled MgO substrates. The number of pulses for one monolayer was determined using homoepitaxial growth directly before each deposition as described in chapter 4. After each monolayer was deposited, deposition was stopped and a RHEED pattern was taken along <100> in both growth regimes. The deposition conditions that were used in this study are shown in Table 5.1. The RHEED specular intensity as a function of time along with RHEED patterns for each monolayer deposited in both standard and interval deposition modes are shown in Fig. 5.1 and Fig. 5.2, respectively. Atomic force microscopy (AFM) images of both surfaces, taken ex-situ, are shown in Fig. 5.3. During standard deposition of each monolayer (Fig. 5.1) the RHEED specular intensity decreased rapidly which indicated a three dimensional island growth. The RHEED patterns taken after each monolayer add weight to this conclusion. At first the pattern was streaky, which along with a bright specular spot and the presence of Kikuchi lines indicated a smooth surface. The pattern became more three dimensional with spots in a grid-like structure starting to appear as the growth progressed. After 4 monolayers were deposited there was no evidence of the specular reflection being present in the RHEED pattern and hence the pattern was completely three dimensional in nature. In this case the diffraction pattern is a trans-

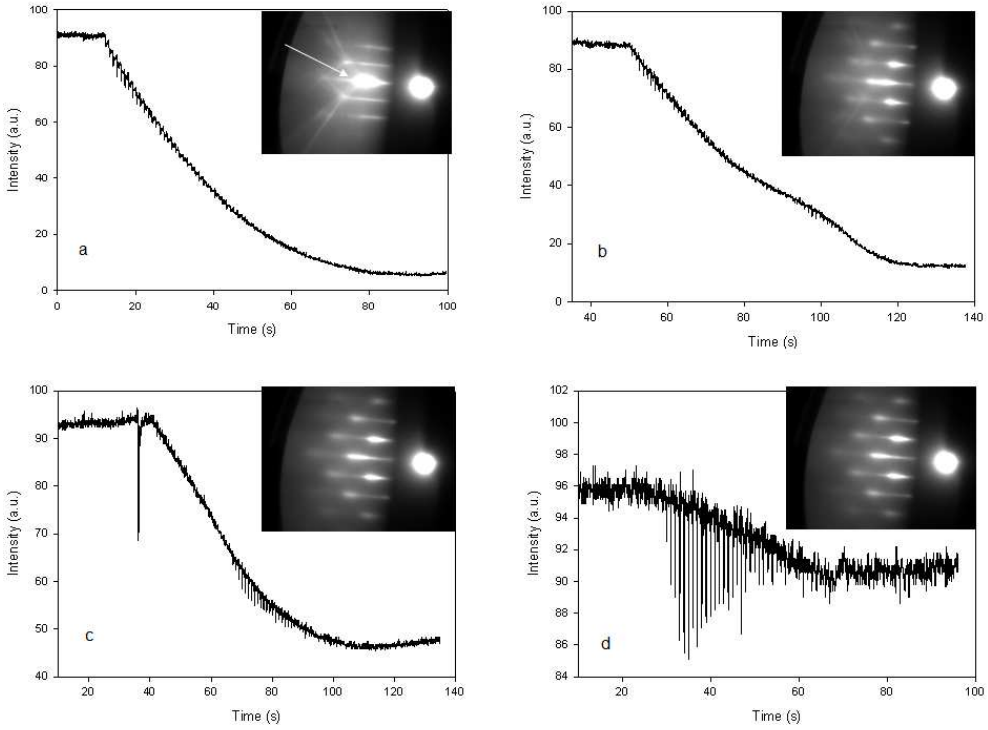

Figure 5.1: RHEED specular intensity as a function of time for the deposition of STO on a MgO substrate in standard mode and RHEED patterns taken after each monolayer was deposited. The first, (a), second, (b), third, (c), and fourth, (d), monolayers shown here. The white arrow in (a) indicates the specular reflection.

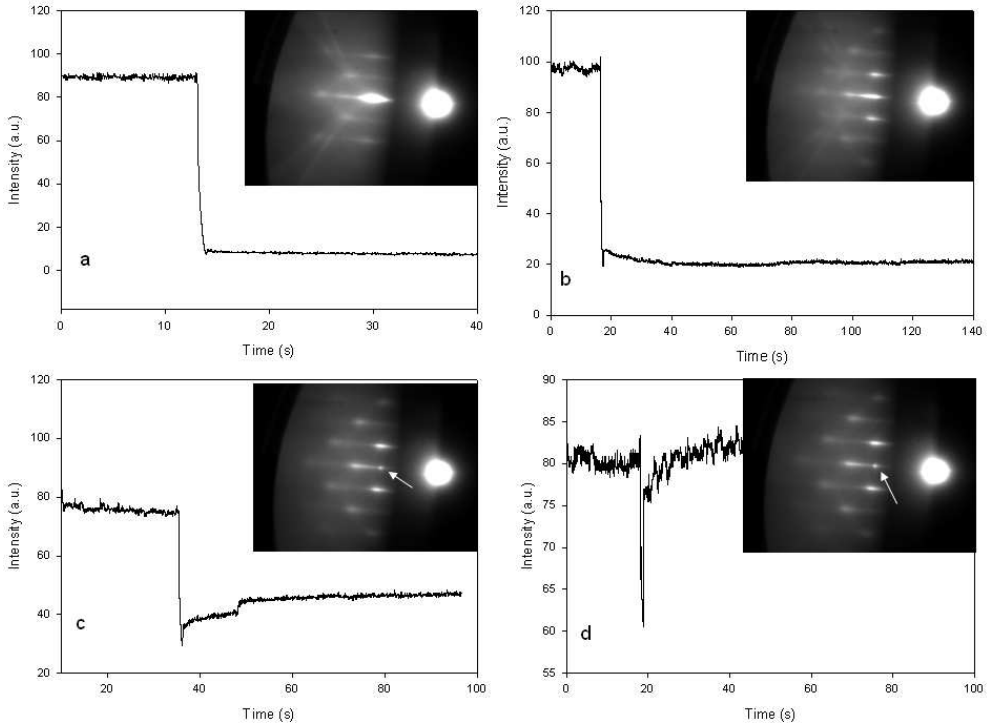

Figure 5.2: RHEED specular intensity as a function of time for the deposition of STO on a MgO substrate in interval mode and RHEED patterns taken after each monolayer was deposited. The first, (a), second, (b), third, (c), and fourth, (d), monolayers shown here. The white arrow indicates the presence of a specular reflection component.

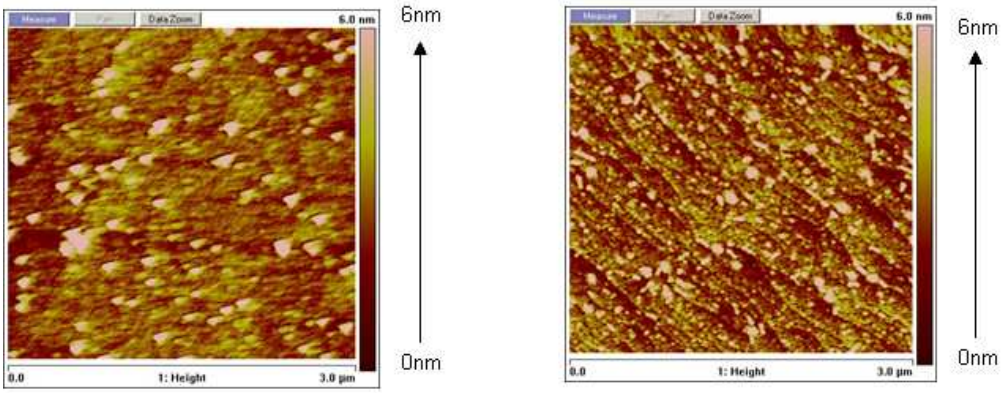

Figure 5.3: AFM images of the surfaces of 4 monolayer thick films grown by standard (*left*) and interval (*right*) deposition.

mission pattern, the electron beam passing through growth islands (see Fig. 2.4). A specular reflection is never present in a purely transmission type pattern. Modulation of the RHEED intensity by the laser pulsing was present and became more pronounced as the deposition continued. This shows the deteriorating nature of the overall specular intensity. The specular RHEED intensity for the sample grown by interval deposition showed some recovery after each interval (Fig. 5.2). This recovery is most clear in Fig. 5.2(c) and Fig.5.2(d) where the drop on commencing the burst of pulses was smaller. In addition to this, although the RHEED patterns deteriorated from a two dimensional type pattern to a three dimensional type pattern there was still a component of the specular reflection present after deposition of four monolayers. These data suggested a more two dimensional growth and a smoother surface was present when grown with interval deposition. The AFM images confirm this. The sample grown by interval deposition exhibits a smooth surface on which the steps of the substrate are still visible; this is not the case with the sample grown by standard deposition. On the surface of the PLID sample, a smooth surface was seen with three dimensional outgrowths

present on the step terraces. It was concluded that these are the result of SrO being the first layer of STO at the interface creating three dimensional nucleation sites due to the high interface energy [9, 35].

The in-plane lattice parameters of the film were calculated from the streak spacing in the RHEED patterns after each monolayer was deposited. Only the {01} streaks were present on the RHEED pattern for the STO surfaces. The distance between the (01) and $(0\overline{1})$ streaks was taken and divided by two for the streak spacing. The RHEED pattern for MgO surfaces, however, is a little more complicated. MgO has the rock-salt structure, i.e. face-centred cubic with a basis, and therefore the structure factor has to be considered. The structure factor is given by the Fourier transform of the crystal [55]:

$$F(hk) = FT(basis) \times FT(lattice). \tag{5.1}$$

There is a lattice point at (00) and one at $(0\frac{1}{2})$, so the Fourier transform of the lattice is

$$FT(lattice) = fe^{i2\pi(0)} + fe^{i2\pi(\frac{h}{2}+\frac{k}{2})}, \tag{5.2}$$

where f is the form factor of the lattice point. This analysis of the lattice structure factor shows that a reflection is only observed when h and k are both even or both odd. The Fourier transform of the basis adds extra conditions for the occurance of a diffraction point. The basis consists of a Mg^{2+} ion at (00) and an O^{2+} ion at $(0\frac{1}{2})$, so the Fourier transform is

$$FT(basis) = f_{Mg^{2+}}e^{i2\pi(0)} + f_{O^{2+}}e^{i2\pi(\frac{h}{2})}, \tag{5.3}$$

where $f_{Mg^{2+}}$ and $f_{O^{2+}}$ are the atomic form factors of the Mg^{2+} and O^{2+} ions respectively. This shows that if h is even then there is a strong reflection but if it is odd, the atomic form factors cancel and a weak reflection is observed. In the case of using RHEED to investigate MgO substrate surfaces,

the {01} reflections are therefore not allowed. Thus, the {02} streaks were used to calibrate the sample to screen distance and thus the lattice parameter measurement. The lattice parameter a is related, in the small angle approximation, to the streak spacing d by

$$a = \frac{\lambda L}{d}, \tag{5.4}$$

where L is the substrate to screen distance and λ is the electron wavelength. The misfit of the film normalised to the bulk film parameter is plotted as a function of thickness for both the PLD and PLID samples in Fig. 5.4. It can be seen that in both films the lattice parameters relax to a constant value during the deposition of the second monolayer. This agrees well with the theory described in chapter 3 that says in such a high mismatched system dislocations are introduced in the initial layers. The error bars in Fig. 5.4 are dominated by the random errors in the measurement of the streak spacing.

5.2 Control of Interfacial Layers

The study of the initial growth stages of STO films on MgO substrates added weight to the argument that the first layer of STO is important in deciding the growth mode [9, 35]. There was an improved growth mode using PLID and AFM images showed three dimensional nucleation sites on the step terraces of the film which were attributed to first layer growth of SrO. In this section it will be shown that it is possible to deposit a single atomic layer of TiO_2 onto the MgO surface. This technique will be used to examine the influence of controlling the initial layer of the STO structure on the growth mode. Films were grown with and without a TiO_2 buffer layer in both standard and interval deposition modes. These in turn were used to test the hypothesis that a layer-by-layer growth mode can be achieved

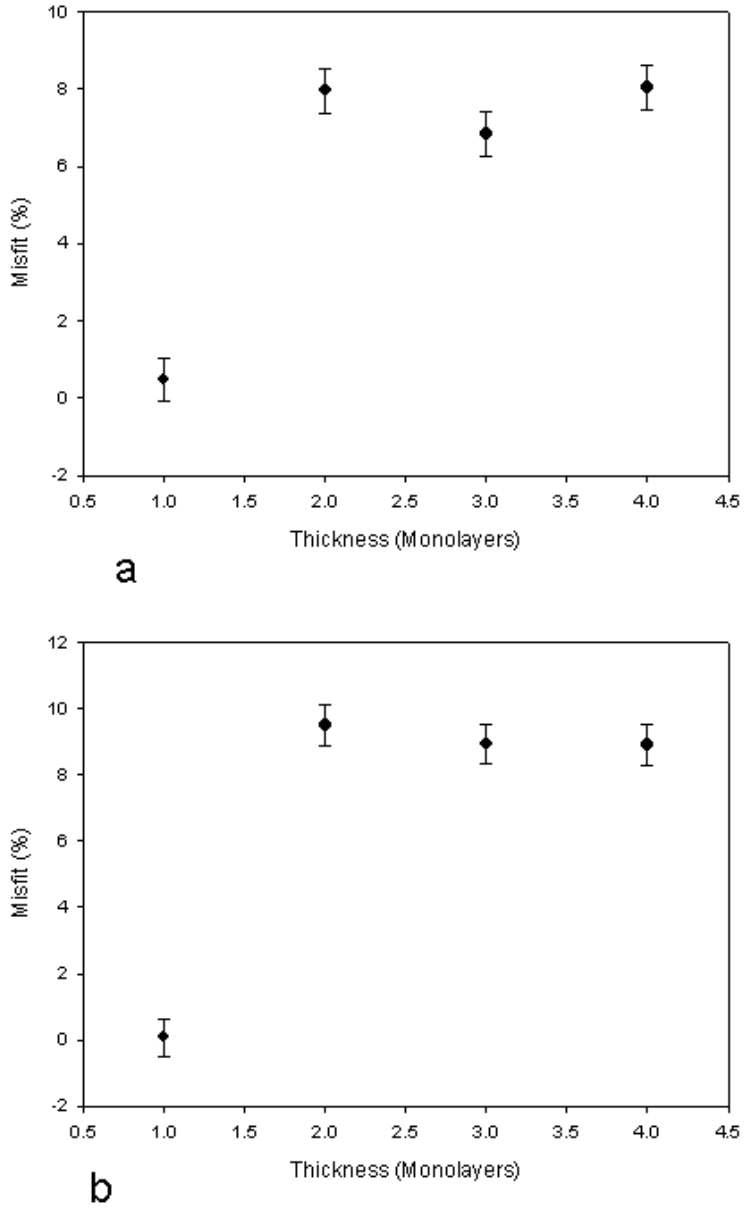

Figure 5.4: Misfit of heteroepitaxial films grown by standard (a) and interval (b) PLD as a function of thickness.

Fluence (STO) (J cm^{-2})	4
Fluence (TiO_2) (J cm^{-2})	3
Temperature (°C)	850
Oxygen Partial Pressure (STO) (mbar)	5×10^{-3}
Oxygen Partial Pressure (TiO_2) (mbar)	0.1
Target-Substrate Distance (mm)	45
Laser Pulse Frequency (Hz)	5

Table 5.2: Deposition conditions used to grow 40 nm thick heteroepitaxial films by standard deposition.

using a combination of interval deposition to overcome the large misfit and a buffer layer to improve interface compatibility.

5.2.1 Standard PLD

Films of STO were grown on MgO substrates to a thickness of 40 nm in standard deposition mode with and without a monolayer thick buffer layer of TiO_2. The deposition parameters used to grow these films are shown in Table 5.2. In Fig. 5.5 and Fig. 5.6, the RHEED intensity data for the deposition of the TiO_2 buffer layer and the RHEED pattern along <100> of the buffer layer surface are shown, respectively. It can be seen from the RHEED intensity data that a little over one monolayer was deposited as the deposition was stopped just past the peak of the oscillation. The RHEED pattern exhibits streaks, with Kikuchi lines and the specular spot indicating a smooth film and confirming it was a two dimensional growth.

The specular RHEED intensity is plotted against time for the first 500 seconds of deposition for both samples grown by standard PLD is shown in Fig. 5.7. The RHEED patterns, taken along <100>, from the surfaces

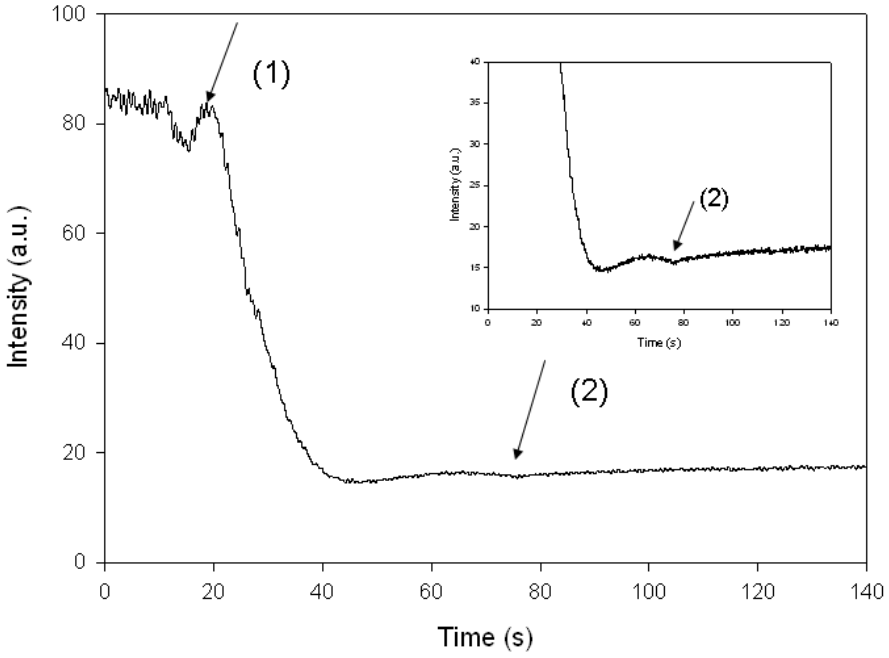

Figure 5.5: The RHEED specular intensity as a function of time during the growth of a single atomic layer of TiO_2 on an MgO substrate. The inset is a close up of the intensity oscillation and the arrows indicate the beginning, (1), and end, (2), of deposition.

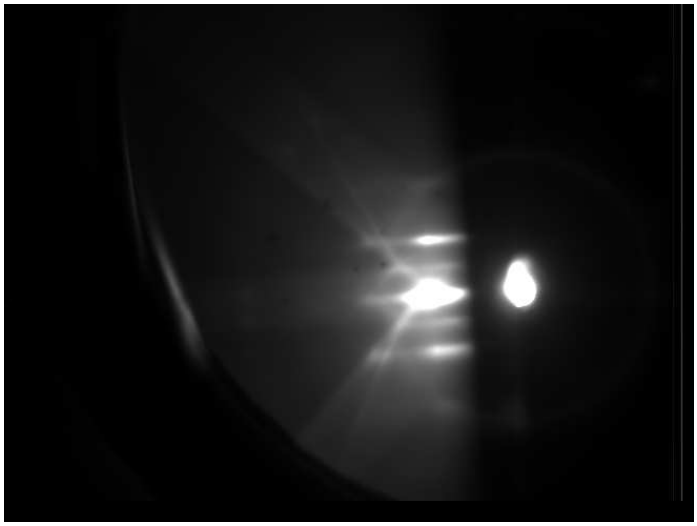

Figure 5.6: The RHEED pattern taken along <100> of the surface of an atomic layer of TiO_2 grown by standard deposition onto MgO.

of the two films after deposition are shown in Fig. 5.8. Both film surfaces exhibited a similar streaky pattern and hence, showed a smooth surface with some disorder. The specular RHEED intensity, in both cases, droped rapidly to a steady state which is characteristic of a three dimensional island growth mode. However, there was an increase in intensity at the beginning of growth when there was a buffer layer present which resembled an intensity oscillation as observed with a layer-by-layer growth mode. This, however, was not an oscillation; the observation that as the STO growth started the specular reflection moved position lead to the conclusion that the increase in specular intensity was actually due to the STO specular reflection growing in intensity whilst the MgO/TiO_2 specular reflection died out. Although both films had a three dimensional growth mode, the fact that the STO specular reflection was obeserved at the beginning of growth suggests that the film was smoother in the initial stages of growth when a TiO_2 buffer layer was deposited first. The growth was improved by the introduction of the buffer

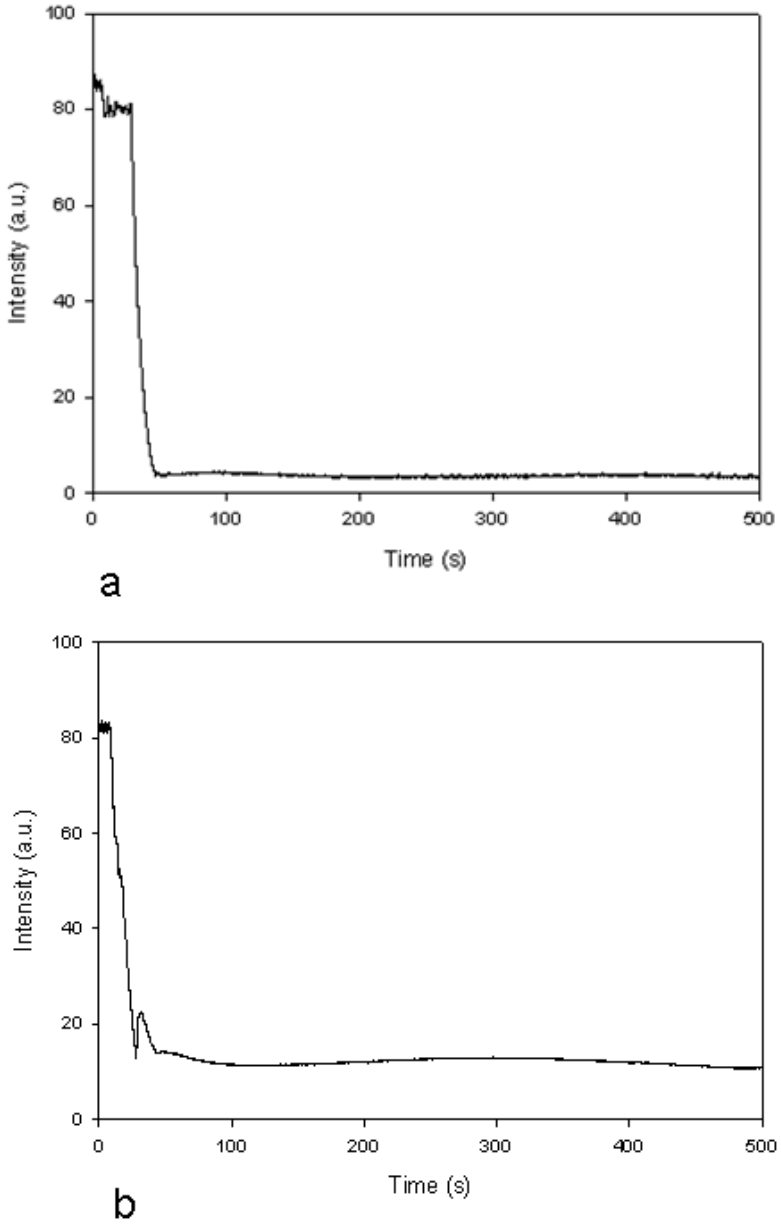

Figure 5.7: The RHEED specular intensity as a function of time for the first 500 seconds of growth of heteroepitaxial STO on MgO by standard PLD both without (a) and with (b) an atomic buffer layer of TiO_2.

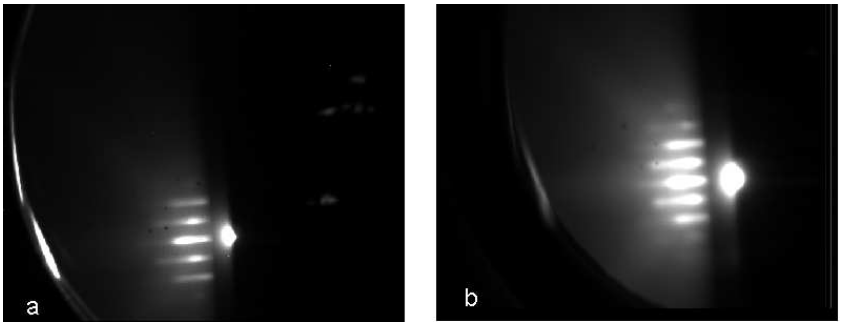

Figure 5.8: RHEED patterns taken along <100> of 40 nm thick STO films grown by standard deposition without (a) and with (b) a TiO_2 buffer layer.

layer. Forcing the first layer of the STO structure to be TiO_2 allows the intial layers to completely wet the surface.

TEM analysis was completed by Dr. Y. Y. Tse [36]. Bright field cross-sectional TEM images with g=200 and g=002 for the film grown by standard deposition without a buffer layer of TiO_2 are shown in Fig. 5.9(a) and Fig. 5.9(b) respectively. A smooth film is observed with misfit dislocations at the interface and some threading dislocations throughout the film. The selected area electron diffraction (SAED) pattern reveals that the film is cubic and the completely relaxed. The misfit between film and substrate was calculated from the SAED to be 7.8 %, which is consistant with the 7.9 % estimated from the bulk parameters. The dark field TEM image showing the misfit dislocations at the interface is shown in Fig. 5.10. From the dark field image the misfit dislocation spacing was calculated to be approximately 2.80 ± 0.25 nm. The expected separation of pure edge dislocations of [100] or [010] type which would fully relieve the mismatch strain is 5.3 nm. Therefore, there was a higher density of misfit dislocations than required of pure edge type to completely relieve strain. The misfit dislocation must therefore be of a type that is less effective at relieving strain than pure edge type. Analysis of

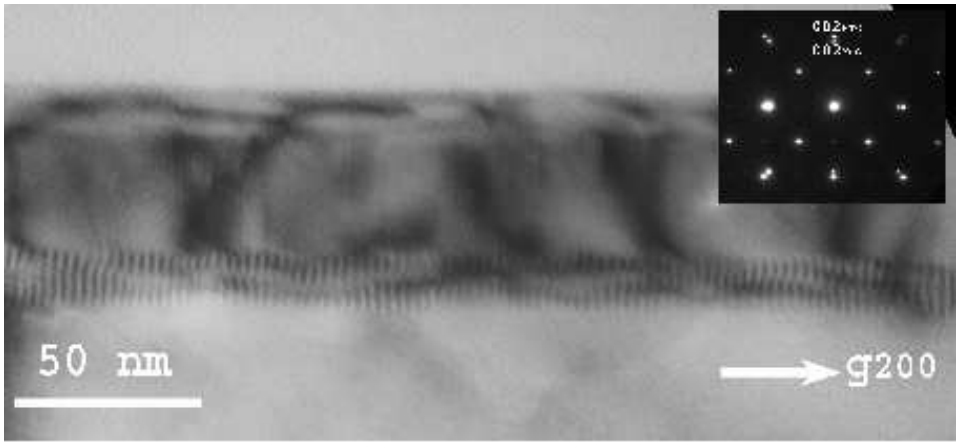

a

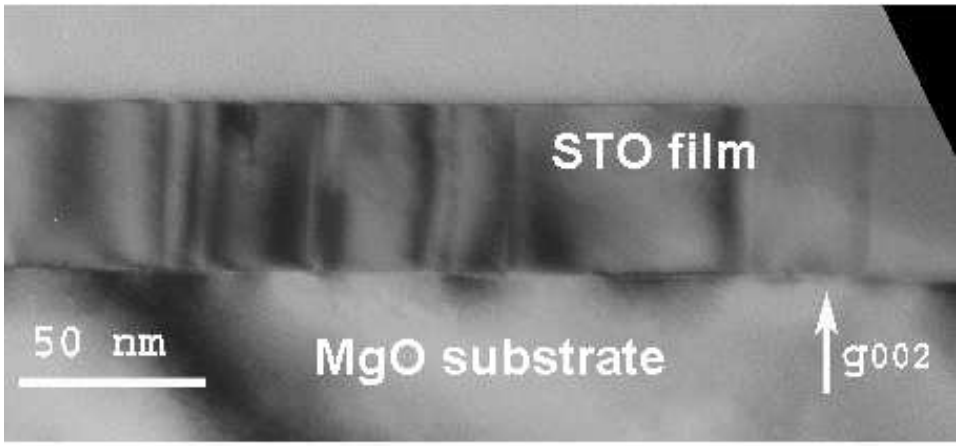

b

Figure 5.9: Bright field cross-sectional TEM images of a heteroepitaxial film grown by standard deposition with no TiO_2 buffer layer. The sample was tilted to the two beam condition with g=200, (a), and g=002, (b). The inset shows the selected area electron diffraction (SAED) pattern.

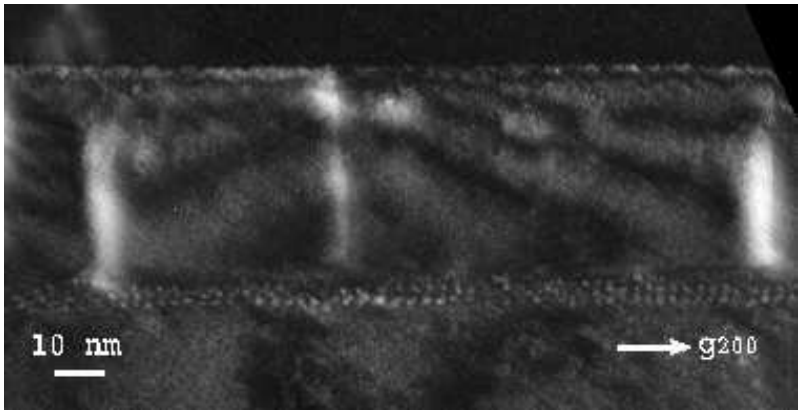

Figure 5.10: Dark field cross-sectional TEM image of a heteroepitaxial film grown by standard deposition with no TiO_2 buffer layer. Misfit dislocations at the film/substrate interface and threading dislocations (vertical white lines) are evidenced.

TEM images found the misfit dislocations to have a Burgers vector of $\mathbf{b} = \frac{1}{2}[\bar{1}01]_{STO}$. This was confirmed by drawing a Burgers circuit around a misfit dislocation on a Fast Fourier Transform filtered image of Fig. 5.10. This type of dislocation requires a separation of approximately 2 nm for complete relaxation of the misfit strain [36]. The presence of larger separation indicates that the misfit dislocations do not completely relax the strain. It can, thus, be deduced that the threading dislocations have some role in strain relaxation too.

Bright field cross-sectional TEM images, with g=002 and g=200, of the film grown by standard deposition with a buffer layer of TiO_2 are shown in Fig. 5.11. The film is smooth but has cracks as seen in Fig. 5.11(b). The dark field images are shown in Fig. 5.12.

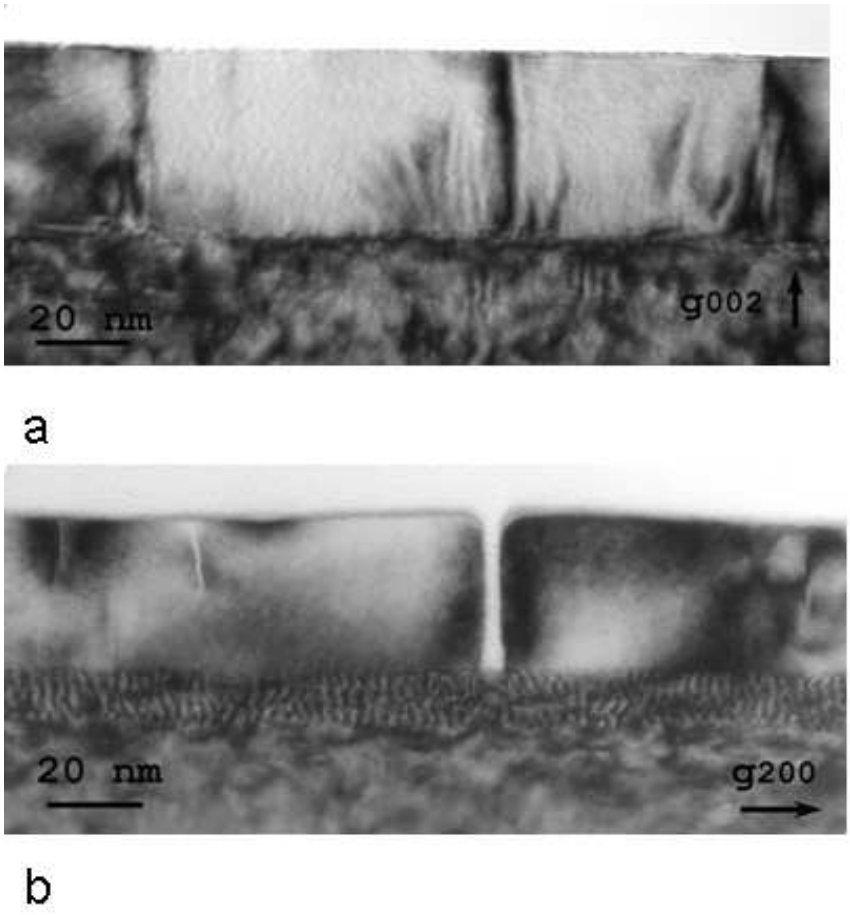

Figure 5.11: Bright field cross-sectional TEM images of a heteroepitaxial film grown by standard deposition with a TiO_2 buffer layer. The sample was tilted so that g=002, (a), and g=200, (b).

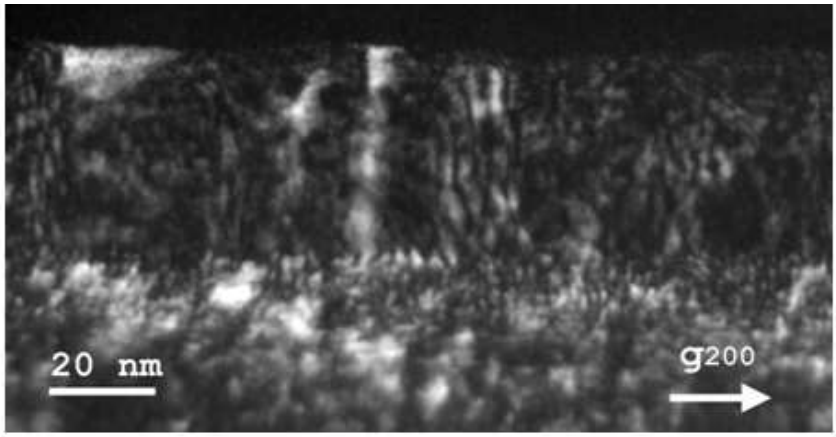

a

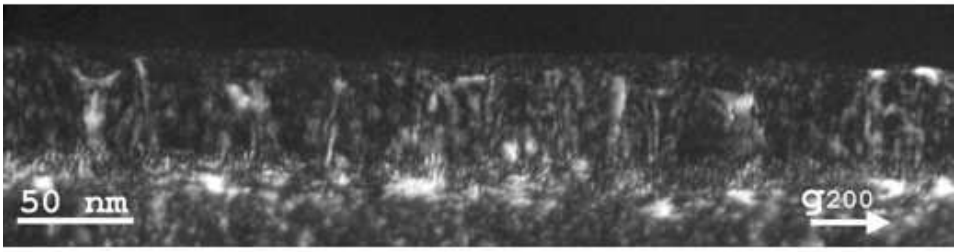

b

Figure 5.12: Dark field cross-sectional TEM images of a heteroepitaxial film grown by standard deposition with a TiO_2 buffer layer. Here, the sample was tilted so that g=200 in both (a) and (b).

The misfit dislocation separation was calculated to be 2.74 ± 0.25 nm which is the same as the sample without a buffer layer. The film was seen to have an out-of-plane misfit of 7.0 % and an in-plane misfit of 6.4 % from the SAED pattern. The high-resolution TEM was not possible due to the quality of the foil prepared, therefore Burger's vector analysis was not possible.

Fluence (STO) (J cm^{-2})	4
Fluence (TiO_2) (J cm^{-2})	3
Temperature (°C)	850
Oxygen Partial Pressure (STO) (mbar)	5×10^{-3}
Oxygen Partial Pressure (TiO_2) (mbar)	0.1
Target-Substrate Distance (mm)	45
Laser Pulse Frequency (Hz)	60

Table 5.3: Deposition conditions used to grow 40 nm thick heteroepitaxial films by interval deposition.

5.2.2 Interval Deposition

Films of STO were grown with a thickness of 40 nm on MgO substrates in interval deposition mode; one with and one without an atomically thick buffer layer of TiO_2. RHEED patterns were taken along <100> and the RHEED current was increased to bring the specular intensity higher after every 10 monolayers grown for the first 40 monolayers and then every 20 monolayers grown subsequently. The deposition parameters used to grow these films are shown in Table 5.3. The buffer layer was grown under the same conditions as the standard deposition films, in standard deposition mode at a laser pulse frequency of 5 Hz. The specular RHEED intensity data is shown, from throughout the deposition for the samples without and with a TiO_2 buffer layer in Fig. 5.13 and Fig. 5.14, respectively. The insets to the intensity data show the RHEED patterns taken along <100> of the surface at the corresponding stages of the growth.

Interval deposition directly onto the substrate, without a buffer layer of TiO_2, shows some improvement over the films grown in standard deposition mode. The first interval decreased the specular intensity dramatically and

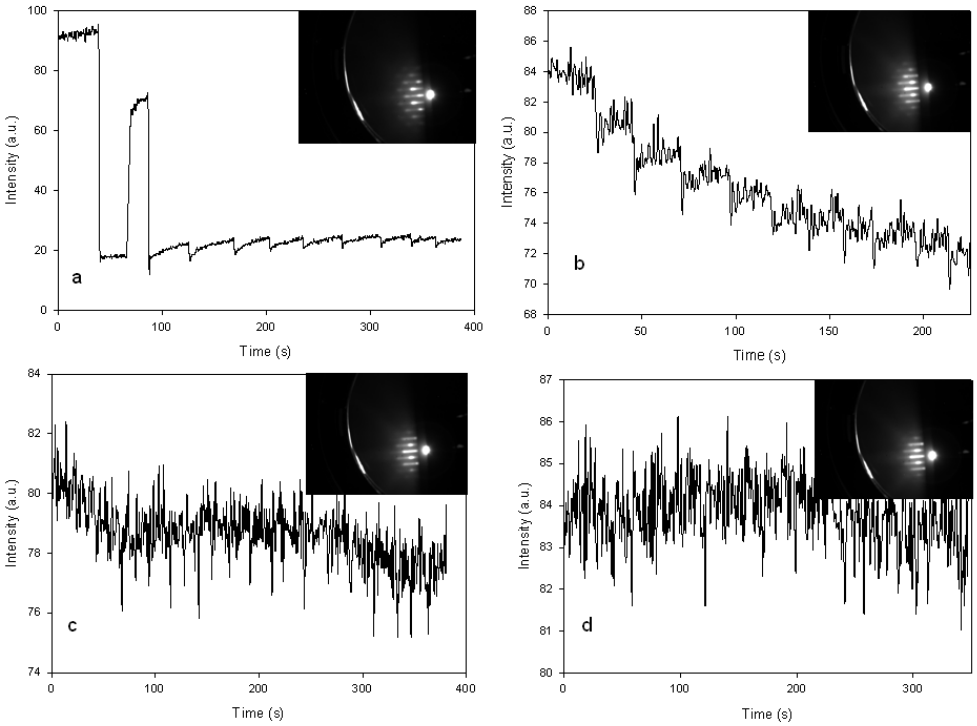

Figure 5.13: Specular RHEED intensity data throughout the growth of a heteroepitaxial film grown by interval deposition with no buffer layer of TiO_2. Shown here is the 1^{st}10, (a), the 20^{th} to the 30^{th}, (b), the 40^{th} to 60^{th}, (c), and the $80^{th}$to 100^{th} monolayers grown. The insets show the RHEED patterns of the surface along <100> taken after the corresponding round of deposition.

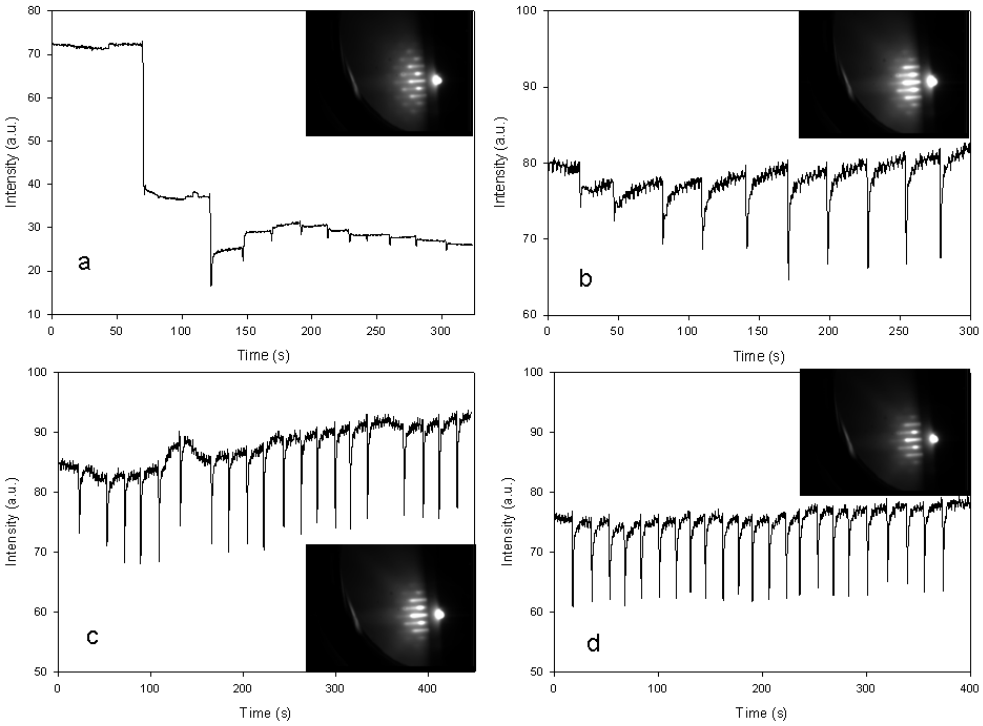

Figure 5.14: Specular RHEED intensity data throughout the growth of a heteroepitaxial film grown by interval deposition with a buffer layer of TiO_2. Shown here is the $1^{st}10$, (a), the 20^{th} to the 30^{th}, (b), the 40^{th} to 60^{th}, (c), and the $80^{th}$to 103^{rd} monolayers grown. The insets show the RHEED patterns of the surface along <100> taken after the corresponding round of deposition.

showed negligible recovery; the RHEED current was increased to artificially increase the specular intensity before the second monolayer was deposited. The second interval deposited also decreased the specular intensity dramatically but exhibited a greater recovery. After the deposition of the first two monolayers, each subsequent interval deposited saw a small drop in specular intensity followed by a recovery to a very similar intensity as before. This hinted at a two dimensional component to the growth mode. The RHEED pattern taken after ten monolayers were deposited was streaky which is indicative of a smooth surface. By the twentieth interval deposited the specular intensity showed a decrease after each monolayer was deposited. The decrease in the signal to noise ratio indicated the growth was deteriorating to a three dimensional island growth. The RHEED pattern taken after 30 monolayers were deposited showed a streaky pattern with hints of three dimensional transmission spots being superimposed over the streaks. Shortly after this the specular intensity became very noisy and decreased steadily with time. There was no evidence of the sudden drops in intensity followed by an exponential recovery that are characteristic of the interval deposition technique. Although there was no visible change in the RHEED pattern from the surface, the fact that the specular intensity has reached a steady decline shows that the transmission components of the RHEED pattern had become dominant. The intensity was, therefore, insensitive to surface phenomenon. It was at this cross-over point that the two dimensional growth was completely replaced by a three dimensional island growth.

A buffer layer of TiO_2 in combination with interval deposition improved the growth further. Fig. 5.14 shows that two dimensional growth was continued throughout the entire deposition. Each interval exhibited a definite drop in specular intensity followed by a sharp recovery back to a level simi-

lar to that before the interval was deposited. In fact towards the end of the 40 nm the intensity regularly increased with each interval deposited. The only exceptions to this were the first two intervals deposited which showed a significant drop in intensity with not much recovery. This happened with greater effect in the deposition of the sample without a buffer layer. The fact that this effect is still quite prominant in a film which clearly has a forced two dimensional growth mode leads to the deduction that at least part of this initial decrease in specular reflection may be due to change in surface material effecting the reflected intensity.

The relaxation of the specular RHEED intensity as a function of time following the deposition bursts was studied for the samples grown by interval deposition. If there a single relaxation time then the intensity varies after a deposition burst with time as

$$I = I_0 \left(1 - \exp - \frac{t}{\tau}\right), \tag{5.5}$$

where I_0 is the maximum intensity after the deposition burst, t is the time after the deposition burst, and τ is the relaxation time. Rearranging equation (5.5) and taking the natural log of the normalised intensity gives a straight line when plotted against time, the gradient of which is $-\frac{t}{\tau}$. The intensity data for both the sample with and the sample without a buffer layer of TiO_2 was fitted and analysed. The intensity data for the initial growth of the sample without a buffer layer yielded a plot which was not a straight line, seen in Fig. 5.15(a), which indicated more than one relaxation time connected to the growth. This confirmed that there were both three dimensional and two dimensional growth processes occuring. As the growth diminished further into a three dimensional island growth the data became too noisy to identify any trend (Fig. 5.15(b)). The data for the sample with a buffer layer of TiO_2 did exhibit a straight line trend, seen in Fig. 5.15(c), and the relax-

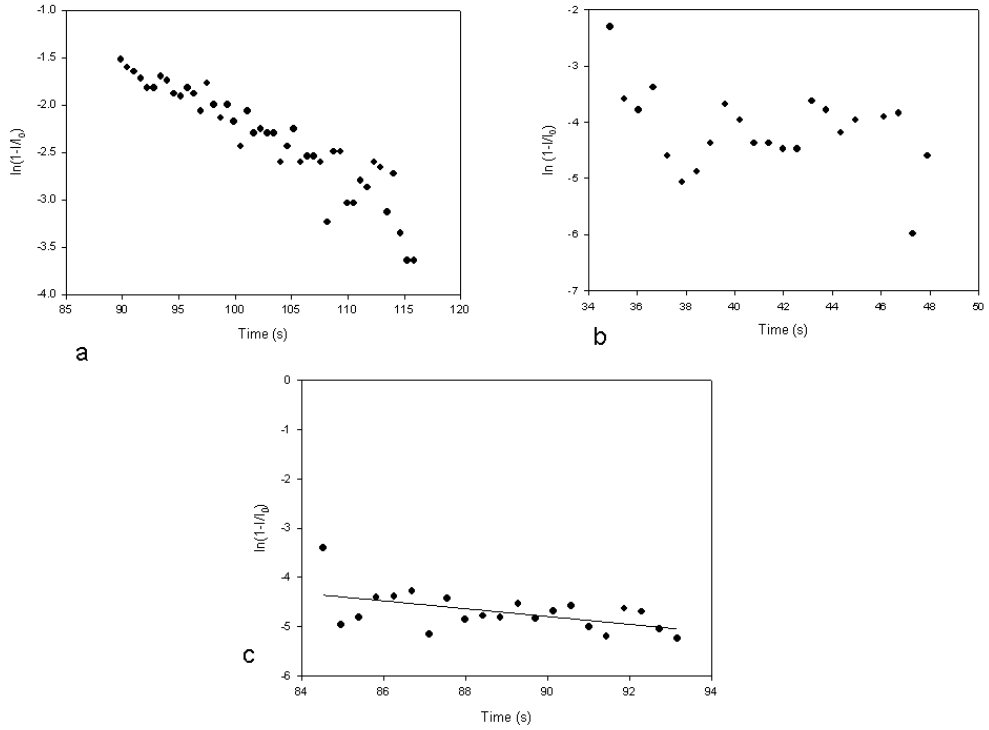

Figure 5.15: Natural log plots of the normalised specular intensity data against time for the heteroepitaxial samples grown by interval deposition without, (a) and (b), and with, (c), a buffer layer of TiO_2

ation time was calculated to be constant throughout the growth with a value of 10.49 ± 1.14 s. The fact that it was possible to calculate τ showed that there was only one growth process present, confirming a two dimensional mode. The continuity throughout the growth fits with the theory described in chapter 2 which suggested that any change in the relaxation time is coverage dependent. As there was no coverage variation seen here, the relaxation time should be constant.

A study of the in-plane lattice misfit as a function of thickness was only possible for the interval deposition as taking a RHEED pattern requires stopping the deposition and rotating the sample azimuthally so that the

electron beam is incident along a direction of high symmetry. The misfit is plotted against thickness for the both interval samples in Fig. 5.16. The strain had relaxed in both films to a steady state by the tenth monolayer deposited. This is in good agreement with the intial growth studies that showed that the strain relaxes during the growth of the initial layers. The first point, at one monolayer, on the plot for the sample with a buffer layer corresponds to the RHEED pattern taken after deposition of the TiO_2. It was noted that the atomically thick TiO_2 buffer layer stretches to the MgO lattice parameter and this agrees with the conclusion that the single TiO_2 layer grows in a layer-by-layer mode.

TEM [36] was undertaken and, shown in Fig. 5.17, is the bright field images of the film grown by PLID without a buffer layer. The film is smooth for the most part but exhibits a number of undulations throughout the film. These undulations confirmed the film had a three dimensional component to its growth. They are most likely caused by the progression of growth from the three dimensional nucleation sites seen in the AFM of Fig. 5.3 in the intial growth studies. The SAED patterns reveal that the film was under in-plane tension and out-of-plane compression with a misfit of 6.8% in-plane and 9.4% out-of-plane. However, the dark field TEM image, shown in Fig. 5.18, displayed the same spacing of misfit dislocations as the film grown with standard PLD and no buffer layer, which was completely relaxed in-plane and out-of-plane. The fact that the PLID film had fewer threading dislocations and is strained confirms the role that threading dislocations play in relieving strain. Interval deposition, whilst forcing a growth mode that is unfavourable under normal growth conditions, seems to inhibit the formation of threading dislocations and thus forces strain into the structure.

Cross-sectional bright field images are shown in Fig. 5.19 for the het-

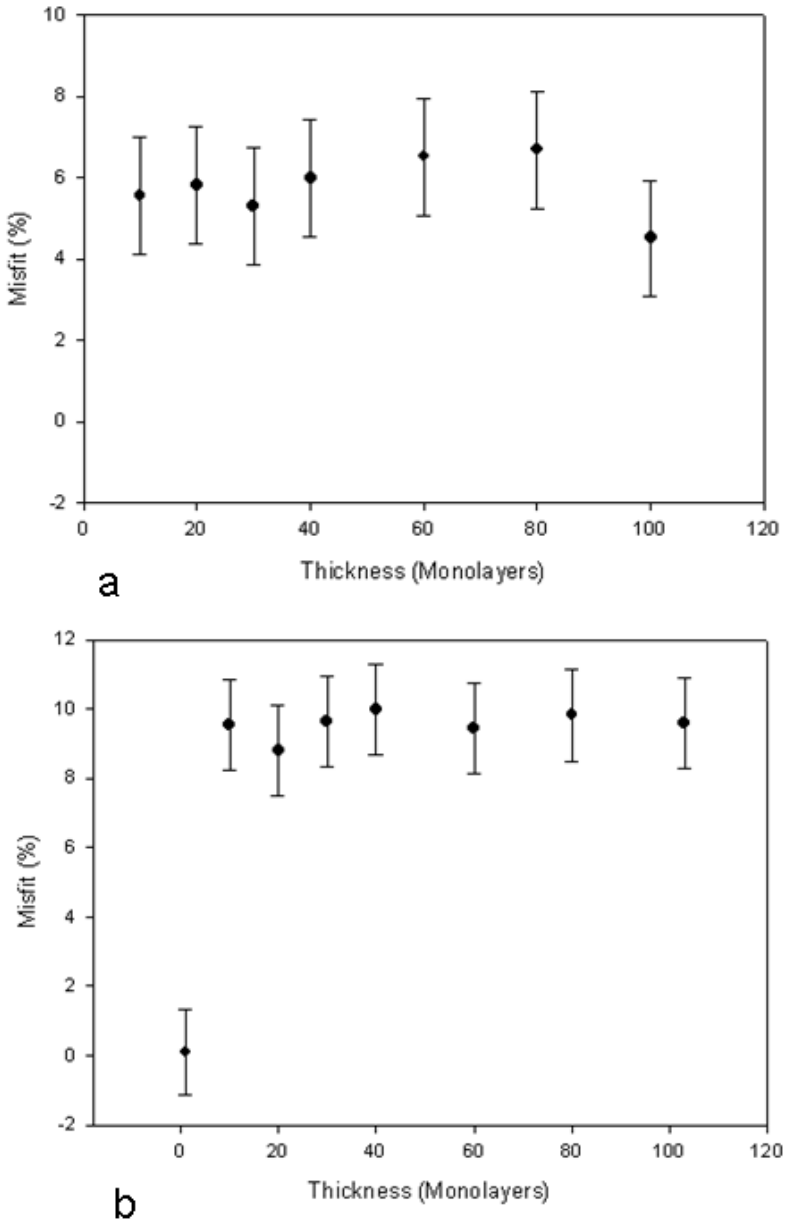

Figure 5.16: The misfit plotted as a function of thickness for films grown by interval deposition without, (a), and with, (b), a TiO_2 buffer layer.

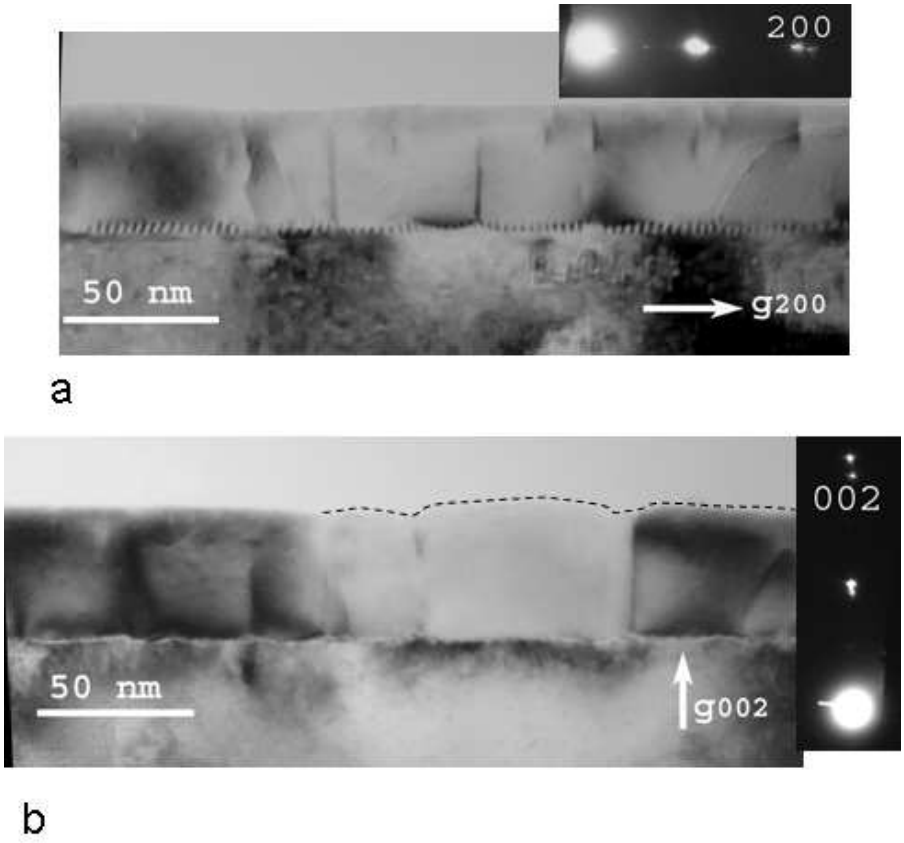

Figure 5.17: Cross-sectional bright field TEM images of the heteroepitaxial PLID film without a buffer layer. The sample has been tilted so that g=200, (a), and g=002, (b). Insets show the SAED patterns.

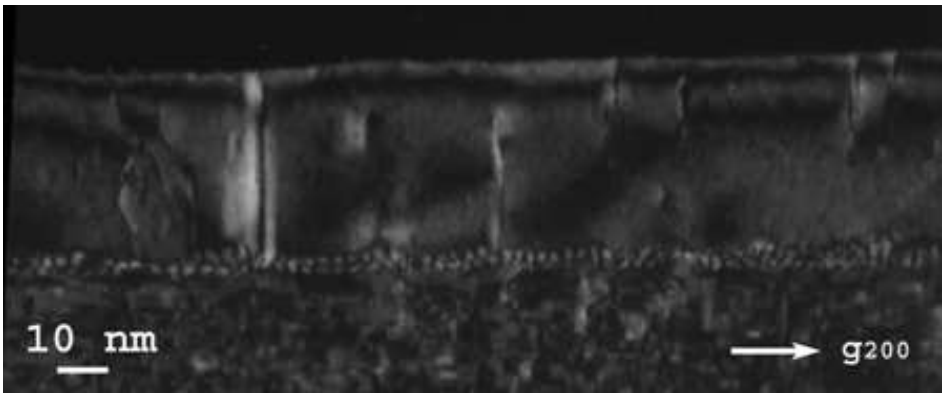

Figure 5.18: Cross-sectional dark field TEM image of the heteroepitaxial PLID film without a buffer layer.

eroepitaxial film grown by PLID with a TiO_2 buffer layer. The film appears to have cracks just as the standard deposition film with a buffer layer. These are most noticable in Fig. 5.19(a). The film appeared to be strained with an in-plane misfit of 5.8 % and an out-of-plane misfit of 8.2 %, as calculated from the SAED pattern; this is consistent with Poission's ratio. The dark field image for the same film is shown in Fig. 5.20. The misfit dislocation separation was calculated to be 3.1 ± 0.25 nm which is higher than all the other films. This coupled with the strain within the film confirms that interval deposition inhibits defect formation and forces strain into the film structure. The fact that a two dimensional growth was obeserved in the RHEED indicated that the cracks visible in the TEM images formed after growth, most likely during cooling. It is thought that the combination of the TiO_2 buffer layer allowing the film to completely wet the substrate and the interval deposition inhibiting defect formation creates such a strained structure that it is unstable. The rapid cooling process from the deposition temperature to room temperature most likely causes local temperature gradients which in turn nucleate crack formation. It should be noted, however,

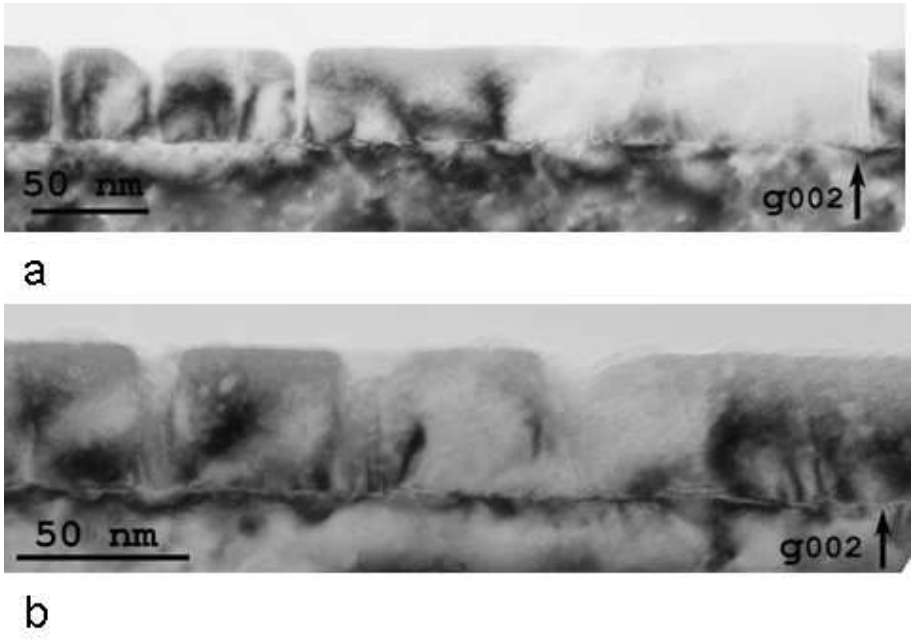

Figure 5.19: Cross-sectional bright field TEM images of the heteroepitaxial PLID film with a TiO_2 buffer layer.

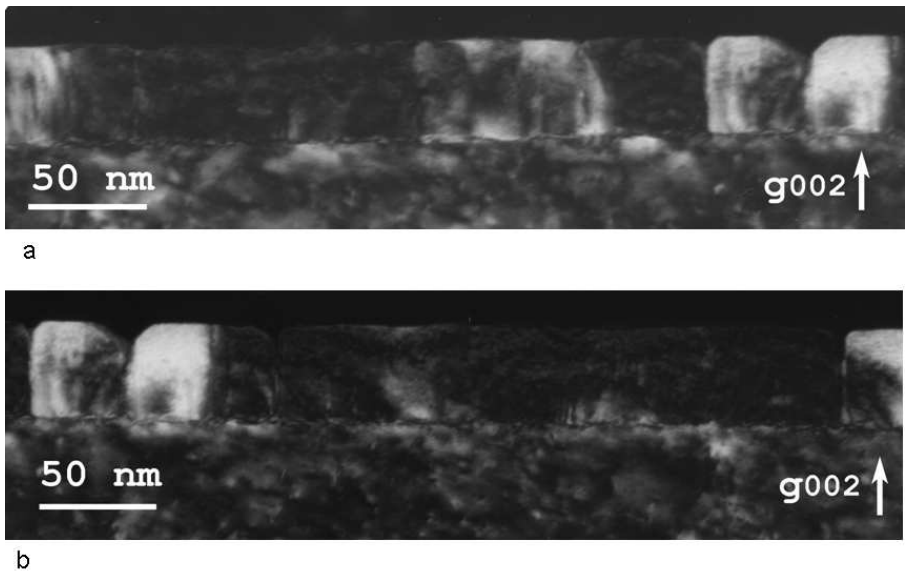

Figure 5.20: Cross-sectional dark field TEM images of the heteroepitaxial PLID film with a TiO_2 buffer layer.

that the films considered here are much thinner than the calculated critical thickness for crack formation in chapter 3. This calculation is considering the case of cracking relieving strain during growth and does not account for imperfections in the film and the dynamic nature of the cooling process. The cracks formed here were not efficient at relieving strain and thus can be seen as a by-product of the cooling process upsetting the balance introduced by the interval deposition.

5.3 Summary

In the initial stages of growth interval deposition was found to improve growth of STO on MgO with the step and terrace structure still being present after 4 monolayers deposited (Fig. 5.3). The step and terrace structure was not apparent in the 4 monolayer thick film grown by standard deposition. Even though the step and terrace structure was still visible there was still three dimensional outgrowths across the surface and these were attributed to SrO at the interface. It was seen that the strain was relieved within the growth of the intial layers as seen in Fig. 5.4. This agrees well with the theory presented in chapter 3.

In the later stages of growth it was noted that interval deposition alone introduced a two dimensional component to the growth of STO on MgO, however, this completely broke down to a three dimensional growth after the deposition of 30 or so monolayers. With the addition of an atomically thin buffer layer of TiO_2 the STO was able to wet the surface completely and interval deposition forced a two dimensional growth mode throughout the deposition of the 40 nm thick film with no sign of deterioration to a three dimensional growth. It was seen that interval deposition inhibits the formation of dislocations and forces strain into the film structure. There

were cracks seen in the TEM images of the thin films with a buffer layer of TiO_2 and this was attributed to strain causing an unstable structure which breaks down during the cooling from the growth temperature.

Chapter 6

CONCLUSIONS AND FURTHER WORK

Homoepitaxy was used to optimise the PLD setup to achieve a layer-by-layer growth. The RHEED was used to observe the growth mode of STO. It was seen that the old experimental setup, used by many groups worldwide [15, 49, 50, 51], with the "large laser spot size" of 2×4 mm^2 on the target provides too high a deposition rate even at low fluence for high quality film growth. A three dimensional island growth was observed as there was not enough time between laser pulses for the high density of adatoms to crystallise into a single layer with a "clean" microstructure. Lowering the instantaneous deposition rate by decreasing the spot size brought a layer-by-layer growth mode into favour. This had been seen in the literature [16, 32, 48, 52, 53], however, most groups used a low oxygen pressure. Good oxygenation is required of the films grown in this thesis because ultimately, the films are to be used in microwave devices and oxygen vacancies are known to have an adverse effect on the dielectric properties, particularly on the loss tangent [14]. With a small spot size and high oxygen pressure the ablation plume was too small; increasing the fluence overcame this problem. The combination of small spot size and high fluence produced a deposition rate of ~ 50 pulses per monolayer. A substrate temperature of 850 °C caused a high surface mobility that favoured the desired two dimensional growth mode. It was observed

with RHEED that a layer-by-layer growth mode was easily achieved in both standard and interval deposition modes when the deposition parameters are carefully chosen. The specular RHEED intensity exhibited oscillations as a function of time in standard mode (Fig. 4.5). In interval mode [16, 32, 48], however, only the first five monolayers deposited showed the characteristic drop in specular intensity followed by a recovery as the adatoms find stable sites. The RHEED patterns for both standard and interval deposition of homoepitaxial STO, shown in Fig. 4.6 and Fig. 4.8 respectively, exhibit spots lying on Laue circles as well as Kikuchi lines. These are indicative of a smooth, well ordered, highly crystalline surface and confirm that a two dimensional growth mode was present in both films. TEM analysis confirmed the high crystallinity of the films and showed that the substrate/film interface was consumate. There were no threading or misfit dislocations observed.

The initial growth studies of heteroepitaxial STO on MgO substrates provided the first evidence that the interval deposition technique could force a two dimensional layer-by-layer growth mode in such a highly mismatched system. After deposition of four monolayers of STO onto MgO substrates in the interval deposition regime, the step and terrace structure of the substrate was still visible in the AFM image of the film (Fig. 5.3). In standard mode this was not observed. The growth in interval mode, however, was not of a purely two dimensional type. Three dimensional outgrowths were visible in the AFM across the whole surface. It was concluded that these outgrowths were due to SrO at the film/substrate interface. When the film nucleates on the substrate surface, the intial layer is equally likely to be SrO or TiO_2. The high interface energy caused by the anion-anion or cation-cation nearest neighbour interactions when SrO is the first layer of STO at the interface prevents the film from wetting the surface [9, 35]. This

generates a three dimensional outgrowth of SrO which acts as a nucleation site for three dimensional growth of the film. The fact that TiO_2 wets the surface and SrO does not explains why, in interval deposition, the film was smooth between the outgrowths; the majority of the film started with the TiO_2 layer and the interval deposition forced a two dimension growth in those areas.

The comparison of standard growth of STO on MgO with and without a buffer layer of TiO_2 confirmed that the film completely wetted the surface when the intial layer of STO was controlled to be TiO_2. The standard growth of STO directly onto the MgO surface exhibited a sharp initial drop in specular RHEED intensity without recovery (Fig. 5.7). With an atomic layer of TiO_2 the specular intensity exhibited a peak at the beginning of the growth which coincided with a shift in position of the specular reflection. Although it was concluded that this peak was not a RHEED intensity oscillation indicating two dimensional growth, it did show how the specular reflection due to the MgO/TiO_2 surface faded out and the STO specular reflection became dominant as the surface material changed. This showed how the surface was much smoother in the initial stages of growth when a TiO_2 buffer layer was present, and thus confirmed that controlling the initial layer of the STO structure allowed the film to wet the surface completely.

It was seen that interval deposition introduced a two dimensional component into the growth, even without a buffer layer of TiO_2 (Fig. 5.13). However, after 30 or so monolayers were deposited the three dimensional growth caused by SrO at the interface began to dominate and the two dimensional component to the growth was abolished. By controlling the interfacial layer of STO, layer-by-layer growth was continued throughout the growth of the 40 nm film (Fig. 5.14). The monatomically thick TiO_2 buffer layer was in-

tegrated into the STO structure as the initial interfacial layer which allowed the film to wet the substrate completely. The kinetics of interval deposition [16, 32, 48] forced a two dimensional growth mode in a system where it would not be favourable under standard deposition conditions due to the high mismatch between film and susbstrate. Each monolayer was deposited at high laser pulse frequency in under the relaxation time and the laser was turned off to allow time for crystallisation. In that way it can be assumed that after each deposition burst there was a highly dense gas of adatoms on the surface and nucleation occured only after the burst was over. The high supersaturation on the surface favoured a high nucleation density with a very small average island size. This small island size dramatically lowered the probability of second layer nucleation and thus forced a two dimensional growth mode. The specular intensity relaxation times confirm that when the intial layer of STO was controlled to be TiO_2 there was only one growth process present. Two growth processes were present without a buffer layer showing that both three dimensional and two dimensional growth were occuring. By forcing the film to grow in a layer-by-layer fashion, the formation of dislocations, which are introduced in the initial layers of growth (Fig. 5.4), was inhibited and strain was incorporated into the film structure. It was evident, when examining the TEM data, that this strained structure was unstable and caused cracking of the film during the cooling process. During cooling from the deposition temperature the delicate balance of the strained structure was disturbed and initiated the cracking process.

Further Work

The question of whether it is impossible to impose a two dimensional layer-by-layer growth mode on such a badly matched system of STO film on MgO

substrate has been answered. It is indeed possible, however, the technique developed here will only truely be useful if the improved crystallographic structure alters the dielectric properties positively. Therefore, heteroepitaxial films must be grown with and without a TiO_2 buffer layer in both interval and standard deposition regimes for dielectric measurement and comparison. A layer of superconducting $YBa_2Cu_3O_7$ will be grown on top of these and patterned using photolithography for dielectric measurements at microwave frequencies. The dielectric properties will be correlated to the growth modes and dislocation densities and the hypothesis that a more perfect crystal structure will lead to higher tunability and lower loss will be tested.

In addition to this, a number of interesting experiments are still left to do on the growth. First and foremost, the elimination of the cracking process during cooling is desirable. Various cooling regimes with different ramp rates will be tested in an attempt to lock the strain into the structure and prevent cracking. X-ray analysis (e.g. reciprocal space mapping) will allow accurate measurement of in-plane and out-of-plane lattice parameters leading to an evaluation of strain gradients) [38, 39, 56]. Further TEM studies could reveal the nature of the cracking, also. Plan view TEM would give data on any misallignment or twisting of the crystal structure on two sides of a crack. A repeat of the heteroepitaxial initial growth studies would provide additional information on the early growth stages. Hopefully this would shed some light on the reason for the dramatic drop in specular RHEED intensity for the first few monolayers grown. It would, also, be interesting to take RHEED patterns throughout the growth and study the evolution of the full width half maxima of the RHEED streaks. This was not possible in the present study as the pattern intensity was maximised to observe all details of the pattern. This, unfortunately, caused the maxima to saturate the RHEED

camera and made viewing the maxima impossible.

If it is impossible to eliminate the cracking and/or the films do not provide the ideal microwave properties expected, the techniques developed and knowledge gained here are easily adaptable to growth on other substrates that also have favourable properties for microwave engineering. Other substrates may give an even more greatly optimised architechture for microwave devices. It seems likely that through careful choice of substrates and growth regimes, the defect content of the films can be controlled. This would allow clear identification of particular defects with particular dielectric response.

Another application of RHEED in combination with PLD that has the potential to be very useful is the production of high quality superlattices or multilayers [57, 58, 59]. This technique could allow for strain and defect engineering to control material properties. Also, the production of novel devices, such as all-oxide diodes, is a possibility eliminating cross-layer oxidation or contamination.

REFERENCES

[1] C. Kittel. *Introduction to Solid State Physics.* John Wiley & Sons, Inc., 7th edition, 1996.

[2] F. Jona and G. Shirane. *Ferroelectric Crystals.* Dover Publications, Inc., 1993.

[3] J. R. Hook and H. E. Hall. *Solid State Physics.* John Wiley & Sons, Inc, 2nd edition, 2001.

[4] P. M. Suherman. Private communication. 2006.

[5] A. K. Tagantsev, V. O. Sherman, K. F. Astafiev, J. Venkatesh, and N. Setter. *Journal of Electroceramics*, 11 (1-2):S–66, 2003.

[6] I. B. Vendik, O. G. Vendik, V. M. Pleskachev, and M. A. Nikolski. *IEEE Transactions on Applied Superconductivity*, 13 (2):716–719, 2003.

[7] M. Lippmaa, N. Nakagawa, and M. Kawasaki. *Applied Physics Letters*, 74 (23):3543–3545, 1999.

[8] W. Chang, J. S. Horwitz, A. C. Carter, J. M. Pond, S. W. Kirchoefer, C. M. Gilmore, and D. B. Chrisey. *Applied Physics Letters*, 74 (7):1033–1035, 1999.

[9] R. A. McKee, F. J.Walker, E. D. Specht, G. E. Jellison, Jr., and L. A. Boatner. *Physical Review Letters*, 72 (17):2741–2744, 1994.

[10] P. Casek, S. Boutette-Russo, F. Finocchi, and C. Noguera. *Physical Review B*, 69:085411, 2004.

[11] C. Zhou and D. M. Newns. *Journal of Applied Physics*, 82 (6):3081–3088, 1997.

[12] J. Oh, T. Moon, T.-G. Kim, J. H. Lee, S. Y. Lee, and B. Park. *Current Applied Physics*, 7:168–171, 2007.

[13] L. J. Sinnamon, M. M. Saad, R. M. Bowman, and J. M. Gregg. *Applied Physics Letters*, 81 (4):703–705, 2002.

[14] A. A. Sirenko, I. A. Akimov, J. R. Fox, A. M. Clark, H.-C. Li, W. Si, and X. X. Xi. *Physical Review Letters*, 82 (22):4500–4503, 1999.

[15] P. R. Willmott and J. R. Huber. *Reviews of Modern Physics*, 72 (1):315–328, 2000.

[16] G. J. H. M. Rijnders. *The Initial Growth of Complex Oxides: Study and Manipulation*. PhD thesis, University of Twente, 2001.

[17] M. Y. Chern, A. Gupta, and B. W. Hussey. *Applied Physics Letters*, 60 (24):3045–3047, 1992.

[18] A. Gupta, M. Y. Chern, and B. W. Hussey. *Physica C*, 209:175–178, 1993.

[19] G. J. H. M. Rijnders, G. Koster, D. H. A. Blank, and H. Rogalla. *Applied Physics Letters*, 70 (14):1888–1890, 1997.

[20] M. Ohring. *Material Science of Thin Films*. Academic Press, 2nd edition, 2002.

[21] C. B. Samantaray, H. Sim, and H. Hwang. *Microelectronics Journal*, 36:725–728, 2005.

[22] *CRC Handbook of Chemistry and Physics.* CRC Press, 76th edition, 1996.

[23] J. F. Ready. *Applied Physics Letters*, 3 (1):11–13, 1963.

[24] R. Timm, P. R. Willmott, and J. R. Huber. *Journal of Applied Physics*, 80 (3):1794–1802, 1996.

[25] S. Proyer and E. Stangl. *Applied Physics A*, 60:573–580, 1995.

[26] A. Ichimiya and P. I. Cohen. *Reflection High Energy Electron Diffraction.* Cambridge University Press, 2004.

[27] I. Bozovic, J. N. Eckstein, and N. Bozovic. *In Situ Process Diagnostics and Intellegent Materials Processing*, pages P29–56, 2000.

[28] J. N. Eckstein. Private communication. 2008.

[29] S. Stoyanov. *Surface Science*, 199:226–242, 1988.

[30] S. Stoyanov and M. Michailov. *Surface Science*, 202:109–124, 1988.

[31] T. J. Jackson, S. B. Palmer, H.Blythe, and A. S. Halim. *Journal of Magnetism and Magnetic Materials*, 159:269–281, 1996.

[32] G. Koster, G. J. H. M. Rijnders, D. H. A. Blank, and H. Rogalla. *Applied Physics Letters*, 74 (24):3729–3731, 1999.

[33] M. Lippmaa, N. Nakagawa, M. Kawasaki, S. Oshashi, and H. Koinuma. *Applied Physics Letters*, 76 (17):2439–2441, 2000.

[34] B. W. Wessels. *Journal of Vacuum Science and Technology B.*, 15 (4):1056–1058, 1997.

[35] R. A. McKee, F. J.Walker, E. D. Specht, and K. Alexander. *Materials Research Society Symposium Proceedings*, 341:309–314, 1994.

[36] Y. Y. Tse, S. R. C. McMitchell, T. J. Jackson, Y. I. Liu, and I. P. Jones. *Accepted for publication in Ferroelectrics*, 2008.

[37] N. A. Pertsev, A. K. Tagantsev, and N. Setter. *Physical Review B*, 61 (2):R825–R829, 2000.

[38] G. Catalan, B. Noheda, J. McAneney, L. J. Sinnamon, and J. M. Gregg. *Physical Review B*, 72:020102, 2005.

[39] M. M. Saad, P. Baxter, R. M. Bowman, J. M. Gregg, F. D. Morrison, and J. F. Scott. *Journal of Physics: Condensed Matter*, 16:L451–L456, 2004.

[40] C. Bayer and T. J. Jackson. *Applied Physics Letters*, 89:022908, 2006.

[41] C. B. Parker, J.-P. Maria, and A. I. Kingon. *Applied Physics Letters*, 81 (2):340–342, 2002.

[42] H. M. Chirsten, E. D. Specht, S. S. Silliman, and K. S. Harshavardhan. *Physical Review B*, 68:020101(R), 2003.

[43] J. W. Matthews. *Jounal of Vacuum Science and Technology*, 12 (1):126–133, 1975.

[44] S. P. Alpay, I. B. Misirlioglu, A. Sharma, and Z.-G. Ban. *Journal of Applied Physics*, 95 (12):8118–8123, 2004.

[45] R. Wordenweber. *Superconductivity Science and Technology*, 12:R86–R102, 1999.

[46] P. Paufler, B. Bergk, M. Reibold, A. Belger, N. Patzke, and D. C. Meyer. *Solid State Sciences*, 8:782–792, 2006.

[47] I. Rychetsky, J. Petzelt, and T. Ostapchuk. *Applied Physics Letters*, 81 (22):4224–4226, 2002.

[48] D. H. A. Blank, G. Koster, G. J. H. M. Rijnders, E. van Setten, P. Slycke, and H. Rogalla. *Applied Physics A*, 69 (Suppl.):S17–S22, 1999.

[49] T. J. Jackson and S. B. Palmer. *Journal of Physics D*, 27:1581–1594, 1994.

[50] Y. Y. Tse, Y. Koutsonas, T. J. Jackson, G. Passerieux, and I. P. Jones. *Thin Solid Films*, 515:1788–1795, 2006.

[51] Y. Koutsonas, W. F. Hu, T. J. Jackson, I. P. Jones, M. J. Lancaster, G. Passerieux, R. A. Chakalov, R. I. Chakalova, and C. N. W. Darlington. 2006.

[52] A. Ohtomo and H. Y. Hwang. *Journal of Applied Physics*, 102:083704, 2007.

[53] T. Ohnishi, M. Lippmaa, T. Yamamoto, S. Meguro, and H. Koinuma. *Applied Physics Letters*, 87:241919, 2005.

[54] S. McGuire, D. J. Keeble, R. E. Mason, P. G. Coleman, Y. Koutsonas, and T. J. Jackson. *Journal of Applied Physics*, 100:044109, 2006.

[55] A. M. Glazer. *Student Monographs in Physics: The Structures of Crystals.* IOP Publishing Limited, 1987.

[56] P. Zubko, G. Catalan, A. Buckley, P. R. L. Welche, and J. F. Scott. *Physical Review Letters*, 99:167601, 2007.

[57] G. Koster, K. Verbist, G. Rijnders, H. Rogalla, G. van Tendeloo, and D. H. A. Blank. *Physica C*, 353:167–183, 2001.

[58] J. Kim, Y. S. Kim, and J. Lee. *Surface & Coatings Technology*, 201:5374–5377, 2007.

[59] H. Kinbara, T. Harigai, H. Kakemoto, S. Wada, and T. Tsurumi. *IEEE transactions on Ultrasonics, Ferroelectrics, and Frequency Control*, 54 (12):2541–2547, 2007.